

**Department of Physics and Astronomy**  
**University of Heidelberg**

Master Thesis in Physics  
submitted by

**David Schledewitz**

born in Witzhausen (Germany)

**2023**



# **Characterization of APTS, an analog MAPS test structure fabricated in 65 nm CMOS technology**

This Master Thesis has been carried out by David Schledewitz at the  
GSI Helmholtzzentrum für Schwerionenforschung GmbH, Darmstadt (Germany)  
and Physikalisches Institut Universität Heidelberg, Heidelberg (Germany)  
under the supervision of  
Prof. Dr. Silvia Masciocchi



## Abstract

For the next detector upgrade of the ALICE experiment, it is foreseen to minimize the material budget, reduce the distance to the interaction point, and increase the radiation hardness. In order to achieve this, an extensive R&D program is carried out. From the currently installed ALICE Inner Tracking System (ITS2), the innermost three seven layers of Monolithic Active Pixel sensors (MAPS) will be replaced during the next upgrade. The proposed upgrade (ITS3) is based on curved, wafer-scale, ultra-thin silicon MAPS featuring a truly cylindrical geometry. The proposed technology for this upgrade is the 65 nm CMOS imaging process by Tower Partners Semiconductor Co., Ltd. (TPSCo). One of the current prototypes to evaluate the detection performance and radiation hardness of this technology node is the Analog Pixel Test Structure (APTS). This sensor prototype comprises a 4x4 pixel matrix, and parallel, analog in-pixel processing and readout circuitry in various geometries is used to characterize the 65 nm CMOS technology regarding charge collection properties and radiation hardness. In general, the 65 nm technology is qualified for the use in sensors for particle and nuclear physics experiments.

This thesis provides an overview of the APTS and its characterization in laboratory measurements. Particularly the effect of radiation-induced bulk damage on the sensor performance is investigated for different parameter settings and environmental conditions. Using the analog signal information provided by the sensor, a method for determining the leakage current is developed by investigating the relationship of the signal shape and resetting behavior with respect to different parameter settings and temperatures. This is shown to be a valuable tool for quantifying the performance of the sensor. Using this method, the performance of irradiated sensors is studied, concluding that APTS is operable, having been subject to neutron irradiation up to doses of at least  $10^{15} \text{ 1 MeV n}_{\text{eq}}\text{cm}^{-2}$ . This exceeds the requirements of ITS3 and almost reaches the criteria for the prospective ALICE3 experiment.



## Zusammenfassung

Für das nächste Upgrade des ALICE-Experiments ist die Minimierung des Detektormaterials, die Entfernung zum Kollisionspunkt zu verringern und die Strahlhärte zu erhöhen, vorgesehen. Dafür wurde ein umfangreiches R&D-Programm ins Leben gerufen. Bei diesem geplanten Upgrade (ITS3) werden die innersten drei der sieben Schichten mit den derzeitig installierten *monolithic active pixel sensor* (MAPS) des *ALICE Inner Tracking System* (ITS2) ersetzt. Das Upgrade basiert auf großflächigen, ultra-dünnen MAPS, die zu einer zylindrischen Geometrie gebogen werden. Die vorgesehene Technologie für dieses Upgrade ist der 65 nm CMOS Imaging Process von Tower Partners Semiconductor Co., Ltd. (TPSCo).

Einer der Prototypen zur Erforschung der Leistungsfähigkeit und Strahlenresistenz dieser Technologie ist die *Analog Pixel Test Structure* (APTS). Dieser Prototyp mit einer 4 x 4 Pixelmatrix und paralleler, analoger Schaltung (im Pixel) zur Signalverarbeitung und Auslesung in verschiedenen Geometrien wird zur Charakterisierung der 65 nm CMOS hinsichtlich der Signalerzeugung durch Sammlung der freigesetzten Ladungsträger, Strahlenresistenz und Ladungsverteilung innerhalb des Sensors verwendet.

Diese Arbeit bietet einen Überblick über die APTS und die Labormessungen, welche die charakteristische Leistungsgrößen unter Bestrahlung und mit verschiedenen verschiedenen Parametereinstellungen und unterschiedlichen Temperaturen untersuchen. Unter Verwendung der Signalformen des Sensors wurde eine Methode zur Bestimmung des Leckstroms entwickelt. Dies basiert auf der Untersuchung des Zusammenhangs zwischen Signalform und verschiedenen Parametereinstellungen des Sensors und unterschiedlichen Temperaturen. Es zeigt sich, dass dies eine nützliche Methode zur Quantifizierung der Sensorleistung darstellt. Mit dieser Methode wurde dann die Leistungsfähigkeit bestrahlter Sensoren untersucht. Es wurde festgestellt, dass die APTS nach einer Neutronenbestrahlung bis zu einer Dosis von mindestens  $10^{15} \text{ 1 MeV n}_{\text{eq}}\text{cm}^{-2}$  betrieben werden kann. Dies übersteigt die Anforderungen von ITS3 übersteigt und fast die Kriterien für das in Zukunft geplante ALICE3-Experiment erfüllt.



# Contents

<b>1</b>	<b>ALICE at the LHC</b>	<b>1</b>
1.1	Quark-gluon-plasma . . . . .	1
1.2	ALICE . . . . .	2
1.3	ITS2 . . . . .	4
1.3.1	ITS2 Layout . . . . .	4
1.3.2	Alice Pixel Detector . . . . .	5
1.4	The next upgrade of the ITS . . . . .	6
<b>2</b>	<b>Monolithic Active Pixel Sensors</b>	<b>10</b>
2.1	Silicon properties . . . . .	10
2.2	The p-n junction . . . . .	12
2.3	Working principles of transistors . . . . .	14
2.3.1	Subthreshold regime . . . . .	17
2.4	Physics of particle detection in silicon sensors . . . . .	19
2.4.1	Radiation damage effects in silicon . . . . .	20
2.5	Working principles of MAPS . . . . .	23
<b>3</b>	<b>ITS3 pixel test structures</b>	<b>25</b>
3.1	Multi-layer per reticle run . . . . .	25
3.2	APTS characteristics . . . . .	27
3.2.1	Architecture . . . . .	28
3.2.2	Signal Processing . . . . .	30
<b>4</b>	<b>Data acquisition and signal calibration in laboratory measurements</b>	<b>33</b>
4.1	Experimental setup . . . . .	33
4.2	Signal injection via pulsing . . . . .	34
4.3	Systematic parameter measurements . . . . .	37
4.4	Pulse shape dependence on sensor parameters . . . . .	39
4.5	Dependence of effective reset current on applied bias parameters . . . . .	41
4.6	Laboratory measurements of irradiated sensors using pulsing . . . . .	42
4.7	<sup>55</sup> Fe source measurements . . . . .	43

<b>5</b>	<b>Leakage Current Analysis</b>	<b>45</b>
5.1	Preliminary considerations to the reset current . . . . .	45
5.2	The effective reset current . . . . .	47
5.3	Reset current determination . . . . .	49
5.4	Leakage current determination . . . . .	55
<b>6</b>	<b>Performance of irradiated and non-irradiated APTS sensors</b>	<b>60</b>
6.1	Signal analysis as a function of the operating temperature and radiation dose . . . . .	60
6.2	Noise investigation . . . . .	64
6.3	Leakage current determination . . . . .	65
6.3.1	Pixel-to-pixel variation . . . . .	66
6.3.2	Leakage current dependence on reverse bias . . . . .	70
6.3.3	Temperature effect on the leakage current for different irra- diation levels . . . . .	71
<b>7</b>	<b>Conclusion</b>	<b>74</b>
	<b>Appendices</b>	<b>77</b>
<b>A</b>	<b>Derivation of the fit function used for the determination of the effective reset current</b>	<b>78</b>

# Chapter 1

## ALICE at the LHC

High-energy particle physics focuses on investigating the basic elements of matter and their interactions. The underlying theoretical structure for these studies is provided by the Standard Model [1]. At the *Conseil Européen pour la Recherche Nucléaire* (CERN) in Geneva, Switzerland, experiments are conducted to confirm the predictions and test the limitations of this model. For this purpose, protons and heavier nuclei such as lead are accelerated in particle accelerators and brought to collision in particle detectors. The largest and most powerful accelerator in the world is the *Large Hadron Collider* (LHC) at CERN with a circumference of 27km [2]. At the LHC particles are accelerated to extraordinary energies and brought to collision with other particles. The collisions happen within sophisticated particle detector systems, specialized in tracking and identifying the outgoing particles produced inside these collisions.

### 1.1 Quark-gluon-plasma

The Quark-Gluon Plasma (QGP), is formed at extremely high temperatures and energy densities and is believed to have existed microseconds after the Big Bang. It can also be created in high-energy particle collisions in modern accelerators like the LHC. In this state of matter, quarks and gluons are no longer confined within hadrons but move freely within the medium, a characteristic known as asymptotic freedom. This condition of freedom is illustrated by the behavior of the strong coupling constant,  $\alpha_s$ , as depicted in figure 1.1.

At energy scales  $Q$  in the order of 1 GeV, the strong coupling constant  $\alpha_s$  is large, close to 1. This is a regime where quarks and gluons are strongly bound into hadrons, a phenomenon known as color confinement and is one of the most important concepts of Quantum Chromodynamics (QCD) [1]. Following this principle, color-charged objects like quarks and gluons are always confined within

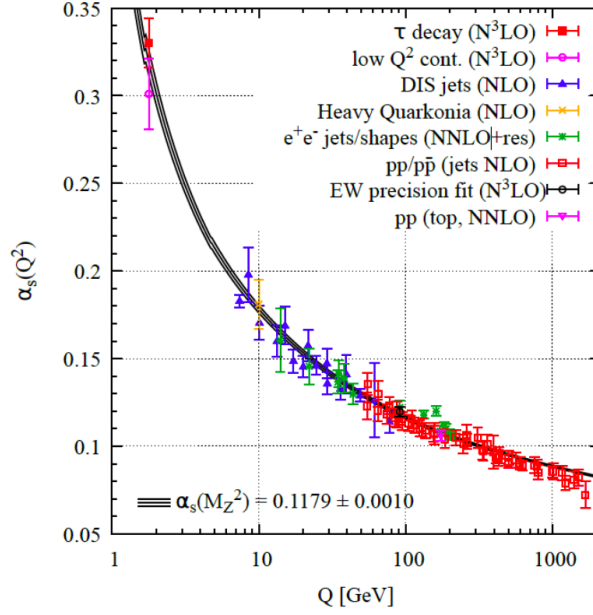


Figure 1.1: Measurements of the strong coupling constant  $\alpha_s$  on the energy scale,  $Q$ . Asymptotic freedom is shown by the decrease of  $\alpha_s$  with increasing energy [3].

color-neutral objects. Consequently, no isolated quarks or gluons can be observed in nature, as only color-neutral particles can behave like free particles.

As the energy scale increases beyond 100 GeV, the value of  $\alpha_s$  becomes significantly smaller, approximately 0.1. This decrease in  $\alpha_s$  indicates the weakening of the strong force, allowing quarks and gluons to act almost as free particles. This regime is referred to as asymptotic freedom, which describes how quarks and gluons behave in the QGP. However, QGP is not directly observable in experiments. Instead, properties such as particle yields, ratios, and the collective flow are observed and investigated.

## 1.2 ALICE

One of the main experiments at the LHC is *A Large Ion Collider Experiment* (ALICE), dedicated to probing the physics of strongly interacting nuclear matter created in heavy-ion collisions, such as lead-lead. As described in the previous section, in this environment, QGP is created. To carry out investigations on this matter, ALICE comprises several specialized detectors, each designed to measure different properties of the particles produced in the collisions. The Inner Tracking System (ITS), Time Projection Chamber (TPC), Time-of-Flight (TOF) detector, and Electromagnetic Calorimeter (EMCal) are among these detectors [4]. The signals from these devices are rigorously studied and reconstructed to retrieve information

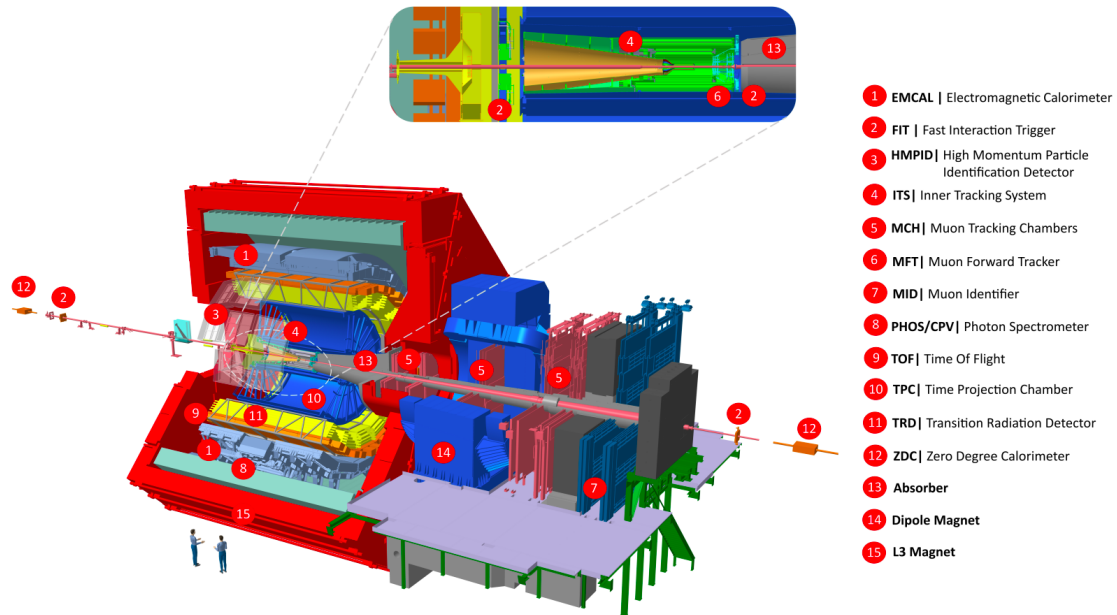


Figure 1.2: Schematic view on the ALICE detector. [5].

about the momenta of the particles, energy, and identities. An overview of all detector subsystems is illustrated in figure 1.2.

The Inner Tracking System (ITS), one of the main detectors, precisely tracks charged particles as they move through the innermost part of the detector. A high spatial resolution is provided by the high pixel granularity of the newly installed upgrade ITS2, consisting of *Monolithic Active Pixel Sensor* (MAPS)[5]. ITS2 consists of seven layers of silicon sensors, which also make it possible to reconstruct particle paths. With this knowledge, the momentum and charge of particles created during collisions can be identified.

Another crucial component of ALICE is the Time Projection Chamber (TPC). The TPC is a large cylinder filled with a noble gas mixture, and it measures the position and momentum of charged particles produced in the collisions. The TPC offers valuable information about the particles, such as their energy loss and particle identity, by monitoring their trajectories as they interact with the gas. Other detectors, such as the transition radiation detector (TRD) and the time of flight (TOF) detector, provide further information for particle identification, assisting the TPC. Further details on the detectors mentioned and other components of the ALICE experiment not addressed here are given in [5]. The combination of all these detectors allows for the precise measurement of particle properties, such as momentum, charge, and energy, enabling the reconstruction of collision events and extraction of valuable information about the produced particles and the underlying physics processes.

## 1.3 ITS2

The Inner Tracking System (ITS2) is a state-of-the-art component of the ALICE detector with the task of reconstructing tracks as well as primary and secondary vertices of particles charged particles traversing it. It was installed in 2021 during the Long Shutdown 2 (LS2) and is currently operational during the LHC Run 3. An impressive active surface of  $10 \text{ m}^2$  and nearly 12.5 Gpixels distributed on 24,000 ALPIDE sensors significantly improves the experiment's capabilities. The primary goal of ITS2 upgrade within ALICE is to improve the reconstruction of primary and secondary vertices created from heavy-flavor hadrons and improve the tracking performance of low- $p_T$  particles. The enhancements realized through the upgrade to ITS2 are remarkable and include up to a five-fold increase in impact parameter resolution, thanks to [5, 6, 7]:

- A reduction of the beampipe diameter from 29 mm to 19.2 mm.
- A repositioned innermost layer moved closer to the interaction point (from 39 mm to 23 mm).
- A reduction in pixel size, from  $50 \times 425 \text{ }\mu\text{m}$  down to  $29.24 \times 26.88 \text{ }\mu\text{m}$ .
- A decreased material budget, with 0.35 %  $X/X_0$  for the inner layers compared to the previous 1.14 %  $X/X_0$ .

Enhanced granularity and the addition of an extra tracking layer, have strengthened the tracking efficiency, particularly in the low transverse momentum range. Consequently, a spatial resolution of  $5 \text{ }\mu\text{m}$  is achieved. In addition, ITS2 supports a higher readout rate, achieving 100 kHz in lead collisions and 200 kHz in proton collisions, a significant jump from the 1 kHz offered by its predecessor. Especially with higher rates, another requirement is to maintain a low Fake Hit Rate (FHR) of less than  $10^{-6}$  hits/(event and pixel). This target is exceeded, with a measured rate of  $10^{-8}$  hits/(event and pixel) during Run 3[6].

Another important aspect is the required radiation hardness of 2.7 kGy Total Ionising Dose (TID) and  $1.7 \cdot 10^{12} \text{ 1 MeV n}_{\text{eq}}\text{cm}^{-2}$  Non-Ionising Energy Loss (NIEL), as the radiation load is increased by 60 to 70 % from Run 2 to Run 3 [6].

### 1.3.1 ITS2 Layout

Figure 1.3 illustrates the detector layout of the upgraded ITS2. The seven layers of the ITS2 are divided into two sections: the Inner Barrel (IB) and the Outer Barrel (OB). The IB consists of the innermost three layers, the OB of the outer four. In each detector layer triangular support structures, referred to as staves,

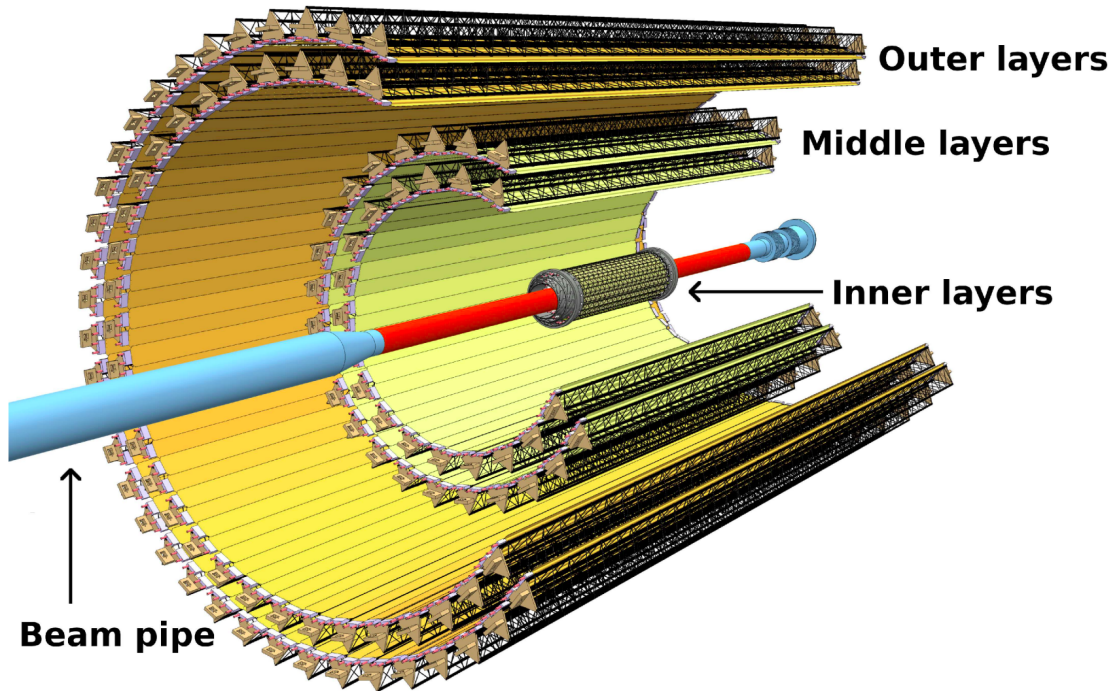


Figure 1.3: Schematic layout of the ITS2 [8].

are carrying the azimuthally segmented detector units. Each stave, regardless of its location, is composed of several key components. The Space Frame is a lightweight mechanical support structure made from carbon. The Cold Plate is another carbon support structure that houses water-cooling pipes for efficient heat conduction and dissipation from the chips. The Hybrid Integrated Circuit (HIC) is an essential component with a Flexible Printed Circuit (FPC) responsible for sensor readout, control, and power supply. The pixel chips as well as other passive components are bound onto this circuit. In the case of the OB half-staves, the HIC unit is glued onto a carbon plate known as a Module Plate. This modular and segmented design of the staves provides structural integrity and functional utility, ensuring efficient operation of the ITS2.

### 1.3.2 Alice Pixel Detector

The backbone of the ITS2 is the *ALice Pixel DEtector* (ALPIDE) chip, a Monolithic Active Pixel Sensor (MAPS, see section 2.5) that employs a 180 nm CMOS<sup>1</sup> Imaging Process from Tower Partners Semiconductor Co., Ltd. (TPSCO) [9, 10, 11]. This sensor was fabricated on high-resistivity silicon wafers (50  $\mu\text{m}$ ) featuring an epitaxial layer with a thickness of 25  $\mu\text{m}$ . An image of a single ALPIDE sensor is shown in Figure 1.4a.

<sup>1</sup>Complementary Metal Oxide Semiconductor

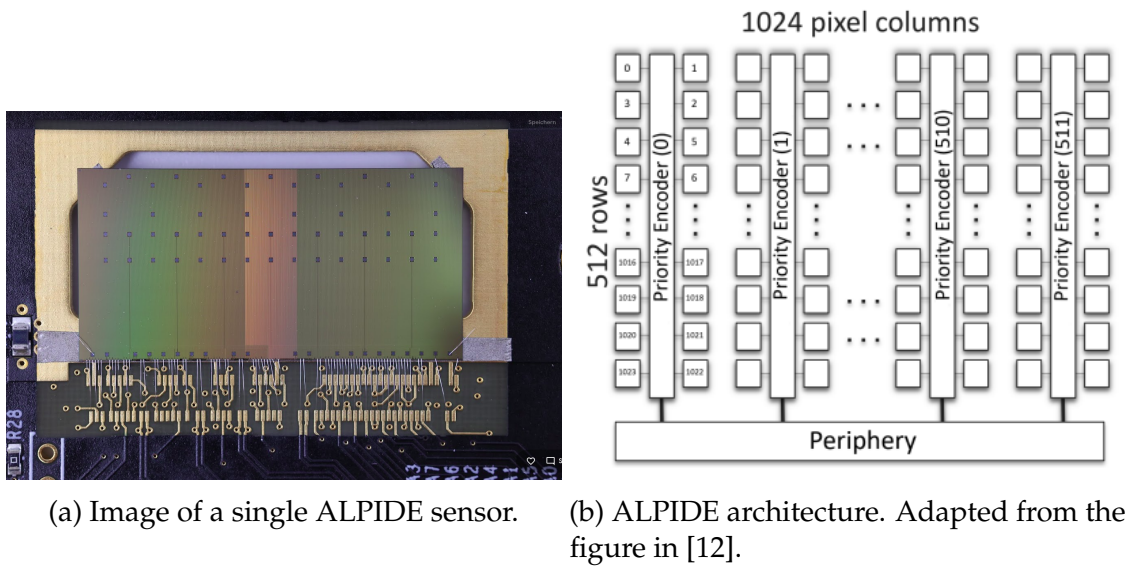


Figure 1.4: ALPIDE sensor and architecture.

Measuring  $30 \times 15 \text{ mm}^2$ , the ALPIDE chip integrates a pixel matrix of 1024 columns by 512 rows. Each pixel, with dimensions of  $29.24 \times 26.88 \text{ }\mu\text{m}^2$ , is equipped with in-pixel amplification, shaping, discrimination, and multi-event buffering capabilities.

The metal layers placed on top of the implants of the epitaxial layer provide in-pixel circuitry and are responsible for signal transfer to the chip logic. Figure 1.4b shows the chip matrix readout structure. The row and column numbers of a pixel determine its address, which can be read out in case of an incoming particle.

## 1.4 The next upgrade of the ITS

The ALPIDE sensor, used in the Inner Tracking System 2 (ITS2) of the ALICE experiment, marks a significant milestone in the evolution of MAPS technology in high-energy physics experiments. The extensive research & development program has resulted in an excellent signal-to-noise ratio, spatial resolution, material budget, and readout speed performance.

However, the fast progress in the field of CMOS imaging sensor technologies offer interesting opportunities for further optimization. Recent developments include the technique known as *stitching*, allowing the fabrication of wafer-sized large area MAPS, up to  $21 \text{ cm} \times 21 \text{ cm}$ , using 300 mm diameter wafers [9]. Another key advancement is the reduction of sensor thickness to around 20 to 40  $\mu\text{m}$ , opening up the potential of flexible silicon for large-area curved sensors. This innovation could lead to the creation of truly cylindrical silicon-only sensor layers, significantly reducing the material thickness.

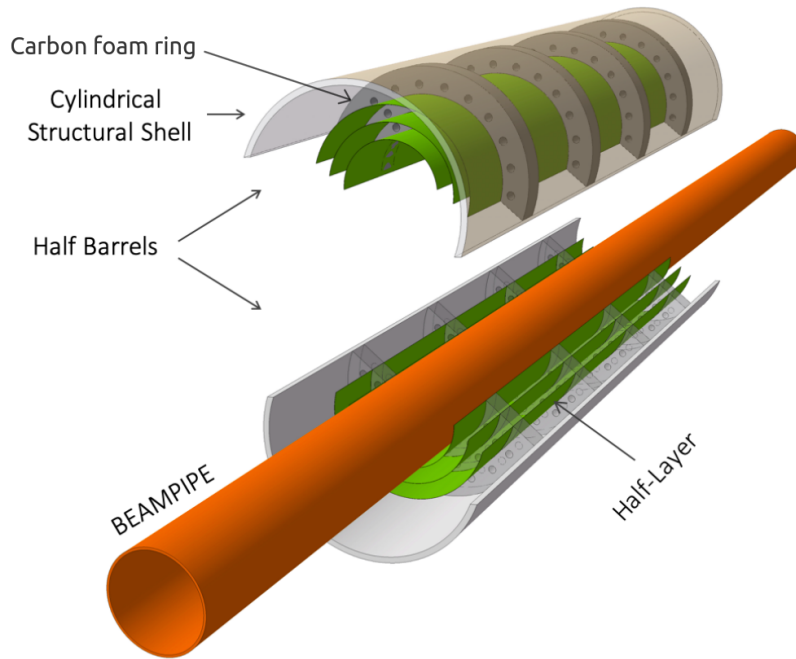


Figure 1.5: Layout of the future ITS3 Inner Barrel [7].

With these possibilities, another upgrade of the ALICE ITS is proposed for the next LHC Run 4 upcoming in 2029, namely the ITS3. The target of this upgrade is to enhance the tracking precision and efficiency, especially at low- $p_T$ . The ITS3 will comprise three cylindrical layers constructed from curved, wafer-scale stitched sensors, replacing the Inner Barrel of the ITS2, as depicted in figure 1.5. These sensors are proposed to feature a minimal material budget of  $0.05\% X/X_0$  per layer. The innermost layer will be placed at a radial distance of 18 mm from the interaction point, which, in combination with a new beam-pipe of reduced radius (16 mm inner radius) and thickness ( $500\ \mu\text{m}$ ), will bring the detection layer closer to the interaction point (reducing the distance from 23 mm to 18 mm) and reduce the material budget close to the interaction point by a factor of six [7].

**Material budget reduction** The significant reduction of the material budget is one of the main improvement requirements of the ITS3. Figure 1.6 shows the material budget distribution of the ITS2. It is noticeable that only 15% of the total material budget is silicon ( $50\ \mu\text{m}$  thick). The remaining 85% are expended on the electrical substrate, cooling circuit, and carbon spaceframe of the stave (see section 1.3). To make significant improvements on the material budget and match the requirements of the ITS3 upgrade, the electrical, mechanical, and cooling materials need to be reduced.

A detector design that eliminates the need for an electrical substrate and an active cooling circuit must be considered. Using the mentioned *stitching* technology,

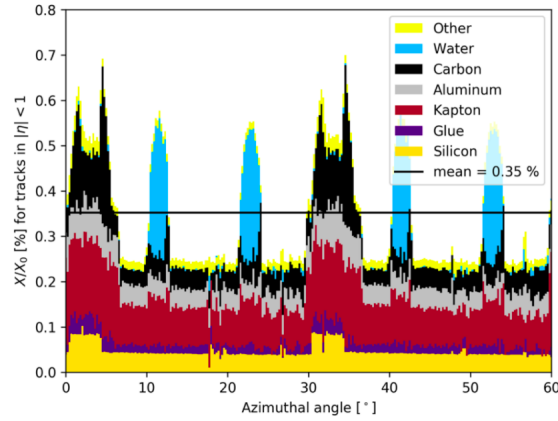


Figure 1.6: Azimuthal distribution of the material budget of ITS2 Layer 0. The angular interval depicted corresponds to two staves, set at  $\Phi = 0$  on the horizontal plane, where a staff from the upper half-barrel and another from the lower half-barrel overlap [7].

large-scale sensors can be fabricated, limited only by the wafer size [9]. This technology could enable the construction of a pixel sensor of the dimension of an entire staff, allowing power and electrical signal distribution to be done entirely inside the silicon chip.

For cooling, low-speed airflow has been considered to remove heat by convection in combination with peripheral liquid cooling. This is only a reasonable solution for sensors with a power density below  $20 \text{ mW/cm}^2$ . Looking at the ALPIDE chip, it dissipates  $40 \text{ mW/cm}^2$ , but  $5/6$  of it is dissipated via the digital interface circuitry and the high-speed output data links. These are located in a small area of  $30 \times 1.5 \text{ mm}^2$  on each ALPIDE sensor. Hence, only  $1/6$  of the total power is dissipated in the pixel matrix, resulting in a power density of about  $7 \text{ mW/cm}^2$ , a range suitable for air cooling. Therefore, relocating the pixel sensor's digital periphery to the edge of a wafer-sized detector is a considered solution to the cooling and material budget problem [7].

**Stitching** The central concept for realizing the wafer-scale sensors required for the ITS3 upgrade is to utilize stitching technology. Usually, the limit on sensor dimensions is the reticle size in standard CMOS circuit manufacturing, which can be circumvented using this technology, due to the possible high-precision placement of the reticles on the wafer. Using this technology, a wafer-sized sensor, as shown in figure 1.7, can be realized. By integrating multiple of these sensor units on one 300 mm wafer, a rectangular matrix of  $280 \times 100 \text{ mm}$  can be achieved, enough to match the dimensions of the outermost and largest layer of the proposed ITS3 ( $280 \times 94 \text{ mm}^2$ ) [7].

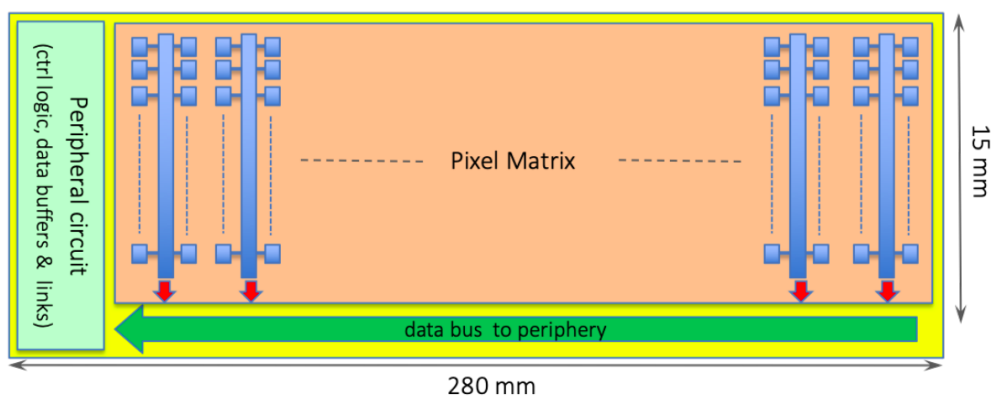


Figure 1.7: Illustration of a stitched sensor in one dimension (sensor dimensions not to scale) [7].

This, however, indicates the need for 300 mm wafers, as for the 200 mm wafers used for the ITS2, a further segmentation into separate sensors would be needed. Hence, the use of a new sensor technology, the 65 nm process is proposed for the ITS3 design, as this process is available in 300 mm wafers [9]. Apart from the wafer size, this technology has further advantages. For example, the smaller feature size of 65 nm, compared to ALPIDE's 180 nm, enables a reduction of the pixel pitch by a factor greater than two. This results in a significantly faster charge collection time and enhances position resolution, creating a more precise and efficient sensor.

**Radiation load** Another crucial aspect is the radiation load the ITS3 has to withstand, which is increasing due to the closer distance of the sensor layers to the interaction point and increasing particle flux through the innermost layer. With an expected increase of 70%, compared to the ITS2 dose, it is predicted to stay well below  $1 \times 10^{13}$   $1 \text{ MeV } n_{\text{eq}} \text{ cm}^{-2}$  NIEL and 10 kGy TID. These values represent the performance limits for the ALPIDE sensor, suggesting that the increased radiation exposure should not restrict the ITS3 sensor performance [7].

However, looking forward to ALICE3, the possible successor of ALICE and the ITS3, higher requirements for radiation tolerance are foreseen. The highest radiation load per year of operation is estimated to reach approximately  $1.5 \times 10^{15}$   $1 \text{ MeV } n_{\text{eq}} \text{ cm}^{-2}$  on the first tracking layer, positioned at a radial distance of just 5 mm from the point of interaction in the experiment proposal [13]. This significantly increased radiation level emphasizes the need for advanced sensor designs with even greater radiation hardness for the future of high-energy physics experiments, which the technology used for the ITS3 is a candidate for. Hence, investigation of the radiation hardness, also beyond the ITS3 requirements, is recommended.

# Chapter 2

## Monolithic Active Pixel Sensors

In high-energy particle physics, a variety of sophisticated detectors are utilized to capture and analyze data from complex particle interactions. These collisions form the basis of the observations and measurements that help us unravel the mysteries of fundamental physical processes.

An important quantity to measure from the particles created in these collisions is their exact position. Hence, detectors capable of performing precision position measurements, known as tracking or vertexing detectors, are highly valued. Ideally, these are placed as close to the interaction point as possible, enabling the detection of even short-lived and low- $p_T$  particles. Because of this proximity to the collision point, these detectors must meet a set of strict requirements, including high granularity, minimal material thickness, fast readout speed, and low power consumption. As tracking detectors operate close to the collision point, high robustness against potentially damaging high particle fluxes is required, as *radiation damage* can reduce the performance of these detectors over time.

Silicon pixel detectors are a type of detector that can meet all these requirements, making them a popular choice in many high-energy physics experiments, particularly those at the LHC and the ALICE experiment. As described in section 1.3, the ALICE experiment currently employs this type of tracking detector.

### 2.1 Silicon properties

Silicon, a semiconductor, forms the basis for the majority of electronic devices, including the pixel detectors used in high-energy physics experiments. To understand the working principles of such devices, it is necessary to begin with the properties of intrinsic (undoped) silicon.

A useful concept for understanding the behavior of a silicon crystal is the band model. In this model, electrons occupy discrete energy levels, known as energy bands. The energy band of highest energy, the *conduction band*, electrons are free

to move through the crystal, contributing to the material's conductivity. On the other hand, the *valence band*, located at a lower energy level, contains electrons that remain bound to their lattice atoms.

At 0 K, a semiconductor like silicon behaves as an insulator since its valence band is fully occupied and no electrons are in the conduction band to conduct electricity. The energy gap at absolute zero between these bands in intrinsic silicon, known as the bandgap  $E_g$ , is about 1.12 eV at room temperature.

At room temperature, some electrons gain enough thermal energy to cross the bandgap and reach the conduction band, leaving holes in the valence band. These thermally generated electron-hole (e-h) pairs are known as intrinsic charge carriers. The concentration of these intrinsic charge carriers, defined as  $n_i$ , is the number of such carriers in a unit volume. In intrinsic silicon, the electron density  $n$  equals the hole density  $p$ , resulting in  $n_i = n = p$ . For silicon at room temperature (300K), this concentration  $n_i$  is approximately  $1.5 \times 10^{10} \text{ cm}^{-3}$ , in other words, one out of  $10^{12} \text{ cm}^{-3}$  atoms have an excited intrinsic charge carrier [14]. This carrier concentration can be described as:

$$n_i \propto T^{3/2} \exp\left(\frac{-E_g}{2k_B T}\right) \quad (2.1)$$

where  $T$  is the absolute temperature,  $k_B$  is Boltzmann's constant, and  $E_g$  is the energy bandgap.

Next, the electrical properties of silicon can be discussed. The resistivity of intrinsic silicon, denoted as  $\rho_i$ , can be expressed using the following relation:

$$\begin{aligned} \rho &= \frac{1}{\sigma} = \frac{1}{e(n\mu_e + p\mu_h)} \\ \rho_i &= \frac{1}{\sigma_i} = \frac{1}{e \cdot n_i(\mu_n + \mu_p)} \end{aligned} \quad (2.2)$$

where  $e$  is the charge of an electron,  $\sigma_i$  the conductivity, and  $\mu_n$  and  $\mu_p$  represent the electron and hole mobility, respectively.

Intrinsic silicon is not used in most semiconductor applications. By introducing impurities in a process called doping, the properties of silicon can be significantly changed. These impurities, having a different number of valence electrons, change the balance of free electrons and holes, forming an *extrinsic* or *doped* semiconductor, a key advancement of silicon towards the development of silicon detectors.

These impurities are classified as *donors*, providing extra valence electrons, and *acceptors*, offering additional holes. In n-type semiconductors, electrons dominate as the *majority* charge carriers, due to the contribution of donor impurities. Contrarily, in p-type semiconductors, the majority of charge carriers are holes due to

the acceptor impurities. The carrier concentration in both types can be expressed as:

$$np = n_i^2 \propto T^3 \exp\left(\frac{-E_g}{kT}\right). \quad (2.3)$$

To maintain neutrality, positive and negative charges within the crystal have to be equal:

$$N_D + p = N_A + n \quad (2.4)$$

Here,  $N_D$  and  $N_A$  denote donor and acceptor impurity concentrations. For n-type silicon, there are only donors ( $N_A = 0$ ), and with  $n \gg p$ ,  $n \simeq N_D$ . Consequently, the resistivity of an n-type semiconductor follows:

$$\rho = \frac{1}{eN_D\mu_e}. \quad (2.5)$$

Calculations for a p-type semiconductor analog to those for the n-type [14].

## 2.2 The p-n junction

A special configuration arises when a p-type semiconductor is combined with an n-type, forming a *pn-junction*. This setup plays a crucial role in many semiconductor devices, including diodes and transistors, which are key components in modern electronics.

When a pn-junction is created, the carriers begin to diffuse across the junction, electrons from the n-region to the p-region and holes from the p-region to the n-region. This diffusion process creates a *depletion region* at the junction, which is essentially a region without any mobile charge carriers. This happens because the diffusing electrons and holes recombine with each other in the depletion region. The net result is the formation of a space charge (or depletion) region, with negatively charged acceptor ions on the p-side and positively charged donor ions on the n-side of the junction. This fixed charge distribution results in an electric field  $E$  across the junction. Due to this electric field, electrons or holes created in the depletion region are accelerated to n-doped and p-doped side, respectively. This characteristic process of the pn-junction is visualized in figure 2.1, providing idealized distributions of the charge carrier concentration, the charge density  $Q$ , the electric field  $E$ , and the electric potential  $V$ . The electric field creates a potential barrier,  $\Delta V$ , often referred to as the *built-in potential* or *junction potential*, which can be given by the formula [14, 15]:

$$\Delta V = \frac{k_B T}{e} \ln \left( \frac{N_A N_D}{n_i^2} \right) \quad (2.6)$$

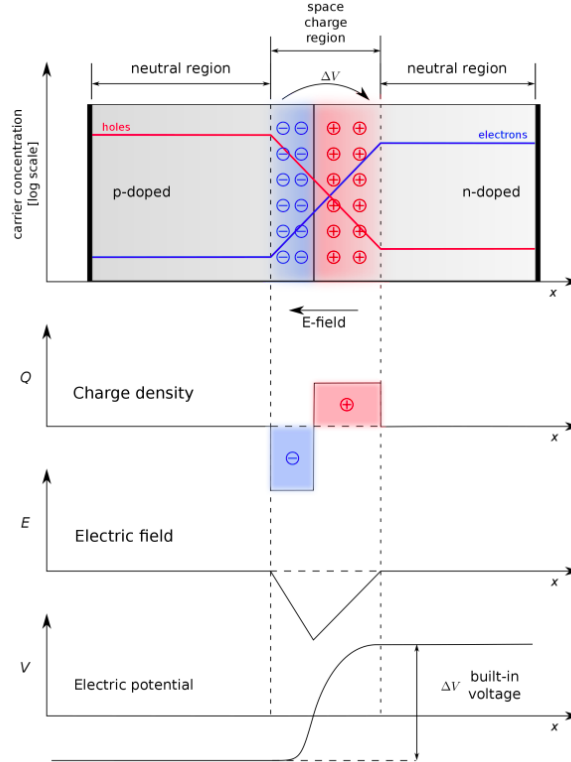


Figure 2.1: Schematic of a pn-junction in thermal equilibrium. Distributions of the charge carrier concentration, the charge density  $Q$ , the electric field  $E$ , and the electric potential  $V$  are plotted [16].

**Depletion depth** Using the Poisson equation the depletion region's width can be calculated, as it connects the charge density distribution with the potential difference. The width or depletion depth  $d$  is calculated as

$$d = \sqrt{\frac{2\epsilon}{e} \frac{N_D + N_A}{N_D N_A} \Delta V} \quad (2.7)$$

where  $\Delta V$  represents the built-in voltage,  $N_D$  and  $N_A$  are the doping concentrations in the n- and p-doped sides, respectively, and  $\epsilon$  is the dielectric constant.

For effective particle detection in the application in detector systems, a larger depletion region is preferred, as it allows for an increased interaction volume. Therefore, high-resistivity silicon is used in most detector designs, due to its ability to produce a larger depletion depth.

In addition to optimizing the semiconductor material, increasing the potential difference in the pn-junction also enlarges the depletion region. A *reverse-bias voltage*  $V$  can be applied to the junction for this purpose, pulling the majority of charge carriers from the junction towards the material's edges. This process enlarges the depletion region according to the equation:

$$d = \sqrt{\frac{2\epsilon}{e} \frac{N_D + N_A}{N_D N_A} (\Delta V + V)} \quad (2.8)$$

This increase in the depletion region amplifies the charge collection efficiency due to the extended electric field. In this way, both material and electrical changes lead to optimized semiconductor detectors for efficient operation.

**Junction capacitance** The capacitance of the junction can be understood in terms of the behavior of a parallel plate capacitor, consisting of two conductive plates separated by a dielectric medium. The capacitance  $C$  is given by the formula:

$$C = \frac{\epsilon A}{d} \quad (2.9)$$

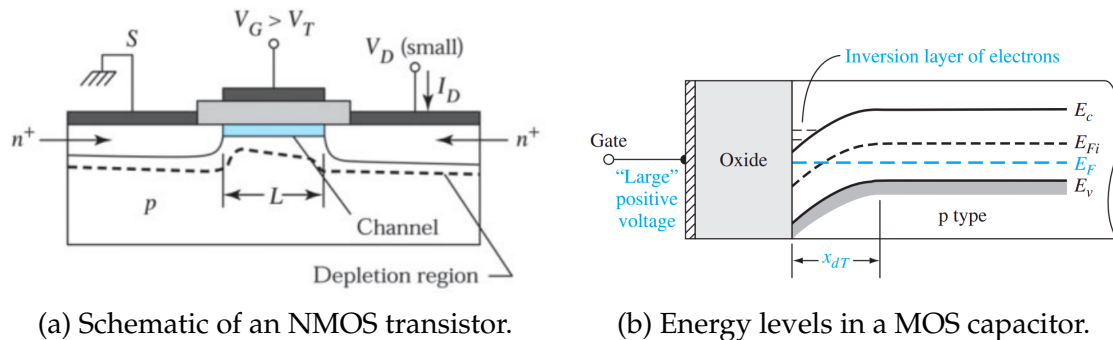
where  $\epsilon_s$  is the permittivity of the dielectric medium,  $A$  is the area of one of the plates, and  $d$  is the separation between the plates, which is equal to the depletion depth.

It is worth noting that the depth of the depletion region  $d$  changes with the applied reverse bias voltage. Consequently, the capacitance of the junction is not a fixed value but varies with the applied voltage. As the reverse bias voltage increases, the width of the depletion region also increases, thereby decreasing the junction capacitance.

## 2.3 Working principles of transistors

Transistors, which operate based on p-n junctions, are among the most commonly produced electronic devices. For the operation of MAPS detectors, commonly a type of transistor called the Metal-Oxide-Semiconductor Field-Effect Transistor (MOSFET) is used. In general, this transistor type is widely used in the design and fabrication of integrated circuits due to its high speed and low power operation. MOSFETs are created in two types: n-channel (NMOS) and p-channel (PMOS), depending on their configuration. NMOS transistors are built from n-p-n junctions, while PMOS transistors are formed from p-n-p junctions. Despite the distinct configurations, both types share a similar operating principle.

An NMOS transistor features four distinct connections: source, drain, gate, and substrate (or bulk). The substrate is of p-type in an NMOS transistor, while the source and drain connect to separate n-type implants, creating two p-n junctions. Between these two connections is an electrically insulating metal oxide layer, typically made of silicon dioxide, on top of the p-type substrate, as depicted in figure 2.2. Analogous conclusions can be made for PMOS transistors by considering their reverse doping profile.



(a) Schematic of an NMOS transistor.

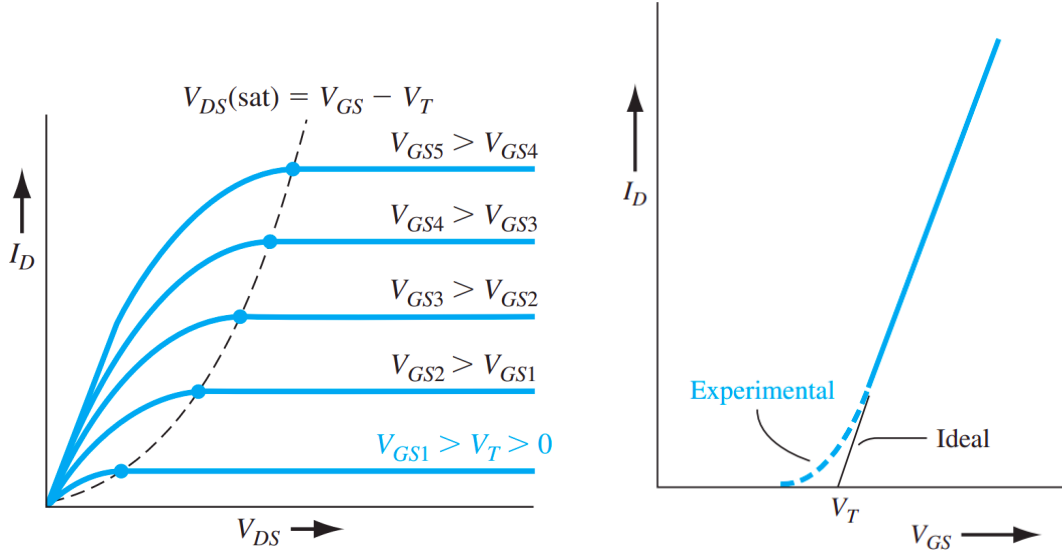
(b) Energy levels in a MOS capacitor.

Figure 2.2: (a) depicts a simple n-type MOSFET, including source, drain, and gate connections. Source and drain are separated via a MOS capacitor consisting of an insulation layer and a metal gate electrode [17]. The energy level behavior in a MOS capacitor for a large gate voltage  $V_G$  applied is shown in (b)[15].

In addition to the source, drain, and gate connections, an NMOS transistor consists of a MOS capacitor between the drain and source.

When a voltage is applied to the gate terminal of a MOSFET, an electric field is generated across the gate oxide. When the gate voltage is less than the threshold voltage, there are insufficient electric field strength and energy to invert the majority carrier type at the semiconductor-oxide interface, i.e., to generate a sufficient density of mobile carriers to create a conductive channel. However, when the applied gate voltage exceeds the material- and temperature-dependent threshold voltage  $V_T$ , the electric field strength is sufficient to invert the carrier type at the semiconductor-oxide interface, forming a channel of carriers (electrons for NMOS, holes for PMOS) that enables current flow from the source to the drain. The dimensions of this layer can be controlled through biasing of the gate leading to different operating regimes of the transistor: the subthreshold, linear and saturation regime, which are depicted in figure 2.3.

**Subthreshold regime** In the *subthreshold* regime, also known as *weak-inversion* regime, or cut-off region, the gate-source voltage ( $V_{GS}$ ) is below the threshold voltage ( $V_T$ ). The transistor is technically not conducting in this state. However, a small amount of minority carriers (electrons in a p-type substrate for an NMOS or holes in an n-type substrate for a PMOS) are thermally generated and can move



(a) MOSFET behavior for  $I_D$  against  $V_{DS}$  with different values of  $V_{GS}$ . (b) Comparison of ideal and experimental behavior of  $I_D$  against  $V_{GS}$ .

Figure 2.3: MOSFET behavior in different regimes of  $V_{DS}$  and  $V_{GS}$  [15].

across the substrate. These minority charge carriers contribute to the drain current ( $I_D$ ) in the subthreshold regime, as explained in detail in section 2.3.1.

**Linear regime** When the gate potential surpasses a threshold value ( $V_{GS} > V_T$ ), electrons accumulate at the semiconductor-insulator interface, forming an inversion layer. In the case of the NMOS transistor, this results in a conductive n-type channel between the source and drain, allowing drain current ( $I_D$ ) to flow. The width of the channel and, consequently, the conductivity between source and drain increase with the gate potential. Hence, the current of the transistor can be regulated via the gate potential. When  $V_{DS} < V_{GS} - V_T$ , the transistor is in the linear regime, meaning  $I_D$  is proportional to  $V_{DS}$ , assuming constant  $V_{GS}$ , as visible in figure 2.3a, and expressed in:

$$I_D = \mu C_{ox} \frac{W}{L} \left( (V_{GS} - V_T) V_{DS} - \frac{V_{DS}^2}{2} \right) \quad (2.10)$$

where  $\mu$  is the carrier mobility,  $C_{ox}$  is the oxide capacitance per unit area,  $W$  is the channel width,  $L$  is the channel length.

**Saturation Regime** As  $V_{DS}$  continues to increase, it eventually becomes equal to the saturation voltage ( $V_{DS,sat} = V_{GS} - V_T$ ). At this point, the MOSFET enters the saturation region, where the conductive channel "pinches-off" near the drain, and the drain current saturates. This saturation is due to the formation of a high-

resistance region near the drain, effectively limiting the current flow through the device. In this region, the drain current is given by the equation:

$$I_D = \frac{1}{2} \mu C_{ox} \frac{W}{L} (V_{GS} - V_T)^2 \quad (2.11)$$

This equation indicates that the current is independent of  $V_{DS}$  in the saturation region (assuming  $V_{DS} > V_{GS} - V_T$ ) and is only controlled by the gate-source voltage. However, effects like the channel length modulation, leading to a very small increase with increasing  $V_{DS}$ , are neglected in this representation [15].

### 2.3.1 Subthreshold regime

While the operation of the MOSFET in the subthreshold region shows several benefits, such as low power consumption, the calculation of the subthreshold current is complex compared to the above-threshold regimes. In this region, the drain current,  $I_D$ , does not show a simple linear or quadratic dependence on the gate voltage but rather an exponential dependence on  $V_{GS}$ .

Apart from this exponential behavior, several second-order effects such as the influence of the  $V_{DS}$ , channel length modulation, source/drain depletion region charge sharing, body-effect, and others have to be considered in this low current regime [18]. These second-order effects are crucial for the precise modeling of circuits operating in the subthreshold region, particularly as device dimensions continue to decrease.

An advanced model considering all these effects is the Berkeley Short-Channel IGFET Model (BSIM) [18, 19, 20]. The BSIM model includes a multitude of effects and has been extensively adopted by the semiconductor industry for the design and analysis of ultra-large-scale integration (ULSI) circuits. The BSIM model provides an accurate model for  $I_D$  and is crucial for modern integrated circuit design. However, it is worth noting that even with the BSIM model, the accurate prediction of the subthreshold behavior is still challenging due to the high sensitivity of the current to process variations, temperature, and other aspects.

According to the BSIM4 model, the subthreshold current is given by

$$I_D = \frac{I_{exp} \cdot I_{lim}}{I_{exp} + I_{lim}} \quad (2.12)$$

with the exponential and limiting current:

$$I_{exp} = \mu_0 C_{ox} \frac{W}{L} V_{th}^2 \exp(1.8) \exp\left(\frac{V_{GS} - V_T}{nV_{th}}\right) \left(1 - \exp\left(-\frac{V_{DS}}{V_{th}}\right)\right) \quad (2.13)$$

$$I_{lim} = \frac{\mu_0 C_{ox} W}{2L} (3V_{th})^2 \quad (2.14)$$

Here:

- $V_{th}$  is the thermal voltage, usually in the order of 25 mV. It is a physical constant equal to  $kT/q$ , where  $k$  is the Boltzmann's constant,  $T$  is the absolute temperature, and  $q$  is the charge of an electron.
- $n$  is the subthreshold swing coefficient. It describes the steepness of the transition from the off state to the on state. Neglecting effects of biasing, it can be calculated via  $n = 1 + \frac{C_{dep}}{C_{ox}}$  [17], where  $C_{dep}$  is the capacitance of the depletion region (see section 2.2). It is usually in the order of 1.4 to 1.5. It has to be considered, that in the BSIM4 model,  $n$  is divided in further parameters, which are dependent on the substrate bias and  $V_{DS}$ , adding further complexity [19].
- $\exp(1.8)$  is an empirically chosen factor to achieve the best fit for the subthreshold characteristics within the model[19].

For a more detailed description, the model manuals and publications can be referred to under [20].

The full model allows for an accurate description of the MOSFET operation in the subthreshold region. However, the accurate modeling of the subthreshold current using the BSIM4 or any other advanced MOSFET model requires detailed calibration of the model parameters based on experimental data. Furthermore, the accuracy of these models can be affected by various factors, including process variations and operating temperature.

Considering this complexity, a simplified model is used for the studies in this thesis and is also known to be used in literature [15, 21]. This is described by the following equation:

$$I_D = I_0 \cdot \exp\left(\frac{V_{GS} - V_T}{nV_{th}}\right) \cdot \left(1 - \exp\left(\frac{-V_{DS}}{V_{th}}\right)\right) \quad (2.15)$$

While this model does not capture all the complex details of the subthreshold current behavior, it will provide a reasonable approximation that is sufficient for most purposes, with significantly reduced complexity.

Operating MOSFETs in the subthreshold region offers several advantages that make this mode highly suitable for silicon pixel detectors. Among the advantages

are low power consumption, minimized noise levels, enhanced tunability of the current, high gain, and reduced impact of short-channel effects [22]. These characteristics enable the optimal functioning of large-scale sensor arrays requiring a small power dissipation (see section 1.4).

Furthermore, the operation in subthreshold provides a high signal-to-noise ratio, improving the detector's sensitivity, while the current's exponential dependency on  $V_{GS}$  allows for precise tuning of device characteristics (see gain calibration in section 4.2). This can be used to increase the detector performance based on specific requirements, such as power consumption or speed.

It is still worth noting that the challenges of subthreshold operation, especially increased susceptibility to temperature changes and process variations (as variations in the dimensions of transistor components or doping fluctuations) and a reduced operating speed [22, 18].

## 2.4 Physics of particle detection in silicon sensors

Understanding the interactions of highly energetic particles traversing silicon sensors is crucial for the development of silicon pixel detectors. As charged high-energetic particles traverse the material, they interact electromagnetically with the atomic electrons, causing ionization and excitation of the atoms. This interaction leads to the transfer of energy from the incident particle to the material.

The mean energy loss per unit path length through ionization can be described using the Bethe-Bloch formula. However, it is important to note that even though the Bethe-Bloch formula was initially derived for all charged particles, it requires adjustments for electrons due to their lower mass and the presence of additional energy loss processes [23]. The Bethe-Bloch formula is given by:

$$\left\langle -\frac{dE}{dx} \right\rangle = Kz^2 \frac{Z}{A} \frac{1}{\beta^2} \left[ \frac{1}{2} \ln \left( \frac{2m_e c^2 \beta^2 \gamma^2 W_{max}}{I^2} \right) - \beta^2 - \frac{\delta(\beta\gamma)}{2} \right] \quad (2.16)$$

$z$ : charge of the incident particle, measured in terms of the elementary charge  $e$

$K$ : constant factor encapsulating several fundamental constants

$Z$ : atomic number of traversed medium

$A$ : atomic mass of traversed medium

$m_e$ : electron mass

$c$ : speed of light in vacuum

$I$ : mean excitation energy of traversed medium

$\delta$ : density correction of traversed medium

$W_{max}$ : maximum energy transfer in a single collision

$\beta = v/c$ : relative velocity of incident particle

$\gamma = \frac{1}{\sqrt{1-\beta^2}}$ : Lorentz factor of incident particle

The Bethe-Bloch formula is applicable in the context of moderately relativistic charged particles in the range of  $0.1 < \beta\gamma < 1000$ , where  $\beta\gamma$  is the momentum of the particle per unit charge.

In this range, the energy loss distribution reveals three different regions. For low momenta ( $0.1 \lesssim \beta\gamma \lesssim 1$ ), the energy loss decreases proportionally to  $1/\beta^2$  with increasing particle momentum. The minimum energy loss of a particle has its minimum at  $\beta\gamma$  values around 3 to 4, representing the region of minimum-ionizing particles (MIPs). However, for further increasing particle momenta, the energy loss initially increases due to relativistic rise, before the increase is damped at higher momenta. This counteracting to the relativistic rise of the energy loss results from the polarization of the medium—an effect described by the density correction term in the Bethe-Bloch equation.

Another limitation for the use of the Bethe-Bloch formula, apart from the particle momentum range, is the thickness of the traversed medium. While the Bethe-Bloch formula provides valuable information about the *mean* energy loss rate of a charged particle, the energy loss of particles traversing the sensor is not a distinct fixed value but follows a distribution due to statistical fluctuations. The nature of this distribution is described by probability density functions (PDFs). It is highly dependent on the thickness of the material through which the particle travels.

In the context of thin silicon sensors, those with thicknesses of a few hundreds of  $\mu\text{m}$ , the energy loss distribution is well described by the Landau model. One notable characteristic of the Landau distribution is its asymmetry, with a pronounced tail towards high energy losses. These high energy losses can be attributed to the generation of delta ( $\delta$ ) electrons, which are electrons resulting from the ionization in the detector material [24].

However, the Landau model reaches its limits when it comes to extremely thin silicon sensors with material thicknesses in the order of magnitude of  $100 \mu\text{m}$  and lower. Most Monolithic Active Pixel Sensors (MAPS) have a thickness of less than  $100 \mu\text{m}$  and can even reach thicknesses of tens of  $\mu\text{m}$ . For these ultra-thin sensors, the Bichsel model is the more suitable choice [25, 24].

### 2.4.1 Radiation damage effects in silicon

Silicon is commonly used in MAPS due to its superior electrical signal detection and processing properties. However, prolonged radiation exposure in high-energy physics experiments, such as those conducted at the LHC can cause significant damage to sensors and electronics, affecting the performance of MAPS [26, 27].

These modifications are especially concerning for the sensitive regions of a sensor, such as the pixel diodes and transistors.

**Radiation damage mechanisms** Radiation damage in silicon primarily occurs through two mechanisms: ionizing and non-ionizing radiation. Ionizing radiation results in electron-hole pairs in the silicon lattice, impacting the electrical properties material. Non-ionizing radiation, on the other hand, can displace silicon atoms from their lattice sites, creating defects that trap charge carriers and degrade the performance of silicon devices.

Ionizing radiation, quantified as Total Ionizing Dose (TID), refers to the process where incoming radiation ionizes the bulk material of the sensor, which includes the substrate and the epitaxial layer [27, 26]. This ionization process, under normal circumstances, is necessary for the proper functioning of the sensor and is usually reversible[27]. However, in the insulation layers of the in-pixel circuitry, ionization can cause irreversible damage. Here, the trapped charge from ionization can accumulate and lead to parasitic electric fields. These fields, in turn, can impact the functionality of the corresponding transistors, altering the working point of the affected pixel.

The NIEL mechanism appears when incoming particles collide with silicon atoms in the crystal lattice, causing displacements from their original positions. This process is mostly irreversible. Different particles interact with the silicon lattice in different ways, and the NIEL is used to compare the damage caused by different particle types and energies. Neutrons of 1 MeV are used as a reference, and the hardness factor  $\kappa$  is calculated to convert the physical fluence  $\Phi_{phys}$  into the neutron equivalent fluence  $\Phi_{eq}$  in the units of  $n_{eq}cm^{-2}$  [27]. These lattice defects create additional energy levels within the band gap of the silicon. The resulting effects are discussed in the following paragraph.

**Radiation damage effects** After a semiconductor has been irradiated, the leakage current can increase in relation to the temperature and the fluence of the radiation exposure. The temperature dependence of the leakage current is related to the increased generation of charge carriers due to the thermal energy provided at higher temperatures. In silicon bulk, the leakage current is shown to increase exponentially with the temperature [28]:

$$I_{leakage} \propto T^2 \exp\left(\frac{-E_g}{2k_B T}\right) \quad (2.17)$$

where  $T$  is the temperature,  $E_g$  represents the energy band gap of the semiconductor (for silicon 1.12 eV [27]), and  $k_B$  is Boltzmann's constant.

The fluence dependence of the leakage current arises from the presence of radiation-induced defects. These defects generate mid-gap energy levels, which allow for additional generation-recombination processes and therefore, an increased leakage current. This leads to a significant increase in the leakage current with increasing radiation dose [26]:

$$I_{leakage} \propto \alpha \Phi V \quad (2.18)$$

where the proportionality factor  $\alpha$  is called *current related damage rate*,  $V$  is the sensitive volume of the sensor and  $\Phi$  the fluence. This linear relationship of fluence and leakage current is illustrated in figure 2.4. There a linear relationship between the leakage current and the radiation fluence can be observed.

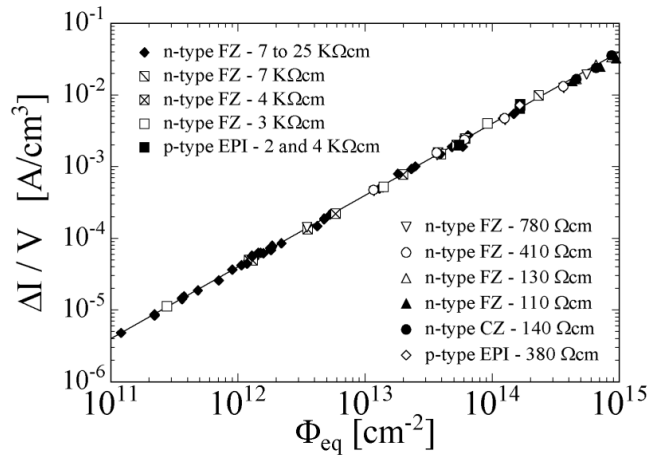


Figure 2.4: Fluence dependence of the leakage current for different silicon detectors process technologies[26].

Radiation damage-induced mid-gap energy levels contribute to another significant effect, referred to as charge trapping. These additional energy levels not only increase the thermal generation of free charge carriers but also increase the rate of recombination. Consequently, this results in the reduction of the lifetime of charge carriers. When a charge carrier is captured, it is effectively removed from the conduction process until it is released, which can decrease the efficiency of charge transport and cause signal loss in detectors. Charge trapping can therefore degrade the performance of the device over time and is a significant problem in the design of radiation hard devices [27].

High levels of radiation can cause another phenomenon known as *type inversion* in semiconductors. Starting with n-doped material, the effective doping concentration decreases up to a certain fluence. With further irradiation, the absolute effective doping concentration increases again, now dominated by acceptor-like defects with a negative space charge. The result is that the behavior of the material shifts from n-type to p-type. This effect is significant as it changes the basic opera-

tion of the device and can lead to problems in devices not designed to compensate for this type of change.

## 2.5 Working principles of MAPS

MAPS have a standardized structure designed to meet the requirements of particle and nuclear physics experiments. The structure of MAPS, illustrated through the transverse section of the ALPIDE detector as an example for this technology, is shown in figure 2.5.

The base layer of the ALPIDE detector is a heavily p-doped substrate, represented as  $p^{++}$ . This substrate acts as a reflective barrier for the electrons in the subsequent layer, influenced by the built-in voltage (further discussed in section 2.2). The middle layer, referred to as *epitaxial* layer, consists of a  $p^-$ -doped material and is primarily responsible for charge production and collection. Above this lies the n-type and p-type implants, the *n-wells* and *p-wells*, respectively. The n-wells that are in direct contact with the epitaxial layer serve as charge-collecting diodes. However, only the area around the collection diodes is depleted (as shown by the white region in Figure 2.5). This depleted region can be extended by applying a reverse bias voltage, denoted as  $V_{BB}$ . The standard operation of ALPIDE includes reverse bias voltages up to  $-6\text{ V}$ , with a nominal voltage of  $-3\text{ V}$  [29].

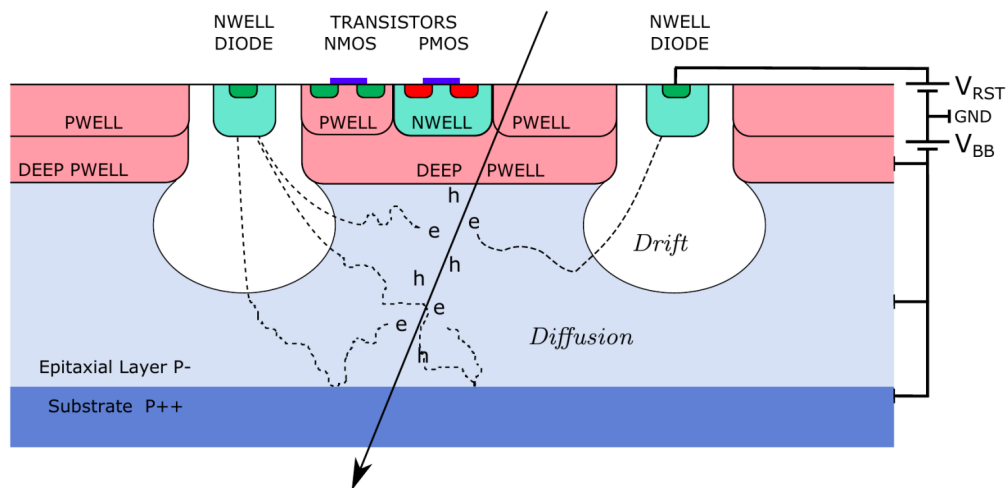


Figure 2.5: Schematic of a MAPS, not to scale. The diagram depicts p-type substrate and epitaxial layer (in blue), integrated electrical circuitry, n-type collection diode, and a deep p-type implant, referred to as deep pwell (ALPIDE specific). The biasing scheme is shown on the right, and a traversing ionising particle is indicated by a black arrow [10].

The signal voltage created from the collected electron charge  $Q_e$  can be evaluated using the pixel's input capacitance,  $C_{pixel}$ :

$$\Delta V_{signal} = \frac{Q_e}{C_{pixel}} \quad (2.19)$$

If a voltage drop  $\Delta V_{signal}$  appears at the input capacitance due to charge collection, a signal is registered as a hit, before the initial level of the signal voltage is restored. To distinguish signal hits from the general noise, a threshold voltage is defined in the operation of MAPS. A hit is identified when the signal amplitude exceeds this set threshold voltage.

The signal-to-noise ratio (SNR) is another important property that can be optimized by adjusting certain design parameters. The sensor performance improves with a higher SNR since the signal amplitude  $\Delta V_{signal}$  increases.

An important parameter for the sensor performance and the correct calibration of a sensor is the *Fake-Hit Rate* (FHR). This can be measured by taking a specific number of events  $N_{event}$  and recording the number of hits  $N_{hit}$  in the absence of an external signal [30]. The FHR is defined as:

$$FHR = \frac{N_{hit}}{N_{pix} \cdot N_{event}} \quad (2.20)$$

In the case of the ALPIDE detector, a extremely low FHR of  $10^{-8}$  was measured, demonstrating the precision and efficiency of this sensor (see section 1.3).

# Chapter 3

## ITS3 pixel test structures

The ITS2, with the ALPIDE chip as its fundamental building block, has achieved outstanding performance within ALICE, as elaborated in section 1.3 [5]. As a result, there has been a growing interest in further developing this technology across various high-energy physics experiments. Furthermore, ALICE is planning an additional upgrade, the ITS3 (refer to section 1.4). This upgrade requires a significantly reduced material budget, a wafer-scale sensor design, and increased robustness against radiation damage, to name a few challenges. These requirements highlight the need for an innovative sensor design to meet the specific objectives and constraints of the ITS3 upgrade.

To realize this goal, an extensive R&D program focusing on the fabrication of MAPS sensors using sub-100nm technologies was started in a joint effort with the CERN experimental physics (EP) department in collaboration with several additional institutes [31]. After the analysis of viable technologies, the TPSCo 65 nm ISC imaging CMOS technology [9] was identified as the optimal candidate, with the benefits discussed in section 3.1 [32]. The first prototype submission fabricated in this technology is the Multi-Layer per Reticle run (MLR1). The primary objective of the MLR1 in this early stage is to investigate the charge collection properties, assess the radiation hardness, and evaluate the detection efficiency of this technology.

### 3.1 Multi-layer per reticle run

One of the primary advancements of the new MLR1 design is the reduction in transistor size, exploiting the capabilities of the 65 nm technology. The reduction in size enables the creation of smaller pixels while maintaining the complex functions within each pixel. MLR1 offers pixel pitches in a range between 10 to 25  $\mu\text{m}$ , providing options for optimizing the sensor resolution and its charge collection properties. Additionally, the availability of larger wafer sizes (300 mm, compared

to 200 mm in TowerJazz 180 nm process [9]) is a critical aspect of the ITS3 design requirements (refer to section 1.4).

Another crucial aspect towards the ITS3 upgrade is the possibility to thin down the sensor, reduce the material budget, and enhance the flexibility of the material, thus simplifying the bending process to achieve the required radii, as outlined in section 1.4. During this process, the thickness of the epitaxial layer is significantly reduced, going from 25  $\mu\text{m}$  to approximately 10  $\mu\text{m}$ . Consequently, these newly processed wafers are characterized by this 10  $\mu\text{m}$  epitaxial layer, which inherently restricts the expansion of the depletion region more than in the case of 25  $\mu\text{m}$ . To compensate for this, various implant geometries and doping concentrations were initially tested with the 180 nm technology before being applied to the 65 nm technology [33, 32]. Figure 3.1 shows the three different geometries the MLR1 sensors were fabricated in, the *Standard process*, *modified process*, and *modified process with gap*.

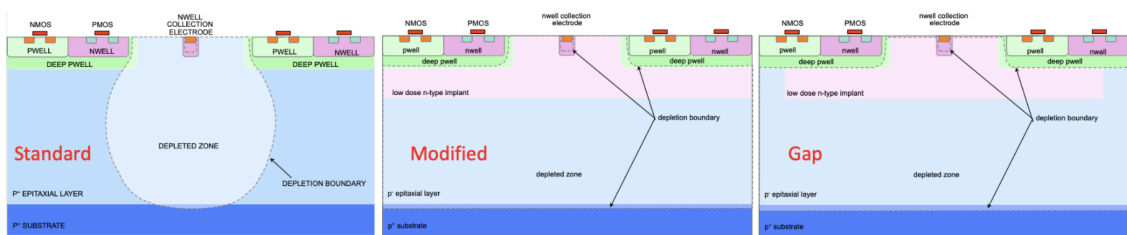


Figure 3.1: Schematic representations of the three implant geometries, the MLR1 run was fabricated in [34].

In order to meet the radiation hardness requirements of the ITS and future experiments (see section 1.4), a sensor with full depletion of the sensitive volume is advantageous to minimize charge loss, particularly after substantial radiation damage. In case of a full depletion, the high drift-field in the depleted volume ensures a large signal even after irradiation. In contrast, in undepleted regions of the epitaxial layer, charge carriers move via diffusion. Furthermore, radiation-induced charge trapping significantly reduces detection efficiency, as discussed in 2.4.1.

While the *Standard process* has a similar implant geometry as the ALPIDE (section 1.3.2), the *modified process* includes a low-dose doped n-type layer within the epitaxial silicon. The depletion begins to form at the interface between the n-type layer and the p-type epitaxial layer, with this junction equally formed under the deep p-well. The sensor junction is planar and extends over the full pixel width, and with sufficient reverse substrate bias, full depletion can be achieved, as shown in figure 3.1. Furthermore, the depletion will reach the n-well collection

electrode, resulting in a small capacitance for the electrode and hence increased signal amplitude (see section 2.2 and 2.5).

A different variant of the process has also been developed, termed the *modified process with gap*. This variant introduces a gap in the low-dose n-type implant at the pixel boundaries. The aim of this modification is to enhance charge collection at the pixel edges and corners. This is achieved by generating a stronger lateral field caused by the gap. This focuses the drift of the generated free charge carriers towards the collection electrode. This reduced the risk of charge trapping in this region and hence improves the efficiency of the sensor in the pixel edges. This modification not only optimizes the performance of individual pixels but also ensures a more uniform response across the entire sensor surface.

Furthermore, the charge sharing is significantly reduced from the standard process to the modified process and is further decreased in the modified process with gap. As a result, the signal of the seed pixel<sup>1</sup> is increased. This enhancement arises from the fact that the charge is no longer distributed across multiple pixels but rather collected predominantly in a single pixel. This increase of signal yield in the seed pixel improves the overall detection efficiency [32, 34].

Within the scope of the MLR1 submission, various pixel test structures were developed to probe and analyze distinct aspects of the technology. Figure 3.2 illustrates these three different test structures, each measuring  $1.5 \times 1.5 \text{ mm}^2$ . The first chip, known as *Analog Pixel Test Structure (APTS)*, contains a  $6 \times 6$  pixel matrix with a pitch of  $10 \mu\text{m}$  to  $25 \mu\text{m}$ , whereby the central  $4 \times 4$  pixels are connected through an analog buffer chain [12]. The second chip, *Digital Pixel Test Structure (DPTS)*, includes a  $32 \times 32$  pixel matrix with a pitch of  $15 \mu\text{m}$ . Each pixel in the DPTS has an amplifier and discriminator, and the readout is time-encoded and digital [35]. The third chip, CE65, contains multiple pixel matrices, collectively forming a  $32 \times 48$  pixel array. This chip features an analog readout, and its pixel matrix is readout with a rolling shutter [36].

## 3.2 APTS characteristics

This study will focus on the APTS. The primary objective of this test structure is to evaluate the charge collection properties, detection efficiency, and spatial charge distribution of this new technology. Moreover, investigating the radiation hardness is an important aspect of the study, as it is a critical requirement for the ITS3 ( $10^{13} \text{ 1 MeV n}_{\text{eq}}\text{cm}^{-2}$  NIEL and  $10 \text{ kGy}$  of TID) and further experiments (up to  $10^{16} \text{ 1 MeV n}_{\text{eq}}\text{cm}^{-2}$  of NIEL) to achieve (refer to section 1.4) [34, 32, 13]. As mentioned above, APTS measures  $1.5 \times 1.5 \text{ mm}^2$  and has a comparably small  $4 \times 4$

<sup>1</sup>The seed pixel is the pixel within a cluster that has accumulated the highest amount of charge.

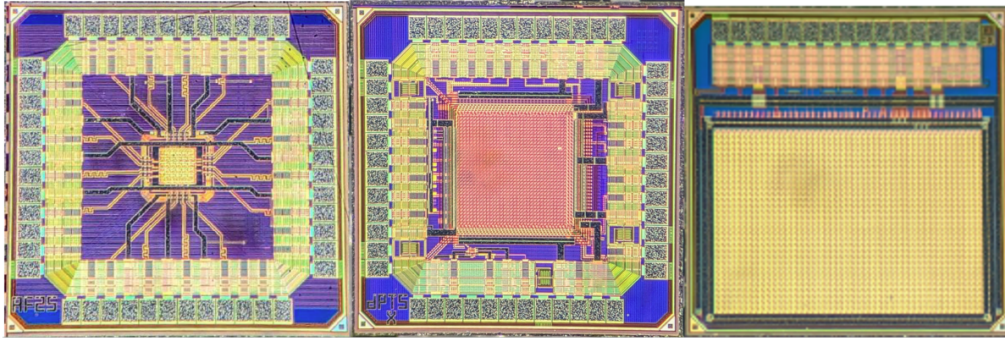


Figure 3.2: Microscope pictures of the different test structures implemented on the first MLR1 run, namely the (a) the analog pixel test structure (APTS) [37] (b) the digital pixel test structure (DPTS) [35] and (c) the CE65 [36].

matrix with analog outputs for each pixel, directly buffered to output pads to be able to observe the complete signal evolution of the 16 pixels in parallel. In the MLR1 run 34 APTS variants have been fabricated, each investigating diverse attributes in terms of pixel size, design, and process variants, reverse biasing schemes, and peripheral analog output buffering [37, 12].

The primary focus of this study is the DC coupled source follower version, with a pixel pitch of  $15\ \mu\text{m}$  and the modified process with gap (refer to figure 3.1), as this version showed promising results in terms of signal charge collection and detection efficiency in earlier conducted studies [32]. These sensors are denoted with the abbreviation AF15\_PW22 and more details to this version are outlined in the following section.

### 3.2.1 Architecture

Figure 3.3 shows the architecture of the APTS front-end circuit. It buffers the signal from the electrode towards an output pad. This buffering procedure is performed partly within the pixel itself and partly within the periphery of the sensor matrix. The process of biasing and resetting the collection electrode is controlled by the PMOS transistor M0, a function which is elaborated on in greater detail in section 3.2.2. The DC voltage on the collection electrode approximates the voltage configured at the source of M0, represented as  $V_{reset}$  in figure 3.3. The rate at which the sensing node resets subsequent to a signal is driven by the reset current parameter  $I_{reset,set}$ . The substrate ( $P_{sub}$ ), as well as the bulk of the NMOS transistors ( $P_{well}$ ) in each pixel, is biased with a negative bias voltage, referred to as *back bias voltage*  $V_{BB}$ .

The in-pixel circuit, containing two source-follower stages, maintains a DC connection to the collection electrode. These stages consist of a p-type follower (M1 and

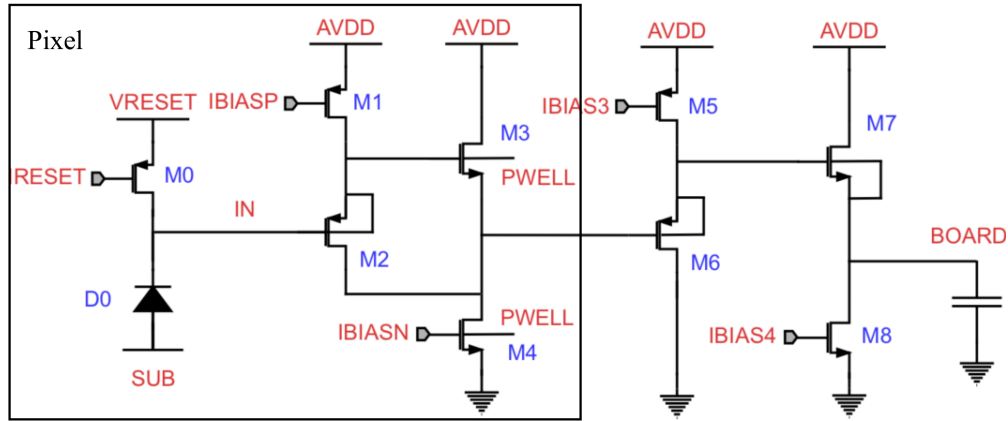


Figure 3.3: Schematic of APTS source-follower version circuitry [12].

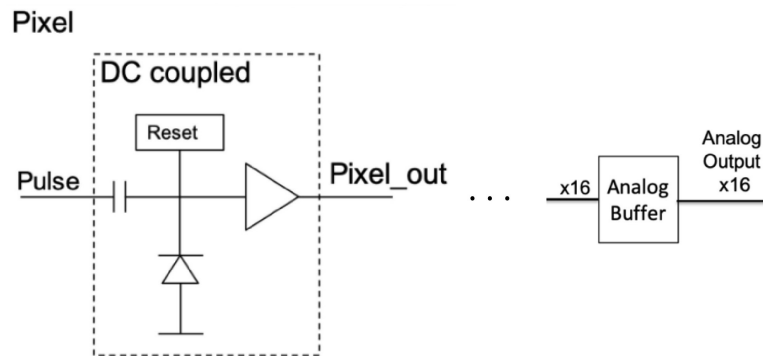


Figure 3.4: High level functional block diagram for the DC coupled APTS [12], with modifications to the figure

M2) and an n-type follower (M3 and M4), which are controlled by the currents  $I_{biasp}$  and  $I_{biasn}$ , respectively. The output from the n-type follower stage is linked directly to the drain of the input transistor of the initial stage. This connection allows both the source and the drain of the input transistor within the readout chain to mimic the voltage signal on the collection electrode. Using this source-follower circuit minimizes the capacitance load on the collection electrode, thereby supporting to conserve its low capacitance.

An additional pair of source-follower stages (M5, M6 and M7, M8), controlled by  $I_{bias3}$  and  $I_{bias4}$ , connect the matrix outputs with the analog output pads. Off-chip, the signals are probed on a high-impedance node.

Additionally, each pixel is equipped with a test circuit, enabling capacitive charge injection into the collection electrode.

The pixel is equipped with a test circuit that enables capacitive charge injection into the collection electrode. The chip's block diagram, including the pulsing, is

displayed in figure 3.4. The quantity of charge injected can be modulated via the voltage setting  $V_H$ .

The working point is an essential aspect that must be finely tuned for optimal performance. Parameters involved in this tuning process can be categorized into two groups: those that are generally static for a given sensor variant and those that require adjustment depending on the use case. For instance, the biasing of the source-follower stages is usually fixed, while the back bias voltage  $V_{BB}$  and the set reset current  $I_{reset,set}$  play critical roles in the fine-tuning of the sensor performance. The possible operating range and the values at the typical operating point for all parameters are summarized in table 3.1 [12]. The studies to find the operating point are presented in [37].

Parameter	Comments	Typical value	Unit
AVDD	Power voltage	+1.2	V
VH	Pulsing bias	+1.2	V
Front-end bias			
IBIASP	1/4 mirror ratio	+2	$\mu\text{A}$
IBIASN	1/4 mirror ratio	-20	$\mu\text{A}$
IRESET	1/10 <sup>4</sup> mirror ratio	+1	$\mu\text{A}$
VRESET		+500	mV
Source follower bias			
IBIAS3	1:1 mirror ratio	+200	$\mu\text{A}$
IBIAS4	1:1 mirror ratio	-150	$\mu\text{A}$
Well bias			
PWELL	Pwell bias voltage	-2.4	V
SUB	P-substrate bias voltage	-2.4	V

Table 3.1: Operating values for parameters of the APTS source-follower version shown in figure 3.3. The mirror ratio represents the proportion of the current in the bias circuit to the current in the front-end circuit. During lab measurements, both well biases are commonly set to the same voltage between 0 V to  $-4.8$  V.

#### 3.2.2 Signal Processing

In sensor circuits, the reset transistor is crucial for initializing the sensor to a known state before measurement. When the reset transistor (M0) is turned on, it allows current to flow from the drain to the source, effectively discharging the collection electrode. This process sets the voltage to a known reference level, typically the reset voltage ( $V_{reset}$ ). This resetting to the reference level, which is also referred to as the baseline, is crucial for ensuring that the transistor remains within its optimal operating conditions.

The reset current  $I_{reset}$  through M0 determines how quickly the sensor element is reset to baseline, hence defining the signal shape. This current can be adjusted by tuning the  $I_{reset,set}$  parameter. The measured reset current  $I_{reset}$  is also influenced by various factors like temperature and process variations, which is why it's considered proportional and not equal to the set parameter  $I_{reset,set}$ . These contributing factors are discussed in greater detail in the sections 2.3 and 5.1, respectively.

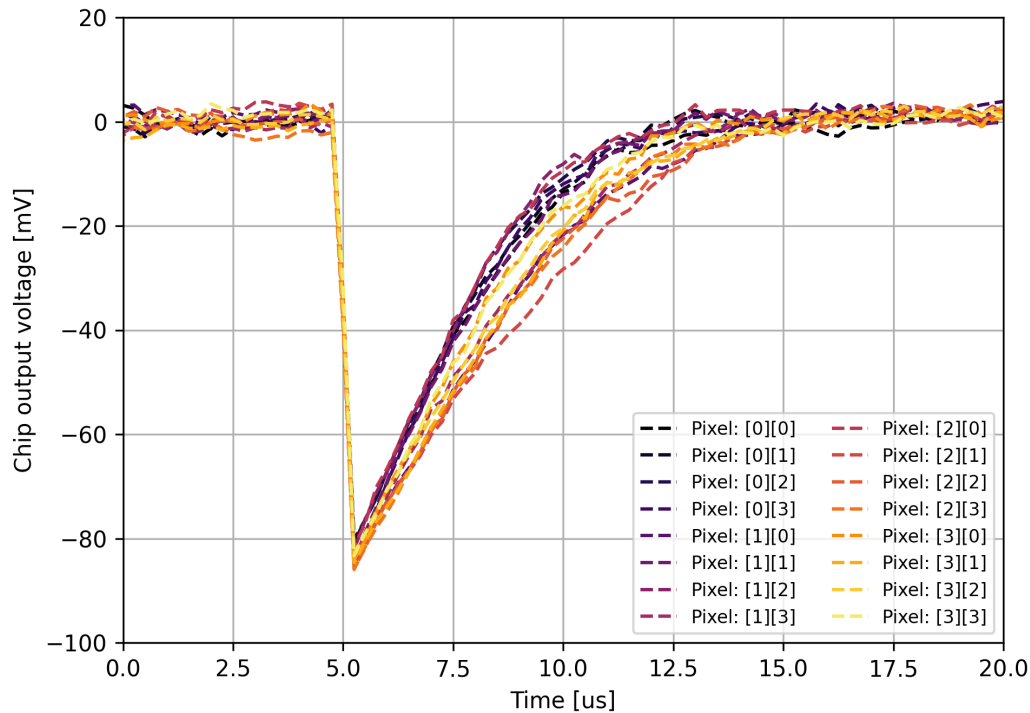


Figure 3.5: Signal shape distribution across the 16-pixel matrix of the APTS, showcasing the dispersion among the pixels. The depicted pixel coordinates define the pixel position in terms of rows and columns.

Figure 3.5 provides a visualization of the signal obtained through charge injection across the pulsing capacitance (242 fF [12]) for the 16 pixels of an APTS. The figure reveals distinct phases in the pulse shape. Data points for each pixel are acquired in intervals of at least 250 ns. Initially, before any charge injection takes place, the signal remains constant at the reference voltage, with only minor fluctuations due to noise. In this representation, the reference voltage has been standardized to 0. At around 5 microseconds, charge injection commences, causing a visible voltage drop in the signal. Subsequently, the reset current starts to drive the signal back toward the baseline. The signal gradually returns to the reference voltage. Small variations in the signal between the pixels are observable, which can be attributed to slightly different reset currents across the pixels. This return to the

### 3.2. *APTS CHARACTERISTICS*

---

reference voltage demonstrates the role of the reset current in reestablishing the initial conditions for the next charge deposit.

# Chapter 4

## Data acquisition and signal calibration in laboratory measurements

In this chapter, a comprehensive description and first qualitative analysis steps of the laboratory measurements conducted to evaluate the sensor performance and characteristics are provided. This assessment is crucial in order to understand the influence of (biasing) parameters on the output signal. As such, results from laboratory measurements is used as input for chip designers to further develop the sensor and ensure its required functionality and reliability within the foreseen application in an experiment.

### 4.1 Experimental setup

Figure 4.1 shows the main components of the used APTS setup. These are, the DAQ board (red), a proximity board (green), and a carrier board (blue). The latter hosts the MLR1 sensor and serves as a rudimentary electrical interface between the chip to the test system. The proximity card is used to route and adjust steering signals from the DAQ board to the chip voltage and current standard. The last instance of the main DAQ system is the DAQ board, which sets the operating point of the chip and reads the pixel output signals via ADC. The DAQ board controls the system via an integrated *Field Programmable Gate Array* (FPGA). Details for all currents and voltages applied on the sensor are depicted in section 3.2.1.

The complete test system comprises also a computer and a low-voltage power supply, for powering DAQ board, proximity, applied reverse bias, and the chip itself. Additionally, in order to control the temperature of the sensor a *huber minichiller* [39] and an aluminum cooling jig, enclosing the carrier board, were

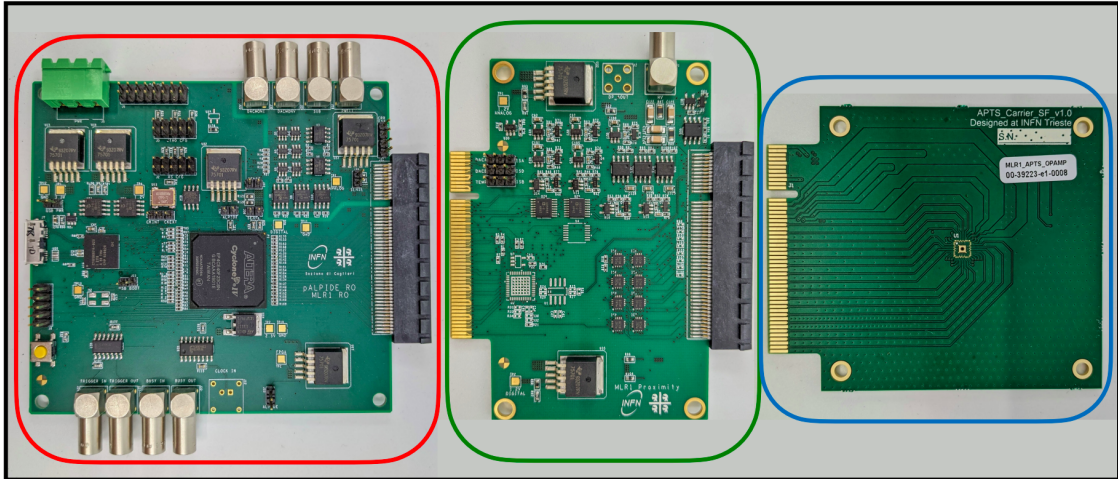


Figure 4.1: APTS laboratory setup, showing the three main components, namely the DAQ board (red), the proximity board (green), and the carrier card (blue) which the APTS is bonded to. [38]

used. The heat generated by power dissipation in the sensor is transferred to the cooling water. Consequently, this process stabilizes the temperature of the chip, allowing for control over its temperature via the *Huber Minichiller*. For the purpose of performing different lab measurements with necessary temperature control, e.g. temperature studies or source measurements (see section 4.7), the jig was custom-created at CERN, for the setups of the MLR1 prototypes, as shown in figure 4.2. Lastly, to shield the APTS setup from light sources and potentially introducing noise to the measured signal, a black cloth is used to cover the setup. Several different measurements can be conducted to study the response of the APTS, some of which are discussed in the subsequent chapters. For this purpose, the data acquisition and analysis software developed by the ALICE ITS3 collaboration is used. One of the goals of this work is the development of a stable method to determine the leakage current in APTS sensors. Traditional methods, such as I-V curve analysis, failed to perform for these devices as other currents than the leakage current are dominating in those measurements. This is making it crucial to develop a new approach. See chapter 5 for more details.

## 4.2 Signal injection via pulsing

There are two possibilities of triggering, first, externally through an external trigger, and second, internally. An internal trigger triggers on the APTS signal itself, e.g. from a radioactive source<sup>1</sup>. Moreover, it is also possible to pulse the chip (refer to

<sup>1</sup>After a minimum amplitude is reached, an adjustable amount of time frames before and after the trigger can be saved, usually 100 frames before and after



Figure 4.2: Setup with a cooling jig and with (right) and without (left) blanket for light protection during measurements. As the cooling jig is used for multiple purposes, it features a cutout for holding a radioactive source. Additionally, the biasing, powering connections, and cooling water tubes are shown.

chapter 3). The signal obtained from the APTS corresponds to the signal voltage measured in ADC units within time intervals of at least 250 ns. Together with the trigger and the APTS signal, the signal shape and internal processing of the charge are studied to evaluate if the technology and the design meet the requirements of future experiments (see section 1.4) or needs to be optimized based on the findings. Additionally, using the analog information quantities like the effective reset current can be derived, see section 5.3.

The following paragraphs, therefore, focus on and explain central topics linked to data acquisition via charge injection (pulsing).

**Gain calibration** The signal voltage and therefore the pulse amplitude and shape (waveform) are measured (figure 4.3) in ADC units. These ADC units need to be calibrated in order to convert the measured values back to mV to be able to interpret the signal pulse at the input node (compare figure 3.3). This step allows to separate any effects due to different gains (i.e. chip to chip or pixel to pixel variation, caused by the source follower) from the sensor behavior itself. An approximate conversion factor of ADC to mV is known to be approximately 0.0381 in the operating regime. However, since the sensor's behavior depends on environmental conditions such as temperature (one of the investigated parameters

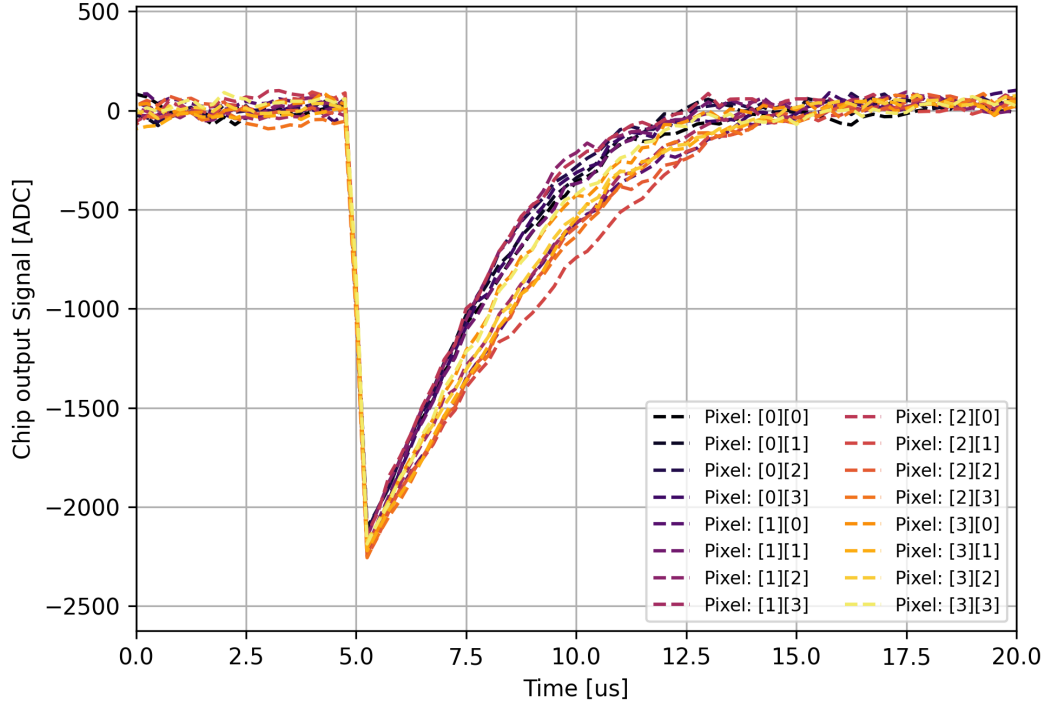


Figure 4.3: Uncalibrated signal pulses of all 16 pixels from a non-irradiated APTS sensor.

in this thesis) a more sophisticated calibration is needed to determine the precise conversion factor. First, the signal is measured at different values for  $V_{reset}$ , which is the biasing voltage for the reset transistor and hence represents the baseline voltage, as detailed in section 3.2.1. This baseline is measured in ADC units for varying values of  $V_{reset}$  (figure 4.4, left). The calibration is based on these measurements, where the measured ADC baseline unit is mapped to the corresponding  $V_{reset}$  voltage in mV. For quality assurance purposes, the numeric derivative of the relation of the baseline to  $V_{reset}$  is calculated (figure 4.4, right).

It represents the linearity of this relationship, giving rise to the calibration factor, which links signal voltage and measured ADC counts at each point. The derivative is required to be as constant as possible since the sensor should operate in a linear region. Operating in a non-linear regime can lead to problems in the energy calibration. An example for a calibrated signal pulse can be seen in figure 3.5. The main distinction from the uncalibrated pulses is the conversion factor, which remains relatively consistent across the entire signal voltage range and all pixels, as shown in figure 4.4. Therefore, no significant difference in the signal shape is apparent.

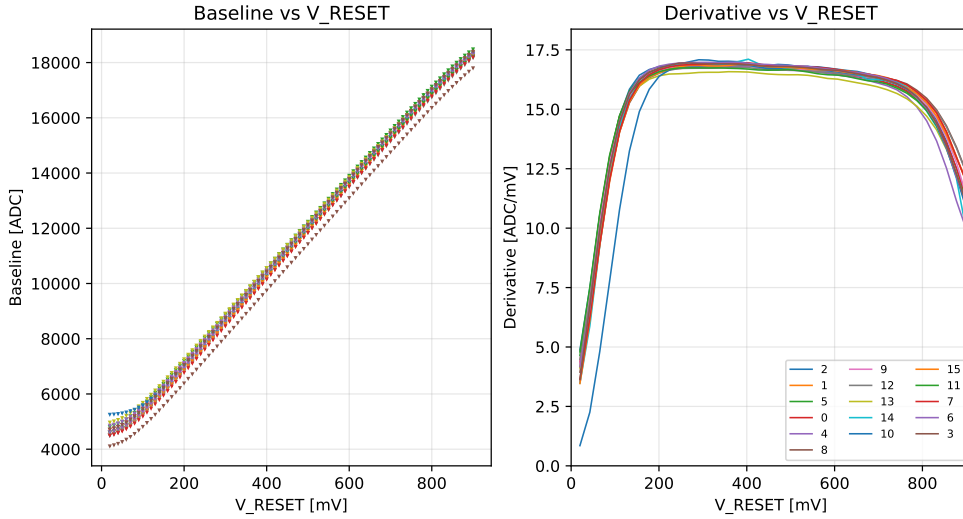


Figure 4.4: Gain calibration plots. Mapping of the baseline value in ADC unit to the  $V_{reset}$  voltage in mV (left) and derivative of it, meaning the conversion factor (right) is shown.

**Pulsing average** The calibrated signal waveforms are now ready to be recorded and evaluated quantitatively. As illustrated in figure 4.5, a sample of these recorded waveforms is presented. It's noticeable that individual waveforms are subject to noise interference. The average of the waveforms is taken to smooth out the statistical fluctuations introduced by thermal and electronic noise. In detail, this involves taking 1000 pulses for each measurement to ensure the reproducibility of the results. This process is carried out for each pixel individually to account for potential variations across different pixels. In figure 4.5 the 1000 waveforms are marked in grey, and in blue the averaged pulse is shown. For simplification reasons, only one pixel is illustrated. Moving forward, the terms 'pulse' and 'waveform' will refer exclusively to the gain-calibrated and averaged signal pulses associated with one pixel.

### 4.3 Systematic parameter measurements

With the previously described calibrated waveforms, different measurements can be taken by either varying environmental conditions or the sensor biasing parameters. In the ITS3 upgrade, the sensor has to withstand much higher temperatures due to the required air-cooling (see section 1.4), which is less effective (but also less material budget consuming) compared to water-cooling [7]. Hence, it is essential to examine the sensor performance for different temperatures as a crucial environmental factor. Taking the lab environment and factors such as the

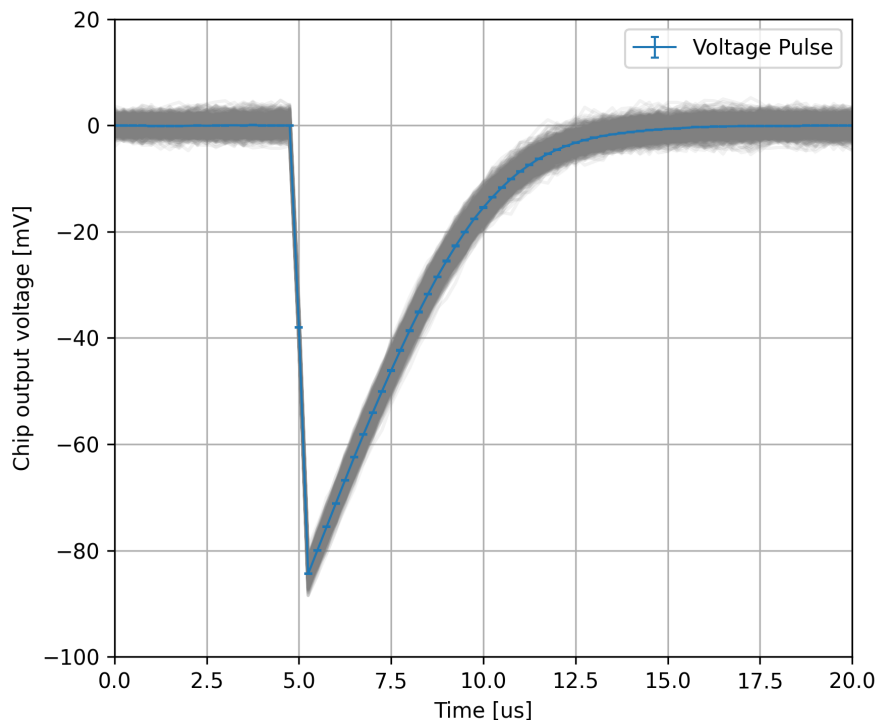


Figure 4.5: Calibrated signal pulses of one pixel from a non-irradiated sensor. 1000 individual pulses are depicted in grey, while the blue line represents the average pulse signal.

dew point into consideration, a temperature range of 15 °C to 40 °C was chosen for testing the sensors. In addition to examining the temperature behavior of the sensor in general, the temperature measurements are also crucial to investigate the temperature dependence of the leakage current, which is especially present in irradiated sensors (see chapter 5).

Besides the temperature, additional sensor parameters are tested, which are explained in more detail in section 3.2.1. For example, parameters affecting the signal shape are  $V_{reset}$ , controlling the baseline,  $I_{reset,set}$ , controlling the reset current, and  $V_{BB}$ , controlling the reverse bias voltage (also called *back-bias*), which is applied on the substrate and the pwell (see figure 3.3). Additionally, the influence of different  $V_H$  is of interest, as it regulates the amount of charge injected during the pulse injection. Parameters not mentioned, such as the biasing of the source-follower stages, are not changed as they do not affect the signal shape itself, but the gain, which is shown to be at an optimal working point for the APTS at the values depicted in table 3.1. All the above-mentioned parameters can be varied in a certain range without compromising the sensor performance significantly. However, their effect on the signal shape is not negligible and therefore important to be investigated to test the limits of the sensor performance.

The investigated ranges of the parameters are listed in table 4.1. For  $I_{reset,set}$ ,  $V_{BB}$  and the temperature all possible combinations were examined, while for  $V_{reset}$  and  $V_H$  only a subset of parameter combinations is measured. These parameters were tested on different sensors having received different radiation doses ranging from  $10^{13}$  1 MeV  $n_{eq}$   $cm^{-2}$  to  $10^{16}$  1 MeV  $n_{eq}$   $cm^{-2}$  for irradiation with neutrons.

Parameter	Measurement Range	Stepsize
Temperature	15–40 °C	5 °C
$I_{reset,set}$	10–250 pA	10 pA
$V_{BB}$	0–4.8 V	0.6 V
$V_{reset}$	200–900 mV	100 mV
$V_H$	0.2–1.2 V	0.1 V

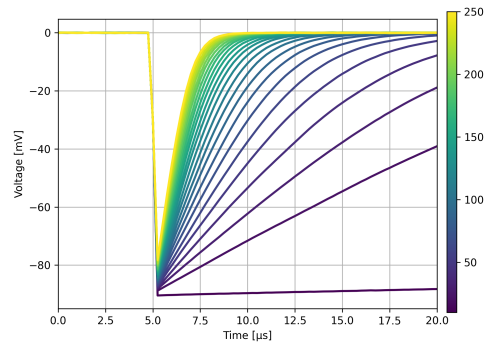
Table 4.1: Measurement ranges of sensor biasing parameters and temperature

In practice, the measurements are executed by first setting the desired temperature on the chiller. After the temperature is reached, the carrier board and silicon sensor are given 15 min to thermalize. Next, all pulsing measurements are performed for all required sets of parameters. After measurements were performed for all parameter combinations, the externally applied  $V_{BB}$  is changed to take the same type of measurement with the changed  $V_{BB}$ . The process is repeated for the remaining temperatures and subsequently for all sensors to be tested.

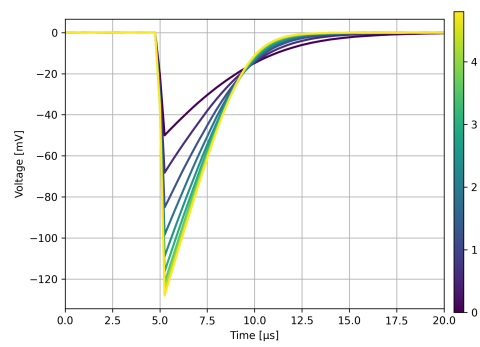
## 4.4 Pulse shape dependence on sensor parameters

The effect of each biasing parameter on the pulse shape is summarised in figure 4.6. Here, each panel represents the change of the pulse shape with the variation of the corresponding parameter. The color scale indicates the parameter value, with low parameter settings represented in blue and high settings in yellow. In the following, a detailed discussion of each of the parameters under investigation is given.

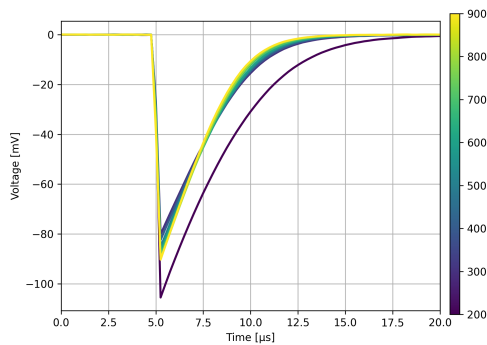
**Reset current parameter** By varying the reset current  $I_{reset,set}$ , the most significant change to the signal shape is achieved, as can be seen in figure 4.6 in the upper left panel as compared to the other panels. With very low reset currents, the signal pulse is driven back to the baseline very slowly, appearing even to be reset with a constant factor, instead of an exponential. As the reset current increases (towards yellow in figure 4.6), the signal progressively returns to the baseline, exhibiting an exponential behavior. This behavior will be explained in more detail in the following chapter 5.



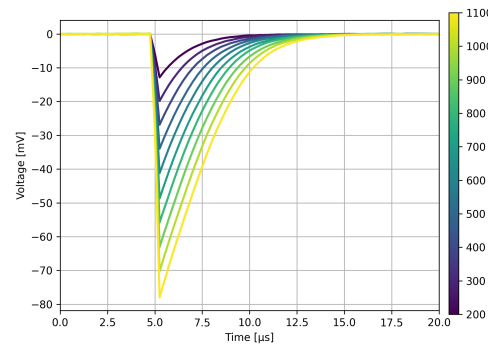
(a) Pulsing  $I_{reset,set}$  dependence



(b) Bias Voltage  $V_{BB}$  dependence



(c) Reset Voltage  $V_{reset}$  dependence



(d) Pulsing Bias Voltage  $V_H$  dependence

Figure 4.6: Effect of different biasing parameters on the pulse shape.

Another aspect that must be considered is the peak height, which is reduced with increasing  $I_{reset,set}$ . This can be explained by the sampling rate (4 MHz). As the reset current increases, the return to the baseline is faster, reducing the signal voltage already before the measurement of the frame with the peak of the signal amplitude.

**Reverse bias voltage** Varying  $V_{BB}$  also yields a significant change in signal shape. On the one hand, the signal amplitude increases with increasing applied voltage. On the other hand, the signal is reset faster to baseline with an increasing voltage, even though the amplitude is significantly larger, indicating an increasing reset current.

As the reverse bias voltage increases, the depletion region extends, as discussed in section 2.2. This change in the depletion region affects the junction capacitance. As the depletion region widens with increasing reverse bias, the junction capacitance and, consequently, the total sensor capacitance decreases, leading to higher amplitudes [37, 18]. The change of the reset current is shown and discussed in more detail in section 4.5.

**Reset Voltage** At 200 mV, the reset voltage is outside of the optimal operating range, as observed during calibration (see 4.2). Being outside of the linear region of Signal Baseline and reference voltage ( $V_{reset}$ ), it deviates from the expected behavior. For the remaining range, there is a slight variation in the reset current. A higher reset voltage accelerates the reset process. This phenomenon can be understood by the transistor equation 2.15, where increasing the gate-source voltage  $V_{GS}$  increases the reset current.

**Pulsing Voltage** The pulsing voltage, denoted by  $V_H$ , dictates the amount of charge injected during the pulsing phase. Therefore, as  $V_H$  increases, linearly increasing signal amplitudes are expected, which is consistent with the observations. Apart from this, no significant effect on other parameters such as pulse shape or reset current is observed.

## 4.5 Dependence of effective reset current on applied bias parameters

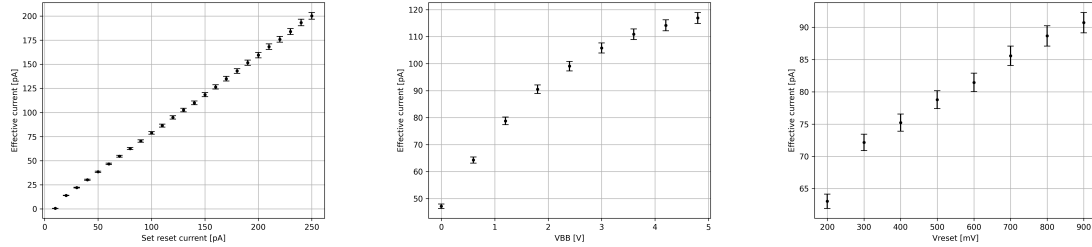
As many parameters significantly affect signal resetting, it is worth investigating the correlation of those parameters with respect to the determined effective reset current. The effective reset current drives the signal back to baseline and can be determined by analyzing the pulse shape, as elaborated in chapter 5. It is linearly proportional to the adjustable reset parameter  $I_{reset,set}$ . Not all effects on the signal can be observed from the signal shape itself, therefore the effective reset current can be used to measure dependencies of parameter variations. The results are presented in the following section.

Figure 4.7 shows the relations for  $I_{reset,set}$ ,  $V_{BB}$ , and  $V_{reset}$  to the effective reset current. For  $I_{reset,set}$ , a linear correlation to the effective reset current is apparent. However, it is notable that the effective current is not equal to the reset parameter. This deviation is reasoned by the process-dependent factors that tend to vary, as discussed in section 5.1.

With increasing  $V_{BB}$  also the effective reset current increases. The increase is larger and low  $V_{BB}$  voltages seem to approach a maximum close to the maximum applied reverse bias. Naively, no increase in reset current is expected, as it solely depends on the characteristics of the reset transistor. However, the reverse bias is shown to affect its threshold voltage  $V_T$  via the body effect, which is described in the BSIM model for the transistor current as indicated in section 2.3 [15, 18]. Consequently, this can affect the reset behavior leading to an increased reset current due to the exponential dependence of the reset current to  $V_T$  and  $V_{GS}$ . Lastly,  $V_{reset}$  indicates a

#### 4.6. LABORATORY MEASUREMENTS OF IRRADIATED SENSORS USING PULSING

roughly linear relation in the operating regime, higher than 200 mV. An increasing reset current is expected in this case, as the reset voltage directly influences  $V_{GS}$ , increasing the reset current.



(a) Pulsing  $I_{reset,set}$  dependence (b) Bias Voltage  $V_{BB}$  dependence (c) Reset Voltage  $V_{reset}$  dependence

Figure 4.7: Dependency of the effective reset current on different biasing parameters.

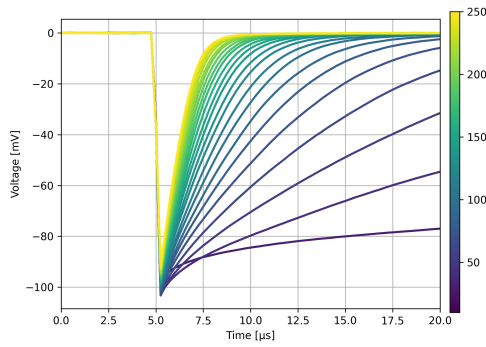
## 4.6 Laboratory measurements of irradiated sensors using pulsing

Until now only the signal shape of non-irradiated sensors has been investigated. In the following a similar analysis is done for irradiated sensors in order to validate similar behavior, i.e. the same test procedures can be applied. As previously mentioned, irradiation levels of up to  $10^{16}$   $1 \text{ MeV } n_{eq} \text{ cm}^{-2}$  are investigated within the scope of this thesis. Figure 4.8 summarises the findings of these laboratory measurements for a sensor having received  $10^{15}$   $1 \text{ MeV } n_{eq} \text{ cm}^{-2}$ . The upper row shows the set reset current  $I_{reset,set}$  (a) and reverse bias voltage  $V_{BB}$  (b) against the signal voltage while the lower row shows  $I_{reset,set}$  and reverse bias voltage  $V_{BB}$  against the effective reset current.

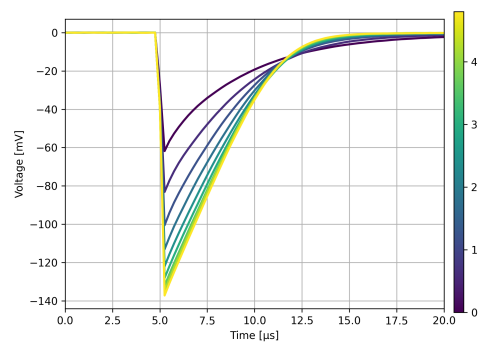
Over a wide range of values for the parameters, the pulse shape behavior of the irradiated sensor is very similar to the non-irradiated one. Having a closer look at low reverse bias and reset current parameters (indicated in blue in the plots), it is apparent that the signal behaves differently. While the voltage seems to be driven back with a constant rate in the non-irradiated case, it appears to reset very fast in the first  $1-2 \mu\text{s}$ , before a similar constant reset to the non-irradiated case sets in. This effect is most significant in the case of the lowest  $I_{reset,set}$  setting, which is 30 pA, here corresponding to an effective current of less than 10 pA (see figure 4.8c). This behavior indicates a second possibly exponential dependence of the signal amplitude of the resetting current with a comparably short time constant and low impact, as it is only significant at effective reset currents smaller than

30 pA. A possible reason for this effect could be discharge effects in the circuitry. Such a behavior is not expected as also reassured in discussions with Dr. Snoeys in the field of electrical engineering, who is involved in the developing of the MLR1 run [32]. Hence, this altered signal behavior for high irradiation doses requires further investigation.

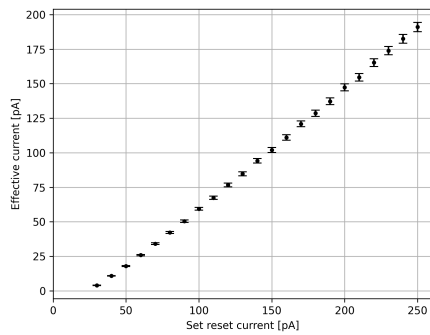
Nevertheless, from the relation of the parameters to the effective current, a comparable behavior to the non-irradiated sensor is apparent, indicating that the overall behavior of the sensor is still comparable. The only difference in relation to  $I_{reset,set}$  is the offset from the origin with a general shift towards a lower effective current. This behavior is thoroughly discussed in section 5. In determining the effective reset current, this irradiation effect is accounted for by excluding the first frames from determining the effective reset current, as described in section 5.3.



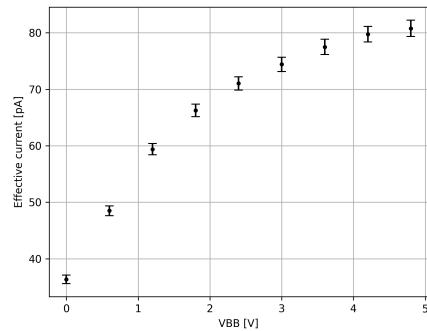
(a) Pulsing  $I_{reset,set}$  dependence



(b) Bias Voltage  $V_{BB}$  dependence



(c) Reset Voltage  $V_{reset}$  dependence



(d) Pulsing Bias Voltage  $V_H$  dependence

Figure 4.8: Dependence of sensor parameters on determined effective current for a  $10^{15}$   $1 \text{ MeV } n_{eq} \text{ cm}^{-2}$  irradiated sensor.

## 4.7 $^{55}\text{Fe}$ source measurements

To determine the effective reset current, it is essential to know the sensor capacitance. However, the capacitance is only approximately known from the design

value, as it can vary from sensor to sensor due to process uncertainties. Hence, it has to be measured, which can be done with a radioactive source. Here, an  $^{55}\text{Fe}$  source is utilized.

The measurement procedure involves repeating the gain calibration steps outlined in section 4.2. Instead of relying on an internal charge injection, which is utilized in pulsing measurements, the external charge generated by the x-rays from the  $^{55}\text{Fe}$  source is used to accumulate charge and extract signals.

$^{55}\text{Fe}$  decays into  $^{55}\text{Mn}$ , which in turn emits two characteristic X-rays with energies of 5.9 keV ( $K_\alpha$ ) and 6.5 keV ( $K_\beta$ ). These X-rays are known to produce, on average, 1640 and 1800 electron-hole pairs in silicon, respectively [37]. With this information, it is possible to locate the corresponding peaks in the measured spectrum. The recorded energy spectra for chips with different pixel pitches are shown in figure 4.9. The amplitude of a signal corresponds to the accumulated charge. Hence, the peaks in the spectrum can be correlated with the amount of charge expected to be liberated by the impact of the X-rays. Consequently, this correlation enables the determination of the sensor capacitance via

$$C = \frac{Q}{V}, \quad (4.1)$$

where  $C$  is the sensor capacitance,  $Q$  is the charge released by the X-rays and  $V$  is the voltage amplitude at the peak. The sensor capacitance is comparable for all pixel variants, with values ranging from 2 to 3 fF.

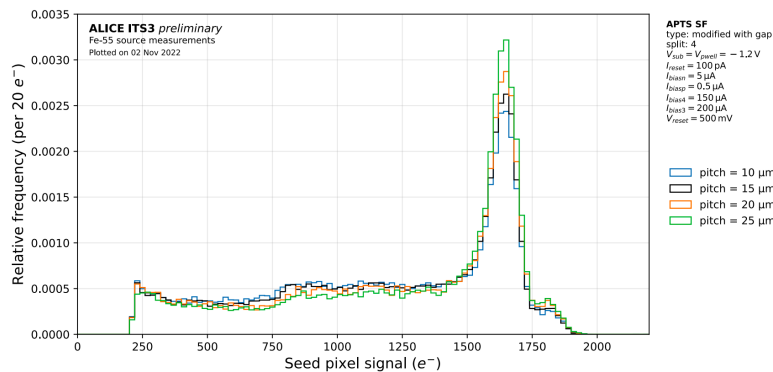


Figure 4.9: Energy spectrum of the accumulated charge in the seed pixel during  $^{55}\text{Fe}$  source measurements in the APTS with source follower. The spectra for various pixel pitches are illustrated, all APTS are produced with the modified process [38].

# Chapter 5

## Leakage Current Analysis

The following chapter discusses the analysis of signal shapes of APTS sensors to determine the leakage current. Evaluating the leakage current across various sensors under different environmental conditions serves as a valuable tool for quantitatively assessing sensor performance, particularly for irradiated sensors, as elaborated in section 2.4.1. It is important to note that conventional and simple I-V measurements have not been effective in measuring the leakage current due to the dominance of other currents in the circuit. As a result, the methodology presented in this chapter essentially represents the only viable approach for measuring the leakage current in these sensors so far.

### 5.1 Preliminary considerations to the reset current

The first step to determine the leakage current is to characterize the signal shape. The fragments of the APTS circuit responsible for the signal shape (compare Section 3.2.2) are shown schematically in figure 5.1. For simplicity reasons, the sketch omits the amplifying source follower stages. Using the schematic, the characterization of the signal shape can be effectively achieved through the analysis of the drain current, which is done in the following section.

The APTS reset transistor operates in the subthreshold region (refer to section 2.3), as the operating condition in that regime fits the low power consumption requirements of the APTS towards the ITS3 (see section 1.4). In this region, the drain current  $I_D$  of the transistor displays an exponential dependence on the gate-to-source voltage  $V_{GS}$ , the threshold voltage  $V_T$ , and the drain-to-source voltage  $V_{DS}$ , following equation 2.15. This behavior is a consequence of how charge carriers move in the transistor under different biasing conditions, as detailed in section 2.3. To simplify the drain current equation, a reset current  $I_{reset}$  can be introduced, as indicated by the bias of the transistor in figure 5.1. Thereby, the impact of the gate

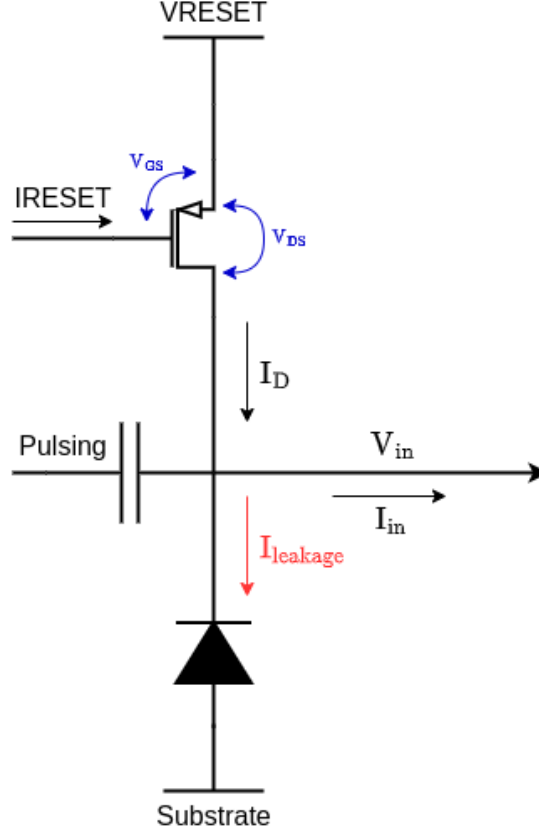


Figure 5.1: Schematic of APTS source follower. It includes the version reset transistor and accounts for the leakage current.

voltage  $V_{GS}$  is minimal, considering that both  $V_{reset}$  and  $I_{reset}$  are biased with a constant supply during operation.

The fluctuations in the gate-to-source voltage  $V_{GS}$  due to the power supply are in the order of 0.05%, and the threshold voltage  $V_T$  remains nearly constant, changing only by about  $-1.6 \text{ mV} \cdot \text{C}^{-1}$  while being in the order of 500 mV in most applications [18, 40]. Additionally, due to the water cooling setup, the temperature can be constant with minimal fluctuations, expected to be around  $\Delta T = 0.5 \text{ }^\circ\text{C}$  [39]. As a result,  $V_{GS} - V_T$  and the corresponding term in the equation can be treated as constants, allowing for the simplification  $I_{reset} = I_0 \cdot \exp\left(\frac{V_{GS} - V_T}{V_{th}}\right)$ . It is essential to understand that, in this simplified form,  $I_{reset}$  is treated as a constant, but some fluctuation is expected due to the exponential dependency on  $V_{GS}$  and  $V_T$ , which will be further discussed in section 5.3. The following equation for the drain current

$$I_D = I_{reset} \cdot \left(1 - \exp\left(\frac{-V_{DS}}{V_{th}}\right)\right) \quad (5.1)$$

is derived from equation 2.15 and reveals that the drain current,  $I_D$ , is primarily influenced by  $I_{reset}$ , the drain-source voltage ( $V_{DS}$ ), and the temperature. From the

intrinsic nature of equation 5.1, it becomes apparent that  $I_D$  reaches a value of zero only when  $V_{DS}$  or  $I_{reset}$  converges to zero. Additionally, it is worth noting that  $V_{DS}$ , the voltage across the drain and source terminals of the transistor, is primarily influenced by charge injection via the pulsing capacitance or charge accumulation through the collection electrode. As the source voltage of the transistor ( $V_{reset}$ ) is held constant, the variation in  $V_{DS}$  is closely correlated to the observable voltage signal,  $V_{in}$  (as depicted in figure 5.1). Therefore, it is reasonable to make the approximation that the observed voltage signal is given by  $V_{in} = -V_{DS}$ . This assumption holds true when the drain current is small and the source voltage  $V_{reset}$  remains constant, ensuring that the voltage drop across the source terminal is negligible.

Ideally, the reset current  $I_{reset}$  should be identical to the externally set reset current parameter,  $I_{reset,set}$ . However, in practice, factors such as manufacturing variations influence the reset current, causing deviations even on a pixel-to-pixel basis. These factors include channel length and width variations, as visible in equation 2.13. As a consequence, the actual  $I_{reset}$  can be expressed as a function of the set current  $I_{reset,set}$  via a proportionality factor  $m$  in the following way:

$$I_{reset} = m \cdot I_{reset,set} . \quad (5.2)$$

## 5.2 The effective reset current

The next step is to introduce the leakage current into the drain current equation. For an ideal and non-irradiated sensor, neglecting the leakage current, the drain current  $I_D$  is the dominant current flowing between the collection electrode and the reset transistor; hence it can be described as  $I_{in} = I_D$ . Instead of considering the input current  $I_{in}$  as the current flowing to the drain, it represents the current associated with a change in the voltage across the sensor capacitance. Therefore, the relationship to the observed signal can be expressed as  $dV_{in}(t) = I_{in}(t)/C \cdot dt$ , where  $C$  represents the sensor capacitance, and  $dt$  the time interval. This indicates that no input current is apparent if no signal is introduced into the circuit.

For an irradiated sensor, the leakage current has to be introduced, as elaborated in section 2.4.1. Figure 5.1 illustrates the leakage current with respect to the collection electrode and the reset transistor. This leakage current counteracts the resetting behavior of the drain current with respect to the input current  $I_{in}$ , effectively limiting the input current to:

$$I_{in} = I_D - I_{leakage} . \quad (5.3)$$

Regardless of the irradiation of the sensor, the input current must be zero in the absence of a signal, as otherwise a signal voltage would be induced. This implies that, in the irradiated case, the drain current has to compensate for the leakage current. As  $I_{reset}$  is assumed to be constant, the exponential component has to be modified to counterbalance the leakage:

$$I_D = I_{reset} \cdot \left( 1 - c \cdot \exp \left( \frac{V_{in}}{V_{th}} \right) \right) \quad (5.4)$$

To determine the factor  $c$ , we can resolve equation 5.3 with the condition that  $I_{in} = 0$  if no signal is introduced (hence  $V_{in} = 0$ ):

$$I_{in} = I_{reset} \cdot \left( 1 - c \cdot \exp \left( \frac{V_{in}}{V_{th}} \right) \right) - I_{leakage} \quad (5.5)$$

$$0 = I_{reset} \cdot (1 - c) - I_{leakage} \quad (5.6)$$

$$c = \frac{I_{reset} - I_{leakage}}{I_{reset}} \quad (5.7)$$

$$c = 1 - \frac{I_{leakage}}{I_{reset}} \quad (5.8)$$

Including equation 5.4 with the determined  $c$  in equation 5.3, the new  $I_{in}$  results in:

$$I_{in} = I_{reset} \cdot \left( 1 - \left( 1 - \frac{I_{leakage}}{I_{reset}} \right) \cdot \exp \left( \frac{V_{in}}{V_{th}} \right) \right) - I_{leakage} , \quad (5.9)$$

which simplifies to

$$I_{in} = (I_{reset} - I_{leakage}) \cdot \left( 1 - \exp \left( \frac{V_{in}}{V_{th}} \right) \right) \quad (5.10)$$

Notably, this equation is analogous to the initial case of a non-irradiated sensor, with the only difference being that the leakage current decreases the available reset current. Defining an effective reset current of

$$I_{effective} = I_{reset} - I_{leakage} , \quad (5.11)$$

both cases (with and without leakage current) can be described through the following current equation:

$$I_{in} = I_{effective} \cdot \left( 1 - \exp \left( \frac{V_{in}}{V_{th}} \right) \right) \quad (5.12)$$

### 5.3 Reset current determination

We exploit the fact that the voltage produced by a signal  $V_{in}$  is measured, to extract the effective reset current. For that purpose, the relationship between the current from the collection electrode into the pixel circuit,  $dV_{in}(t) = \frac{I_{in}}{C} dt$  is used, where  $C$  denotes the sensor capacitance. The capacitance can be assessed through characterization measurements using a  $^{55}\text{Fe}$  source, as discussed in section 4.7. By solving this differential equation utilizing equation 5.12, we obtain the following function describing the pulse in terms of the effective current (full derivation in appendix A):

$$V_{in}(t) = -V_{th} \cdot \ln \left( \exp \left( \frac{-I_{effective} \cdot (t - t_0)}{V_{th} \cdot C} \right) + 1 \right), \quad (5.13)$$

where  $V_{th}$  represents the thermal voltage and  $t$  is the time corresponding to the current signal voltage  $V_{in}(t)$ . The effective current  $I_{effective}$  and the constant time offset  $t_0$  serve as the variables for the fit function.

Figure 5.2 shows the application of this equation as a model for a pulsing signal of a non-irradiated APTS. Here, in red, the signal pulse from the model is displayed, whereby the fit range was chosen to start two frames after the signal amplitude maximum (see section 4.6 for more details) and end when the signal reaches the vicinity of the baseline, to optimize the fit. Each gray graph represents one of the 1000 pulses, and the blue markers show the arithmetic mean used for the model over all 1000 pulses recorded for this setting (see section 4.3). The error of the mean is calculated for each time frame using the standard deviation of the sample mean:

$$\sigma_{\bar{x}} = \frac{\sqrt{\frac{1}{N-1} \sum_{i=1}^N (x_i - \bar{x})^2}}{\sqrt{N}} \quad (5.14)$$

where  $x_i$  denotes the individual measurements,  $\bar{x}$  represents the sample mean of the signal, and  $N$  indicates the sample size.

Figure 5.2 shows that the set reset current  $I_{reset,set}$  (100 pA in this example) is not equal to the effective current  $I_{effective}$  (76 pA here), which is expected from the discussion in section 5.2.  $I_{effective}$  corresponds to  $I_{reset}$  in this case as no significant leakage current is expected for a non-irradiated sensor.

To assess the goodness of the fit, we consider a reduced  $\chi^2$ , defined as:

$$\chi_{red}^2 = \frac{1}{\nu} \sum \frac{(x_i - y_i)^2}{\sigma_i^2}. \quad (5.15)$$

Here,  $x_i$  are the observed values,  $y_i$  are the expected values from the model,  $\sigma_i$  are the uncertainties in the observed values, and  $\nu$  is the number of degrees of freedom, typically calculated as the number of data points minus the number of fit parameters ( $n_{fitparams} = 2$ ) estimated from the data. The  $\chi_{red}^2$  analysis is a statistical measure utilized to quantify the discrepancy between the observed data and the values expected from the fit model. It is normalized by the relevant degrees of freedom in the fit.

A  $\chi_{red}^2$ -distribution with a mean value close to 1 typically indicates a good fit, suggesting that the discrepancies between the observed data and the predicted values are comparable to the uncertainties in the data. A mean value significantly larger than 1 suggests that the model is not adequately describing the data, which might be due to various reasons such as a too simple model, neglected systematic errors, or the uncertainties in the data being underestimated. Conversely, a  $\chi_{red}^2$ -distribution with a mean value substantially smaller than 1 may indicate that the uncertainties in the data have been overestimated or that the model is too flexible and is effectively “over-fitting” the data.

In the fit shown in figure 5.2 (left), the  $\chi_{red}^2$  value of around 70 indicates that the fitting model does not perfectly align with the data. Furthermore, figure 5.2 (right) displays the distribution of  $\chi_{red}^2$  values for all fits from measurements conducted on a single sensor (as outlined in Section 4.3), it is evident that the majority of the data trends toward high  $\chi_{red}^2$  values. Notably, there is a peak at a  $\chi_{red}^2$  value of around 20, while the distribution has a long tail reaching  $\chi_{red}^2$  values of 200. Looking at the current equation used for the model (equation 5.11) and the one introduced in section 2.3.1 (equation 2.15), it is clear that an exponential dependence on  $V_{GS}$  was neglected for the fit model and instead assumed to be constant. Hence, deviations to the data are expected, resulting in the high  $\chi_{red}^2$  value.

Using the detailed theory of the resetting behavior from section 2.3.1, the deviation from the model could potentially be minimized at the price of a more complex derivation of the fit function and result in a time- and  $V_{GS}$ -dependent effective reset current  $I_{effective}$ . As the main interest of this study was to achieve a reasonable estimate of the effective reset current in order to determine the leakage current in the next step, the simplified was chosen to be used nevertheless. This model, while not perfect, provides sufficient information for the purpose of this study. There are other contributing factors, smaller in magnitude, such as the subthreshold leakage current that have not been accounted for in this section but will be in later steps of the analysis.

To confirm that the simplified model results in a reasonable estimate of  $I_{effective}$ , the  $\chi_{red}^2$ -distribution and residuals of fits in different ranges of  $I_{reset,set}$  are investigated.

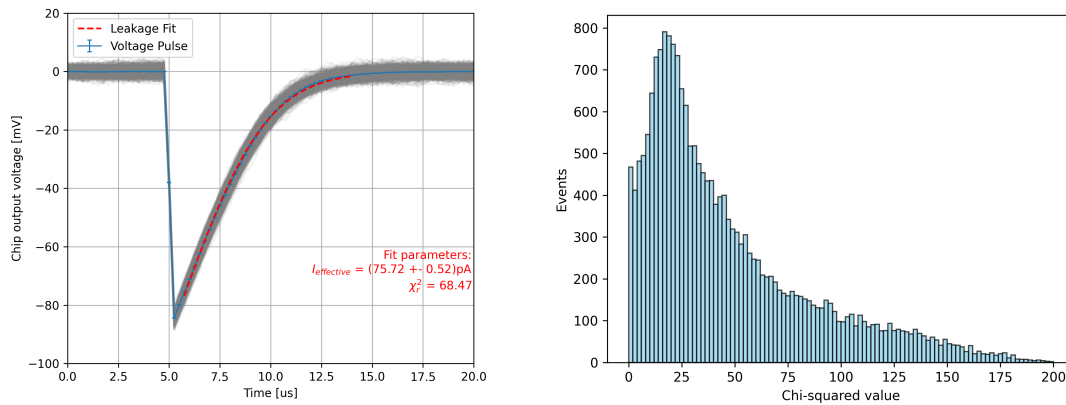


Figure 5.2: **Left:** Signal pulses from a non-irradiated sensor used to determine  $I_{effective}$  for a parameter setting of  $I_{reset,set} = 100 \text{ pA}$ . One thousand individual pulses are depicted in grey, while the blue line represents the average pulse signal. The red line indicates the function fit to the data (refer to text for further explanations).

**Right:** Distribution of reduced chi-squared ( $\chi_{red}^2$ ) values for various settings from a non-irradiated sensor.

Figure 5.3 shows the determination of  $I_{effective}$ , for low and high values of  $I_{reset,set}$  of 40 and 200 pA. As expected with different set reset currents (see section 4.4), for  $I_{reset,set} = 40 \text{ pA}$  shows an extended pulse shape, taking a longer time period to reset to baseline. For the high setting of  $I_{reset,set} = 200 \text{ pA}$ , a fast reset to the baseline is visible. This results in varying numbers of data points being fitted at these settings. The  $\chi_{red}^2$  is lower for  $I_{reset,set} = 200 \text{ pA}$  compared to  $I_{reset,set} = 40 \text{ pA}$ , implying a better fit of the model to the data in the first case. This can have several reasons. On the one hand, with increasing  $I_{reset,set}$  the neglected effects from the simplified fit model could play a small role. On the other hand, the reduced amount of data points could lead to a better fit quality.

The  $\chi_{red}^2$  value of the latter case with  $I_{reset,set} = 40 \text{ pA}$  is comparable to the value for  $I_{reset,set} = 100$  in this example. This observation contradicts the argument of increasing fit quality with increasing  $I_{reset,set}$ . To investigate this behavior and to get a more quantitative view of the fit quality in the different regimes of  $I_{reset,set}$ , the individual  $\chi_{red}^2$ -distributions for selected  $I_{reset,set}$  values are examined.

Figure 5.4 presents the residuals of a single fit alongside the corresponding  $\chi_{red}^2$ -distributions for all data sets with an  $I_{reset,set}$  value of 40, 100, and 200 pA, respectively. The  $\chi_{red}^2$ -distribution for  $I_{reset,set} = 40 \text{ pA}$  shows a broad range of values from 0 to 175, with a peak around a value of 70. The  $\chi_{red}^2$ -distribution for  $I_{reset,set} = 100 \text{ pA}$  has a similar range of values, with a peak around a value of 75, while being more focused around the peak of the distribution compared to

### 5.3. RESET CURRENT DETERMINATION

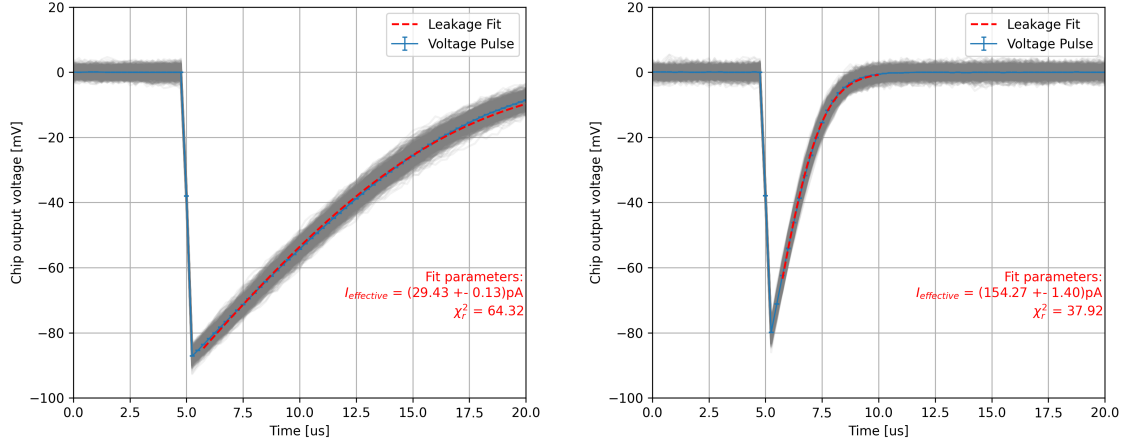


Figure 5.3: Signal pulses from a non-irradiated sensor used to determine  $I_{effective}$  for a parameter setting of  $I_{reset,set} = 40$  pA (left) and  $I_{reset,set} = 200$  pA (right).

the case of  $I_{reset,set} = 40$  pA. The  $\chi_{red}^2$ -distribution for  $I_{reset,set} = 200$  pA is narrow compared to the first two distributions, showing a peak around a value of 20. It is evident that the fit quality improves at very high  $I_{reset,set}$  values. For low and intermediate  $I_{reset,set}$  values 40 and 100 pA, no significant improvement of the fit quality is observable. This observed pattern indicates that the fit model is more suited to high values of  $I_{reset,set}$  while its quality is relatively stable in the lower to moderate range.

In addition to the  $\chi_{red}^2$ -distribution, also the residuals at each regime of  $I_{reset,set}$  can be investigated. In all ranges, a similar residual shape is visible, having an oscillating behavior. As these deviations seem to be systematic, this is another clear indicator of the imperfect fitting model used. For high enough  $I_{reset,set}$ , where the entire signal up to the baseline can be modeled, one can acknowledge that the model is approaching the data as the signal amplitude decreases close to the baseline. Furthermore, examining the residuals for  $I_{reset,set} = 200$  pA, smaller deviations to the data are prominent, and the residuals approach zero more rapidly, compared to the cases with lower  $I_{reset,set}$ .

For all selected  $I_{reset,set}$  values, the residuals are within the range of about 1 mV to the data. Comparing this deviation to the signal amplitude of over 80 mV, the deviation of around 1 mV is comparably small, in the order of on percent. Due to that, it is clear that the simplifications of the model are affecting the fit quality, leading to the deviations in the residuals and high values of  $\chi_{red}^2$ . Nevertheless, for the purpose of determining  $I_{effective}$  with reasonable precision, the simplified approach is sufficient.

However, high  $\chi_{red}^2$ , as seen here, can point to an underestimation of the error. Hence, it is not reasonable to use the error determined from the model as a

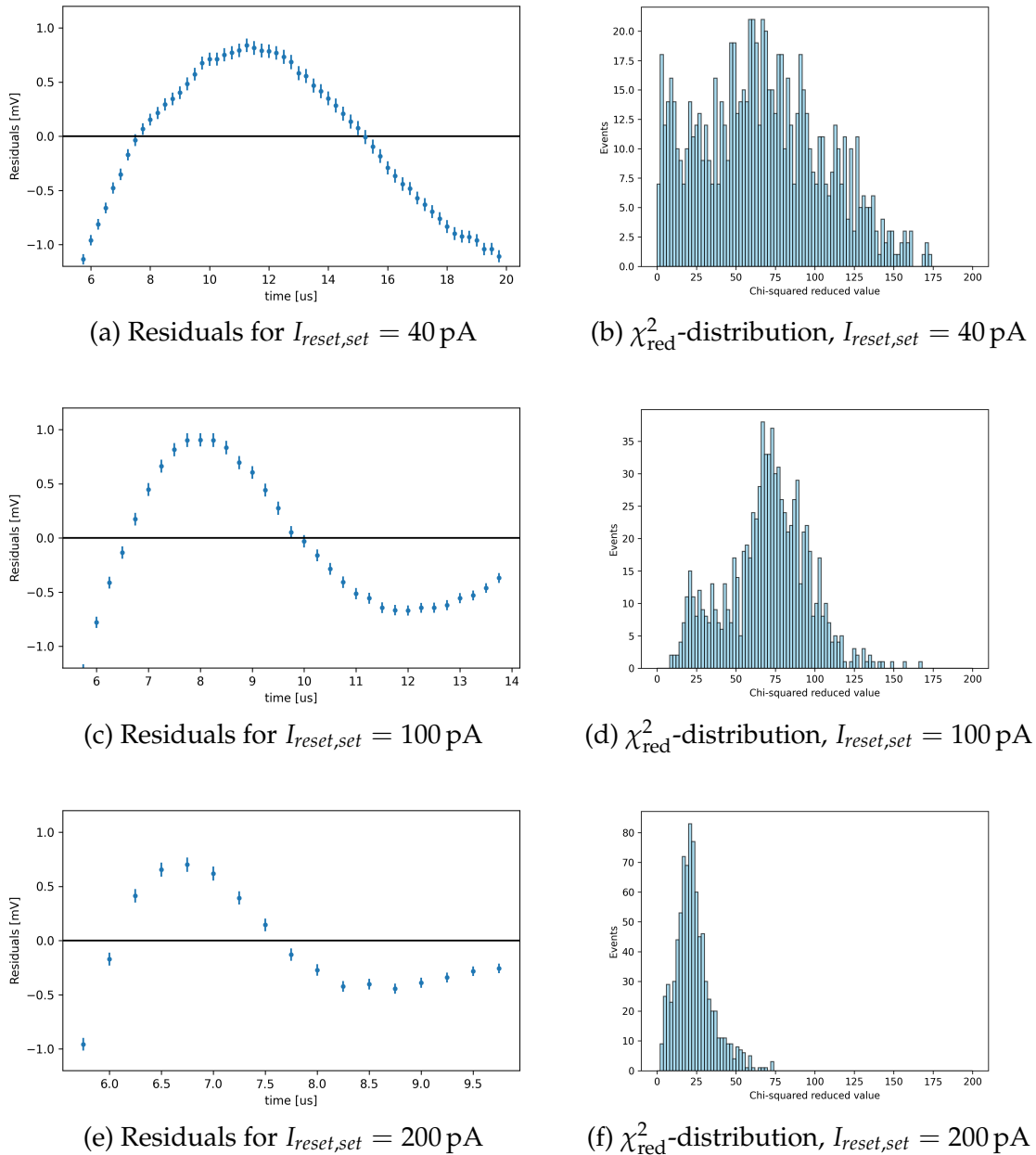


Figure 5.4: Residuals and  $\chi_{red}^2$ -distributions for pulsing measurements at different parameter settings of  $I_{reset,set}$

dominant error on the fit parameter  $I_{effective}$ , but instead introduce systematic sources of error.

Operating the reset transistor in the subthreshold regime means that the current through the reset transistor is highly sensitive to the voltages applied to it ( $V_{GS}$  and  $V_{DS}$ ) and the temperature. As detailed in section 5.1, this sensitivity is due to the exponential relationship of the reset current in this operating regime. Using the definition of the reset current and the uncertainties in terms of temperature and biasing conditions outlined in section 5.1, the systematic uncertainty of the reset current is computed as:

$$\Delta I_{reset} = I_{reset} \cdot \left( \frac{V_T - V_{GS}}{nk_B T/q} \right) \sqrt{\left( \frac{\Delta V_{GS}}{V_{GS}} \right)^2 + \left( \frac{\Delta V_T}{V_T} \right)^2 + \left( \frac{\Delta T}{T} \right)^2} . \quad (5.16)$$

Given the relative uncertainties of  $\frac{\Delta V_{GS}}{V_{GS}} \approx 0.05\%$ ,  $\frac{\Delta V_T}{V_T} \approx 0.16\%$ ,  $\frac{\Delta T}{T} \approx 0.16\%$ , and assuming typical values of 0.5 V for  $V_T$  and 0.3 V for  $V_{GS}$  [18], the relative uncertainty of the reset current approximates to  $\frac{\Delta I_{reset}}{I_{reset}} \approx 1.6\%$ . It has to be noted that this error is just an estimate that assumes typical values for  $V_{GS}$  and  $V_T$ , as the actual values are either unknown or unavailable.

Up until now, transistor effects elaborated in section 2.3.1, like the subthreshold leakage current, are not considered in the uncertainties of the reset current. These effects are less dominant as they scale with the transistor size. At a temperature of 25 °C the leakage is in the order of 1 pA/μm [18]. However, it is essential to incorporate this effect, as the effect is gaining more importance with increasing temperature, reaching up to 30 pA/μm at 75 °C, due to an exponential dependence to the changing  $V_T$ . For the APTS with a sub-100 nm transistor size and measurements conducted up to 40 °C, the subthreshold leakage current is unlikely to exceed one pA, not considering the irradiation damage-induced leakage current. This leads to a slightly increased uncertainties estimation, especially important at low reset currents and higher temperatures:

$$\Delta I_{reset,sys} = \sqrt{(I_{reset} \cdot 1.6\%)^2 + (I_{subthr,leak})^2} \quad (5.17)$$

In total, these effects lead to a systematic uncertainty in the order of 0.5 pA to 3 pA. The total error for the effective current used in the following analysis is  $\Delta I_{reset,total} = \sqrt{(\Delta I_{reset,sys})^2 + (\Delta I_{reset,stat})^2}$ .

Additionally, it is worth mentioning that the error of the leakage current induced by irradiation damage cannot be considered for effective current beforehand since the leakage current is unknown at this point. This error will be discussed in the upcoming section, implying that for the effective reset current, the error  $\Delta I_{effective} \approx \Delta I_{reset,total}$  is applied.

Considering that, in irradiated sensors, leakage current reduces the effective current. An  $I_{reset,set}$  value like 40 pA, which might be suitable for non-irradiated sensors, could be too low for irradiated ones. Nevertheless,  $I_{effective}$  serves as a robust metric for comparing non-irradiated and irradiated sensors as it takes the leakage current into account. By analyzing  $I_{effective}$ , one can produce more meaningful and consistent comparisons between sensors under different conditions, including the performance under irradiation, as investigated in chapter 6. Further

analysis of the relationship of  $I_{effective}$  and  $I_{reset,set}$  will follow in the subsequent section 5.4.

## 5.4 Leakage current determination

In the case of an irradiated sensor, the effective current is a combination of the unknown reset current and the leakage current, as indicated in equation 5.11. Hence, the leakage current can not be directly deduced by the determined effective current of one measurement alone.

In order to estimate the leakage current, an assumption is made that the leakage current for one sensor remains constant as  $I_{reset,set}$  varies, while other parameters stay constant, as it is likely a result of irradiation damage (see section 2.4.1) and not affected by the circuitry. By identifying the linear relationship between the effective current and the reset current, the leakage current can be accurately determined. Equation 5.18 illustrates this behavior, which has to be adjusted by introducing  $I_{reset,set}$ , replacing  $I_{reset}$  using the relation in equation 5.2:

$$I_{effective} = m \cdot I_{reset,set} - I_{leakage} \quad (5.18)$$

To identify the relationship, a series of measurements with varying reset current parameters were performed, while all other parameters were kept constant, as described in section 4.3. Figure 4.6a illustrates the significant pulse-shape dependence of the  $I_{reset,set}$  parameter. The figures 5.5a and 5.5b show the relation of  $I_{effective}$  to  $I_{reset,set}$  for a non-irradiated and an irradiated sensor ( $10^{15}$  1 MeV  $n_{eq}cm^{-2}$ ), respectively.

For both sensors, the expected linear relation between  $I_{reset,set}$  and  $I_{effective}$  is apparent for nearly the entire  $I_{reset,set}$  range and for all temperatures. This behavior is a good indicator for the relation of  $I_{reset,set}$  and  $I_{effective}$  being as expected from equation 5.18.

However, deviations from linearity are observed for very low  $I_{effective}$ , which could be attributed to the effective reset current being insufficient for properly resetting the sensor, causing it to lose its working point and not return to the baseline as intended. Figure 5.6 shows a non-irradiated and an irradiated sensor at low effective currents. It is clear that in both cases, the typical exponential behavior seen in the previous fits is not present. Instead, the reset is very slow and nearly constant, especially for the non-irradiated sensor (left). In the case of the irradiated sensor (right), an unexpected exponential behavior is observed in the first few microseconds after signal injection, which is not predicted by the literature, as discussed in section 4.6.

## 5.4. LEAKAGE CURRENT DETERMINATION

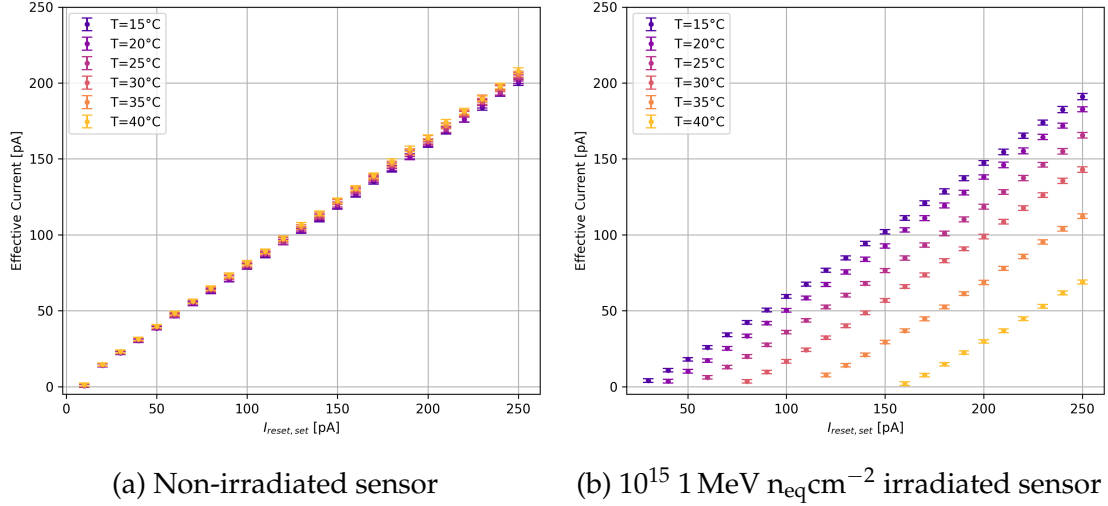


Figure 5.5: Determined effective current as a function of set  $I_{reset}$  of the respective measurement at different temperatures for an irradiated sensor and a non-irradiated sensor. For both sensors, only one representative pixel was chosen.

Looking at figure 5.5b, one can see the most prominent difference between the non-irradiated and the irradiated case being that the effective current is smaller at the same temperature and the same  $I_{reset, set}$  for the irradiated sensor. Furthermore, the effective current is significantly decreasing at higher temperatures but the same  $I_{reset, set}$ -settings. This is a clear indicator that the leakage current increases with temperature (see equation 2.17), which results in a decrease of the effective current as it can be comprehended from equation 5.18. This is the main difference between the irradiated and non-irradiated cases, as the slope of the linear dependence stays constant for the respective temperatures. This is a good indicator that the only difference between those sensors is the appearance of irradiation damage-induced leakage current in the irradiated sensor.

Another aspect, worth mentioning is that even though the determined effective current in the non-irradiated case is nearly constant, a slight trend towards a higher effective current with increasing temperature is visible, even though only in the order of a few pA. This is not expected from our simplified model but can be attributed to the influence of temperature on the reset current (see section 5.1,  $I_{reset} = I_0 \cdot \exp\left(\frac{V_{GS} - V_T}{V_{th}}\right)$ , where  $V_{GS} < V_T$ ). An increasing temperature is indeed causing an increase of a few percent.

For the fit, equation 5.18 is used with  $m$  and  $I_{leakage}$  as fit parameters. Figure 5.7 shows the performed fits on the previously shown data. The linear dependence is well represented, ensuring a reasonable quality of the fit by applying criteria  $\chi_{red}^2 \leq 5$  and  $I_{eff} \geq 30$ . An effect that needs to be considered for the leakage fit of the irradiated sensor is the decreasing amount of data points for higher leakage currents. This reduction is due to the decrease in the effective reset current with

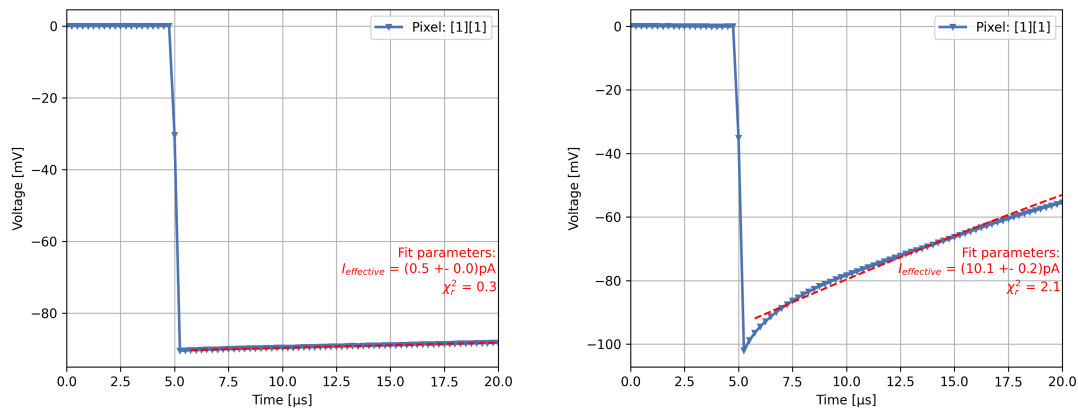


Figure 5.6: Pulsing performance at very low effective reset currents, for a non-irradiated (left) at  $I_{reset,set} = 10$  pA and an irradiated  $I_{reset,set} = 50$  pA (right) sensor. For both sensors, only one representative pixel was chosen.

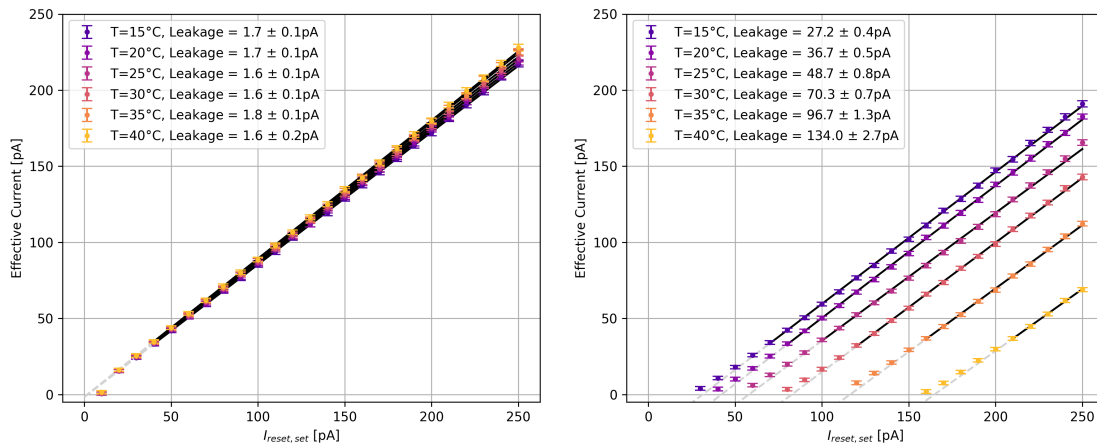


Figure 5.7: Determined effective current as a function of set  $I_{reset}$  of the respective measurement at different temperatures for an  $10^{15}$  irradiated sensor and a non-irradiated sensor. For both sensors, only one representative pixel was chosen. Black lines indicate the linear fits for the leakage current determination.

increasing leakage at constant  $I_{reset,set}$ , which consequently reduces the operating range in terms of  $I_{reset,set}$ . Due to that, a minimum of 5 data points is required to proceed with a fit and ensure its reliability.

Examining the non-irradiated sensor first, it's observed that the leakage is almost non-existent, and the uncertainty in fitting is exceedingly low. A significant offset from zero is apparent, which can be partly explained by temperature effects and the subthreshold leakage, as discussed in the previous section. While this phenomenon contributes to a slight offset, it cannot explain the entire deviation of 2 pA. The unknown exact operating conditions ( $V_T$  and  $V_{GS}$ ) add to the uncertainty, as well as the impact of the imperfect fitting model for the effective reset current.

Turning to the irradiated sensor, the fit appears successful and describes the data comparably to the non-irradiated case. However, there is a clear deviation from the linear behavior in the low effective current regime. This validates the decision to limit the fitting to a minimum of an effective current of 30 pA. Notably, the leakage current nearly doubles for every 10 °C increase in temperature, which is close to the expectations (see equation 5.18). However, the fit uncertainty of the fit parameter becomes more pronounced due to the reduced amount of data points, especially with increasing temperature.

The goodness of the fits is evaluated through the plots in figure 5.8. For the non-irradiated sensor, the  $\chi_{\text{red}}^2$  value is peaking around 1 with a small tail towards higher values, indicating a good fit quality. The fit quality for the irradiated sensor is slightly compromised, mainly due to the reduced number of data points and lower effective current. Nevertheless, with a  $\chi_{\text{red}}^2$  value peaking around 2, the fit can still be considered reliable.

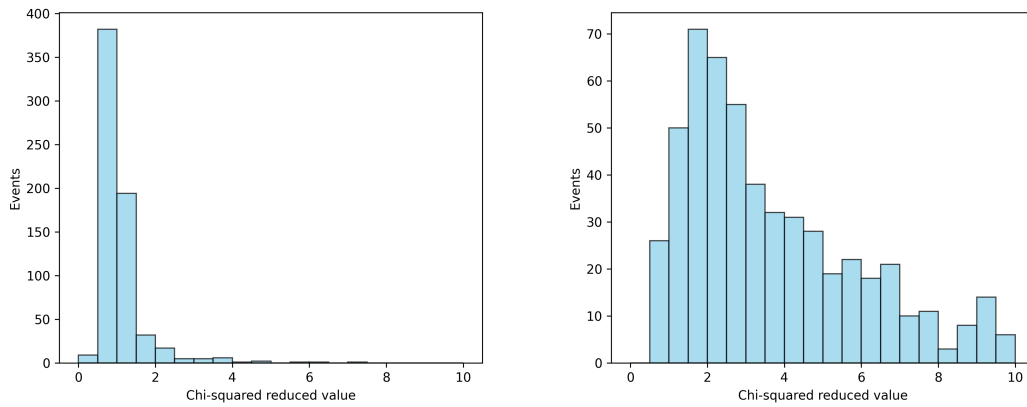


Figure 5.8:  $\chi_{\text{red}}^2$ -distributions for the linear fit of a non-irradiated (left) and irradiated (right) sensor

To estimate the error of the determined leakage current, the equation for leakage current caused by irradiation damage (equation 2.17) is revisited. There, temperature is the only parameter with a significant error. Hence, an equation for the error in leakage current is derived as follows:

$$\frac{\Delta I_{\text{leakage}}}{I_{\text{leakage}}} = \left(2 + \frac{E_g}{2k_B T}\right) \frac{\Delta T}{T} . \quad (5.19)$$

With the previously used error estimate for the temperature of 0.5 °C, the error results in approximately 4%.

In summary, the behavior of sensors under non-irradiated and irradiated conditions is analyzed, with a particular focus on determining the leakage current. The non-irradiated sensor exhibits negligible leakage current with very low fit

uncertainty. However, there is a not fully explained offset from zero, which is partially attributed to the subthreshold leakage and the imperfection of the fitting model for the effective reset current. For the irradiated sensor, which was subject to an exceedingly high irradiation dose of  $10^{15}$  1 MeV  $n_{eq}cm^{-2}$ , more significant deviation, compared to the non-irradiated sensor, from the linear model have been observed, especially at low  $I_{effective}$ . For the data sets investigated in this chapter, the leakage current is measured to almost double with every  $10^{\circ}C$  rise in temperature, which is in good agreement with the expected increase, elaborated in section 2.4.1. Notably, the ability to operate the sensor and measure the leakage current of the highly irradiated sensor is a considerable achievement, as this irradiation level significantly exceeds the requirements for the ITS3 (refer to section 1.4). A more in-depth analysis of leakage currents at different irradiation levels for the entire pixel matrix will be covered in the subsequent chapter.

# Chapter 6

## Performance of irradiated and non-irradiated APTS sensors

For the assessment of the APT sensor performance, data obtained from the measurements applying different biasing and environmental parameter combinations are analyzed, for different prototype versions of the technology. In this section, the focus is on results obtained with prototypes with a pixel pitch of 15  $\mu\text{m}$  and the modified process with gap on the wafer 22, namely the AF15P\_W22 sensors. This particular prototype was selected for the main part of the analysis because it implements the most significant advancements in the new detector technology. With the larger depletion region and improved signal-to-noise ratio and higher charge collection efficiency in the pixel edges (see section 3.1), it is expected to have significantly improved performance under irradiation, which is worth to be investigated.

### 6.1 Signal analysis as a function of the operating temperature and radiation dose

The first step to evaluate the performance of the sensors is to study the change of the pulse shape at different temperatures. This provides the most quantitative insight into the sensor behavior by utilizing the full information available from the analog readout. Investigating two AF15P\_W22 sensors at the standard parameter settings (refer to section 4.4), the signal dependence on the temperature is illustrated for a neutron irradiated sensor (solid line, triangle markers) ( $10^{15}$  1 MeV  $n_{\text{eq}}\text{cm}^{-2}$ ) and non-irradiated (dashed line, circular markers) sensor in figure 6.1. It is apparent that the non-irradiated sensor shows a small effect on the temperature, compared to the irradiated sensor. The latter it can be seen that the recovery time of the output voltage back to the baseline is extended with rising temperatures. This

behavior indicates an effective change of the resetting current  $I_{reset}$ , even though it is kept constant by the corresponding biasing parameter  $I_{reset,set}$ . A possible explanation can be provided by considering the increase of the leakage current in the pixel (refer to section 5.1).

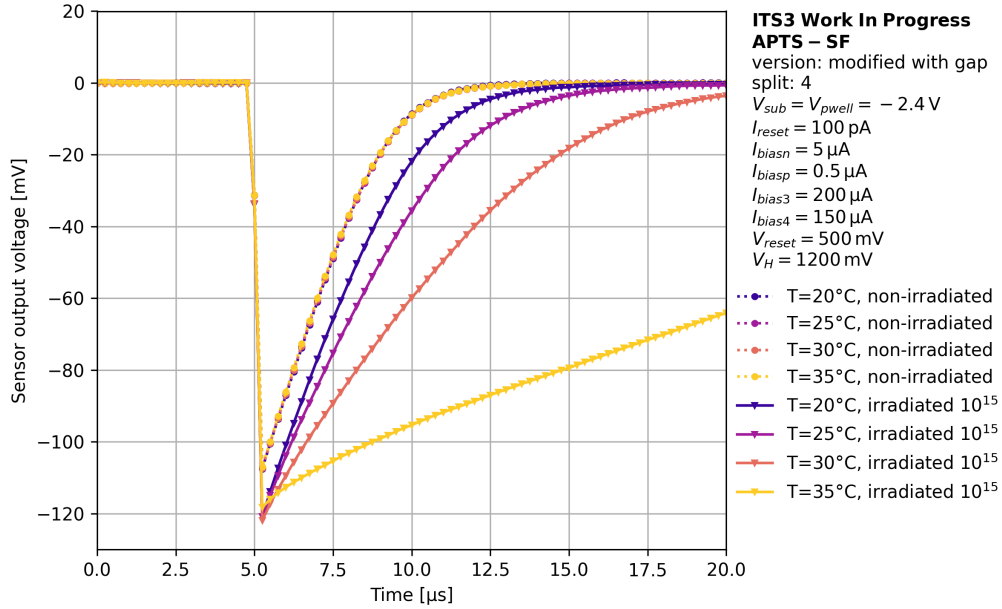


Figure 6.1: Temperature dependence of the pulse shape for an irradiated (solid line, triangles)  $10^{15}$   $1 \text{ MeV n}_{eq}\text{cm}^{-2}$  and non-irradiated (dashed line, circles) sensor. Only four representative temperatures out of the tested temperature range are selected. For both sensors, only one representative pixel was chosen.

After having examined the general temperature dependence of the two mentioned sensors, the investigation is extended to include data from all available irradiation levels over the full temperature range from  $15^\circ\text{C}$  to  $40^\circ\text{C}$  (refer to section 4.3). Figure 6.2 displays the temperature dependence of the pulse shape for sensors at all irradiation levels at which the sensor is operable at standard parameters, allowing for comparison of the different irradiation levels.

Similarly to the non-irradiated sensor shown in figure 6.1, at the (NIEL) radiation dose of  $10^{13}$   $1 \text{ MeV n}_{eq}\text{cm}^{-2}$ , no significant temperature dependence of the signal is observed. Starting from an irradiation level of  $10^{14}$   $1 \text{ MeV n}_{eq}\text{cm}^{-2}$ , a slightly prolonged recovery time becomes noticeable. The sensors that received a dose of  $10^{15}$   $1 \text{ MeV n}_{eq}\text{cm}^{-2}$  (figure 6.2c) and  $1.5 \cdot 10^{15}$   $1 \text{ MeV n}_{eq}\text{cm}^{-2}$  (figure 6.2d) are not operable, i.e., no stable working point can be found anymore, at temperatures exceeding  $35^\circ\text{C}$  and  $20^\circ\text{C}$ , respectively. Furthermore, sensors with irradiation levels of  $5 \cdot 10^{15}$   $1 \text{ MeV n}_{eq}\text{cm}^{-2}$  and higher are shown not to operate at the standard parameter settings ( $I_{reset} = 100 \text{ pA}$ ,  $V_{BB} = -2.4 \text{ V}$ , see section 3.2.1 for all

## 6.1. SIGNAL ANALYSIS AS A FUNCTION OF THE OPERATING TEMPERATURE AND RADIATION DOSE

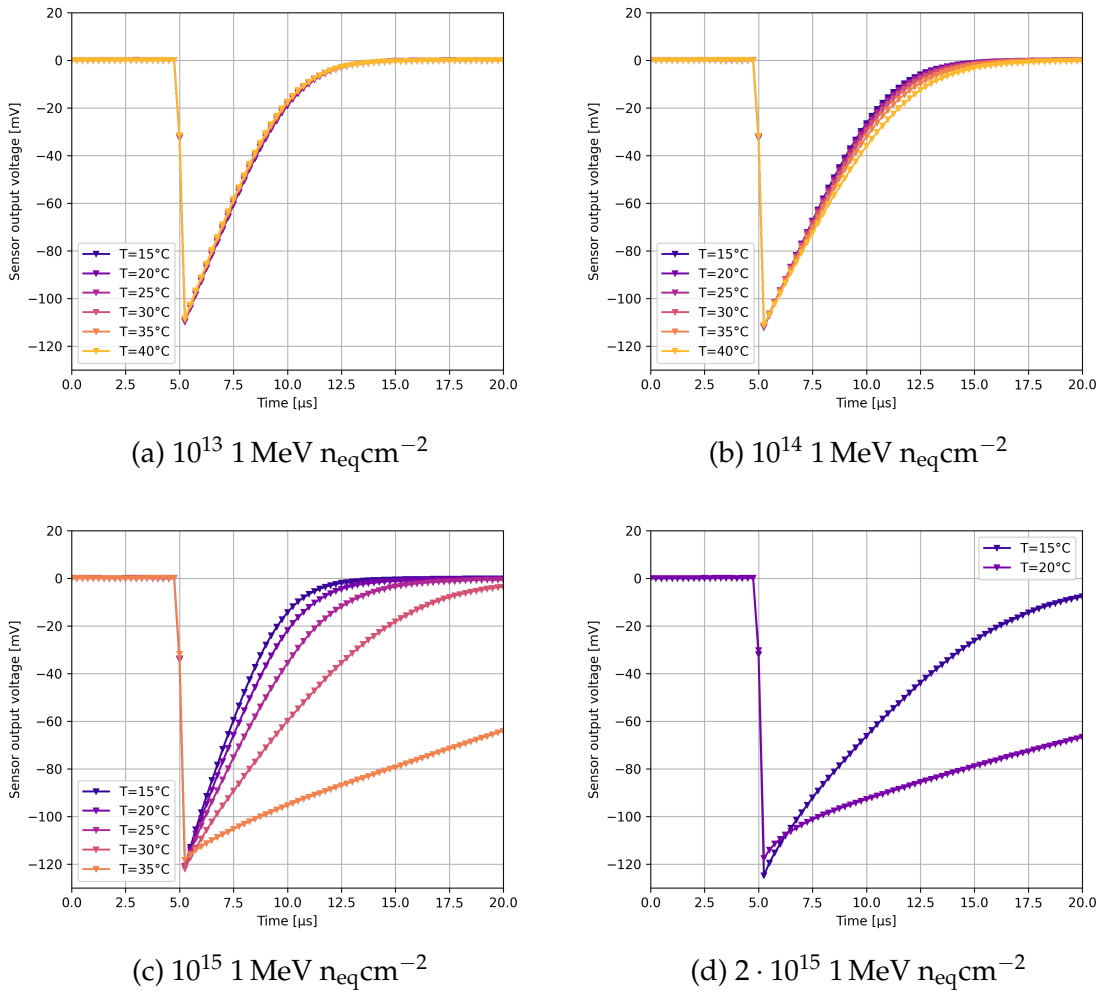


Figure 6.2: Temperature dependence of the pulse shape for functional sensors at the indicated irradiation levels and at standard parameter settings, amongst others  $I_{\text{reset,set}} = 100 \text{ pA}$ . Missing temperatures indicate that the corresponding sensor is not operational at this temperature. For each sensor, only one representative pixel was chosen.

standard biasing settings) at all. For this reason, they are not shown in figure 6.2. As discussed in section 4.4.

In summary, it can be observed that as long as the sensor can operate under these standard conditions, both increased temperature and increased radiation dose contribute to rising leakage current. This impacts the effective reset current  $I_{\text{effective}}$ , slowing down the signal's return to baseline. With  $I_{\text{effective}}$  approaching zero, the sensor cannot operate anymore, as the signal cannot recover to the baseline, hence losing the stable operating point.

Increasing  $I_{\text{reset,set}}$  extends the operational temperature range of irradiated sensors, as it increases  $I_{\text{effective}}$ . Figure 6.3 illustrates the temperature dependence of the

pulse shape for all irradiation levels for the highest possible setting of  $I_{reset,set} = 250$  pA.

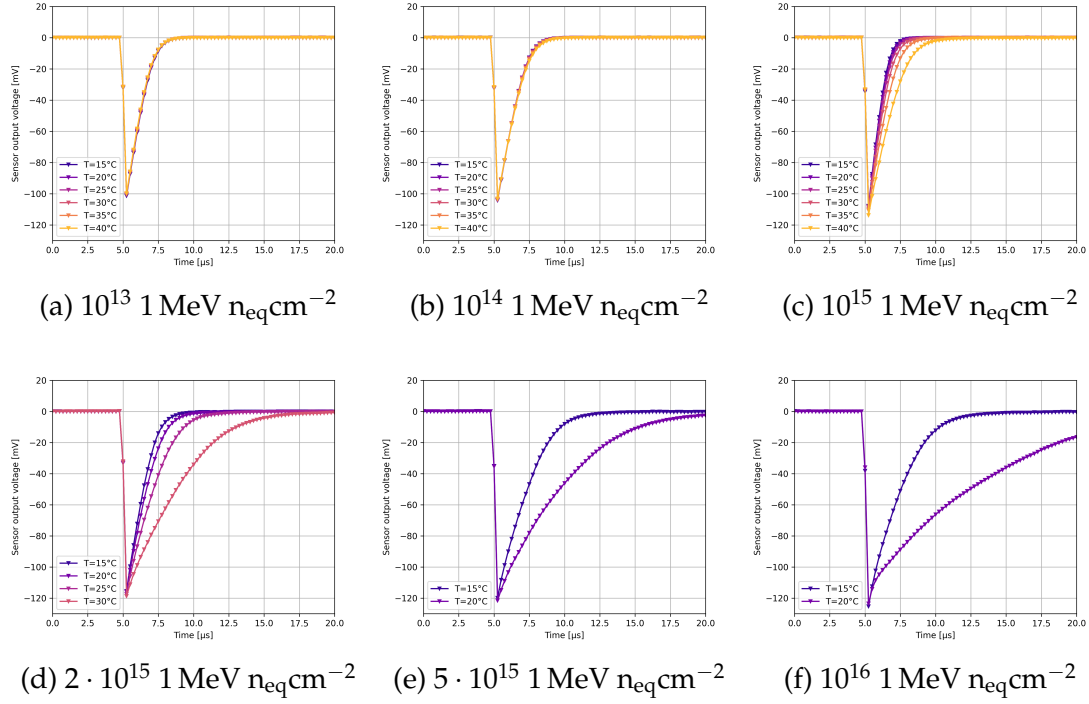


Figure 6.3: Temperature dependence of the pulse shape for increasing irradiation levels from (a) to (f) with optimized parameter setting,  $I_{reset,set} = 250$  pA. Missing temperatures indicate that the corresponding sensor cannot operate at this temperature. For each sensor, only one representative pixel was chosen.

It can be observed that the two sensors with irradiation levels higher than  $5 \cdot 10^{15}$  1 MeV  $n_{eq}cm^{-2}$ , which were not operable at standard parameters could be recovered due to the more practical choice for  $I_{reset,set}$ . Furthermore, the functional temperature range for the sensors shown in figure 6.2 is extended, as observable in 6.3c and 6.3d. The increased  $I_{reset,set}$  value considerably attenuates the effects observed, especially at the irradiation levels of  $10^{14}$  and  $10^{15}$  1 MeV  $n_{eq}cm^{-2}$ , bringing the performance closer to that of the non-irradiated sensor.

It is important to note that even at this increased  $I_{reset,set}$  setting, not all sensors have a stable working point over the entire measured temperature range. Additionally, at irradiation levels higher than  $10^{15}$  1 MeV  $n_{eq}cm^{-2}$ , the effects on the signal shape are still significant. It is anticipated that higher leakage currents, apparent at higher irradiation levels or higher temperatures, would also need higher reset current to fully compensate for the effect on the signal. These observations indicate that there are limitations to the performance of these sensor prototypes for irradiation levels higher than  $10^{15}$  1 MeV  $n_{eq}cm^{-2}$ .

Nevertheless, the achieved performance at already high irradiation levels of the sensors depicted here is a good indicator and an important preliminary result for

the feasibility of this technology towards the ITS3 (requires  $10^{13}$   $1 \text{ MeV } n_{\text{eq}}\text{cm}^{-2}$ ) upgrade and the future ALICE3 (requires  $1.5 \cdot 10^{15}$   $1 \text{ MeV } n_{\text{eq}}\text{cm}^{-2}$  per year) experiment, as discussed in the section 1.4.

## 6.2 Noise investigation

Before analyzing the leakage current, the noise levels for different irradiation levels need to be investigated, as they are the baseline of the measurement and hence influence the precision of the measurement.

The noise is calculated by taking the standard deviation of the baseline and determining the arithmetic mean of the noise over all pixels. Figure 6.4 shows the noise dependence on the temperature for different irradiation levels (right), as well as the dependence of the noise on the reverse bias (left) for a non-irradiated sensor. All measurements are done at  $I_{\text{reset,set}} = 250 \text{ pA}$ , because of performance reasons of the irradiated sensors, which are elaborated in the subsequent sections.

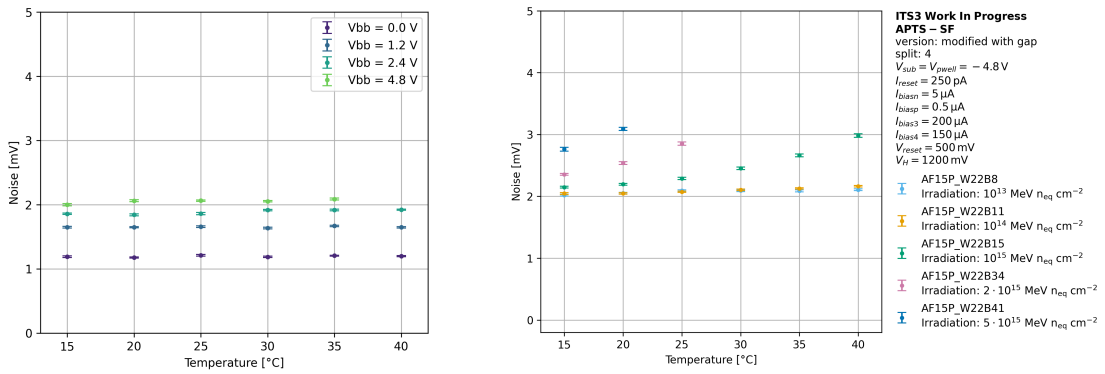


Figure 6.4: Noise level at different temperatures and  $V_{BB}$  for a non-irradiated sensor (left). For different irradiation levels (right), the settings were chosen such that the sensors operate over a wide range of temperatures. The mean over all pixels is shown.

A clear noise dependence on the reverse bias can be seen for the non-irradiated sensor. The increase of the noise level with increasing reverse bias voltage can be attributed to the increased depletion depth and consequently reduced depletion capacitance (see section 2.2). The reduced capacitance leads to an increased signal and consequently to increased noise. A marginal increase with increasing temperature can be observed as well, which is an indicator for increased thermal noise (stemming from thermal excitation of charge carriers) and possibly increased sub-threshold leakage current (refer to section 2.3.1).

The irradiated sensors in figure 6.4 only show the noise-temperature dependence at a reverse bias voltage of  $V_{BB} = -4.8 \text{ V}$ . Hence the comparison with a non-

irradiated sensor from the same figure has to be done at the same reverse bias setting. It can be observed that the noise increases with increasing irradiation levels. For radiation doses of up to  $10^{14}$   $1 \text{ MeV n}_{\text{eq}}\text{cm}^{-2}$ , approximately the same temperature dependence and absolute noise level as for the non-irradiated sensor can be seen. For higher doses, the dependence on temperature is gradually increasing. Furthermore, with increasing irradiation, an increasing temperature dependence is visible, which can be attributed to the increased leakage current (see figures 6.2 and 6.3).

### 6.3 Leakage current determination

After the discussion of the qualitative trends of the signal shape with a focus on stable sensor operation and on the baseline restoration time caused by radiation-induced effects, the next step of the analysis is to quantify the sensor performance. One relevant parameter to investigate in this context is the leakage current, as it is shown to exhibit a dependence on the irradiation level (refer to Section 2.4.1) and is an indicator of the available operating range and radiation hardness. This effect is shown in figure 5.7 from section 5.4. The method introduced in chapter 5 will be applied. The signal pulses examined in section 6.1 are utilized to determine the *effective reset current*  $I_{\text{effective}}$  at the respective parameter settings of the sensor, as outlined in section 5.3. By systematically varying  $I_{\text{reset,set}}$  while maintaining other sensor parameters unchanged, a correlation between the parameter  $I_{\text{reset,set}}$  and the determined  $I_{\text{effective}}$  can be derived. Consequently, the leakage current can be calculated using equation 5.18.

Figure 5.7 provides a visual representation of this method, applied to a sensor exposed to  $10^{15}$   $1 \text{ MeV n}_{\text{eq}}\text{cm}^{-2}$  and to a non-irradiated sensor. The effectiveness of this method has been validated for both scenarios. Nevertheless, it has to be noted once more that for high irradiation levels, the accuracy of the fit for the leakage current decreases. This reduced precision is partly attributed to the decrease in the effective reset current with increasing leakage. Consequently, the operating range in terms of  $I_{\text{reset,set}}$  is reduced. This leads to a smaller set of data points left for the leakage current determination.

The method for determining the leakage current was performed in the previous chapter only on two sensors, evaluating one pixel each. For a more comprehensive and statistically significant assessment of the leakage current, it is crucial to extend the analysis to take into account all pixels of a sensor matrix, a range of temperatures, and various irradiation levels. Additionally, the comparison of different sensors with the same process variants and irradiation levels is valuable. The

latter ensures the reproducibility of the found results and, therefore undoubtedly qualifies the 65 nm technology in this regard.

### 6.3.1 Pixel-to-pixel variation

In this subsection, the pixel-to-pixel variation in terms of the leakage current and the effective reset current is investigated. This investigation is particularly interesting for optimizing sensor calibration and ensuring robust performance, especially when the sensors are subjected to varying temperature and irradiation levels.

Especially the reset current is a quantity that can change significantly due to process uncertainties such as the gate width of the implemented CMOS transistors, as detailed in section 2.3. Figure 6.5 shows the determined effective reset currents in relation to the set  $I_{reset}$  for the entire pixel matrix of a non-irradiated sensor. The expected linear relationship is seen for every pixel, which confirms the analysis done in chapter 5. However, the effective reset current at the same parameter settings is showing a significant spread, which is quantified in figure 6.7 and discussed later in this section. This is expected to be caused by the previously mentioned pixel-to-pixel variations in the sensor fabrication process.

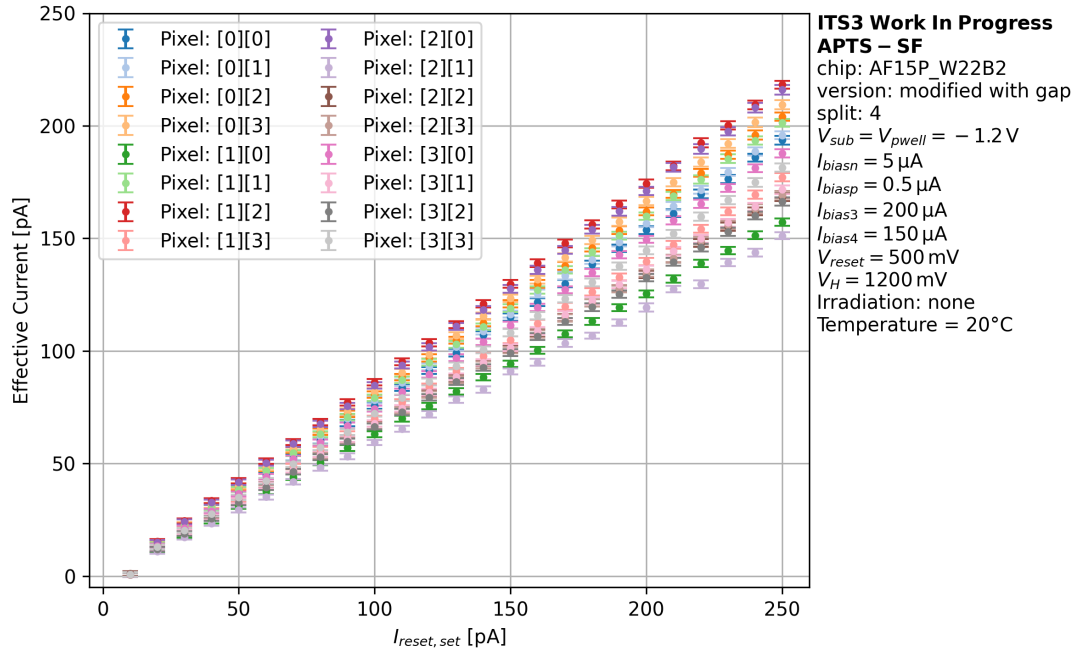


Figure 6.5: Effective current in relation to set reset current for all pixels of a non-irradiated APTS.

In order to quantify the effect of damage introduced by neutron irradiation, figure 6.6 shows an irradiated sensor is investigated in a similar way. Here, the wider

spread of effective current measured for different pixels indicates that damage caused through irradiation has also influenced the circuitry, changing the effective reset current. At this stage, a precise explanation of the findings is not yet possible, because several effects are at play.

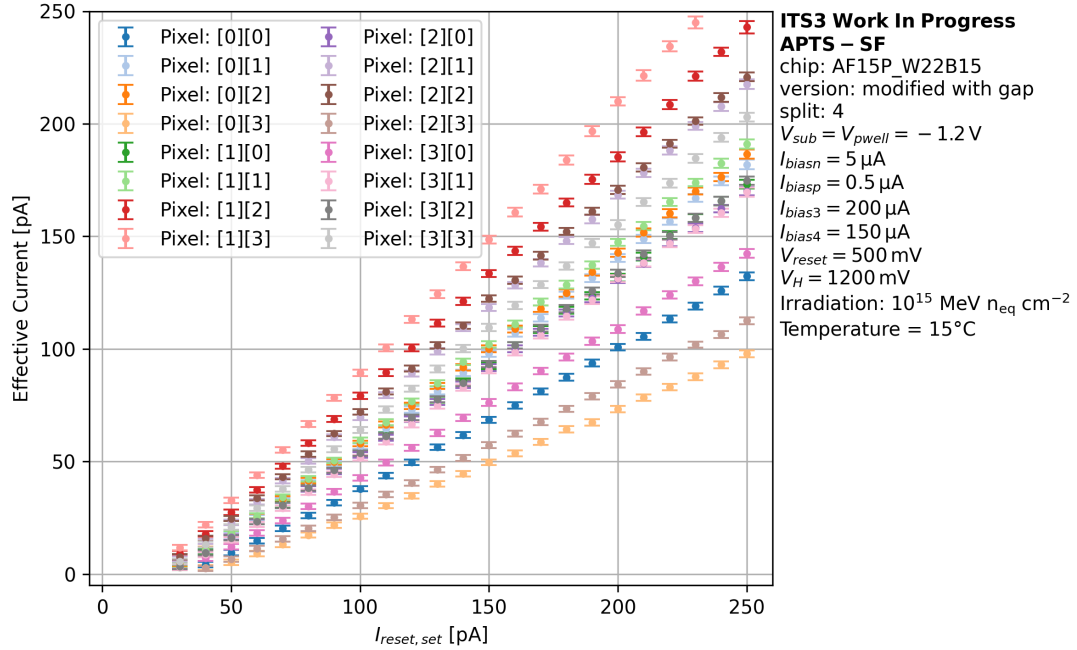


Figure 6.6: Pixel to pixel variation of effective reset current for an irradiated sensor ( $10^{15}$  1 MeV  $n_{eq}cm^{-2}$ ).

It is still left to compare the behavior of those two sensors to a second one for each irradiation level to validate the results. This establishes the comparability of sensors with the same properties and ensures that the results are not an effect measured for one particular sensor. This comparison is shown in figure 6.7, illustrating the spread by the effective reset current at  $I_{effective} = 200$  pA for two non-irradiated and two irradiated sensors ( $10^{15}$  1 MeV  $n_{eq}cm^{-2}$ ) shown in different colors.

It can be seen that the effective current ranges over a wide range for all. Evaluating the Root Mean Square (RMS), indicates that the irradiated sensors tend towards a wider spread in pixels. On the contrary, the average effective reset current over all pixels tends to be lower for irradiated sensors. To validate this observation, more sensors with the same fabrication process and radiation dose need to be tested.

Another aspect that is useful to compare with the irradiated sensors from the figure is the determined average leakage current over all pixels, as done in table 6.1. The leakage current was calculated by a linear fit on the  $I_{effective}-I_{reset,set}$  relation, from which the offset of the effective reset current was determined (see section 5.4). This was done for the two irradiated sensors ( $10^{15}$  1 MeV  $n_{eq}cm^{-2}$ ) shown in

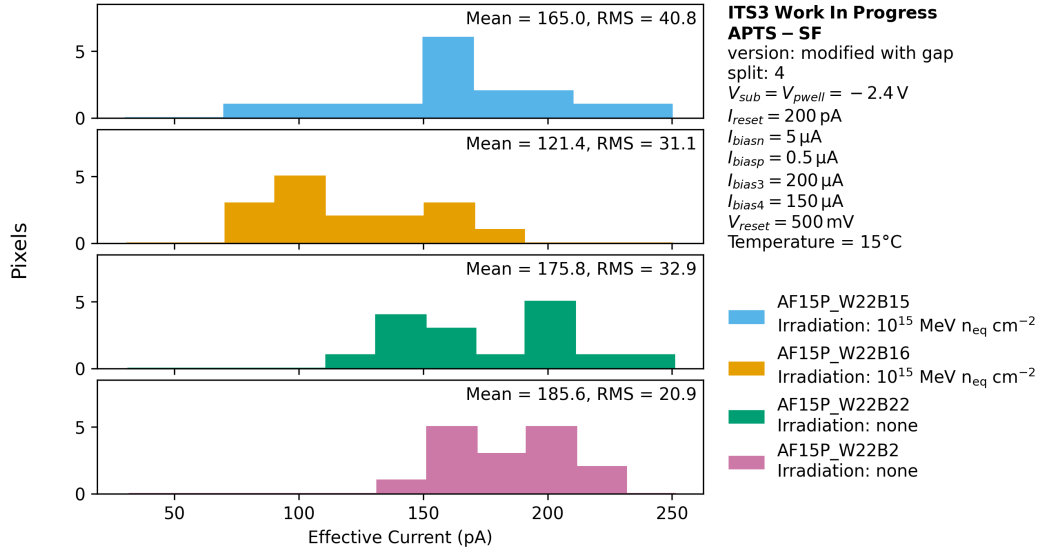


Figure 6.7: Comparison of the pixel-to-pixel variation of the effective reset current for 4 different sensors at a parameter setting of  $I_{reset,set} = 200$  pA

figure 6.7. The parameter settings chosen for this comparison are  $T = 15$  °C and  $V_{BB} = -1.2$  V, as in figure 6.6.  $\Delta I_{leakage,sys}$  (see equation 5.19) is the averaged systematic error of the leakage current and  $\Delta I_{stat}$  is the error of the mean (see equation 5.14) over all pixels. The determined leakage currents for both sensors are in good agreement with the error ranges. This confirms that the determination of the leakage current is reproducible on different sensors with the same radiation dose. Furthermore, compared to the significant spread in the effective current distribution for the two different sensors (see figure 6.7), the determined leakage current has a small variation.

Sensor	$I_{leakage}$ [pA]	$\Delta I_{leakage,sys}$ [pA]	$\Delta I_{leakage,stat}$ [pA]
AF15P_W22B15	25.91	0.30	0.28
AF15P_W22B16	26.54	0.33	0.35

Table 6.1: Average leakage current and error for two sensors with the radiation dose  $10^{15}$  1 MeV  $n_{eq}cm^{-2}$ , at  $T = 15$  °C and  $V_{BB} = -1.2$  V.

As only the leakage current at one temperature was investigated before, it is still worth looking at the pixel-to-pixel leakage current variation for different temperatures. Figure 6.8 illustrates the temperature dependence of the leakage current for all pixels of one sensor. The errors shown for each pixel are the systematic errors of the leakage current. The leakage current is increasing exponentially with increasing temperature for all pixels. The leakage current spread from pixel to pixel increases with the temperature. It is observed that for temperatures up to

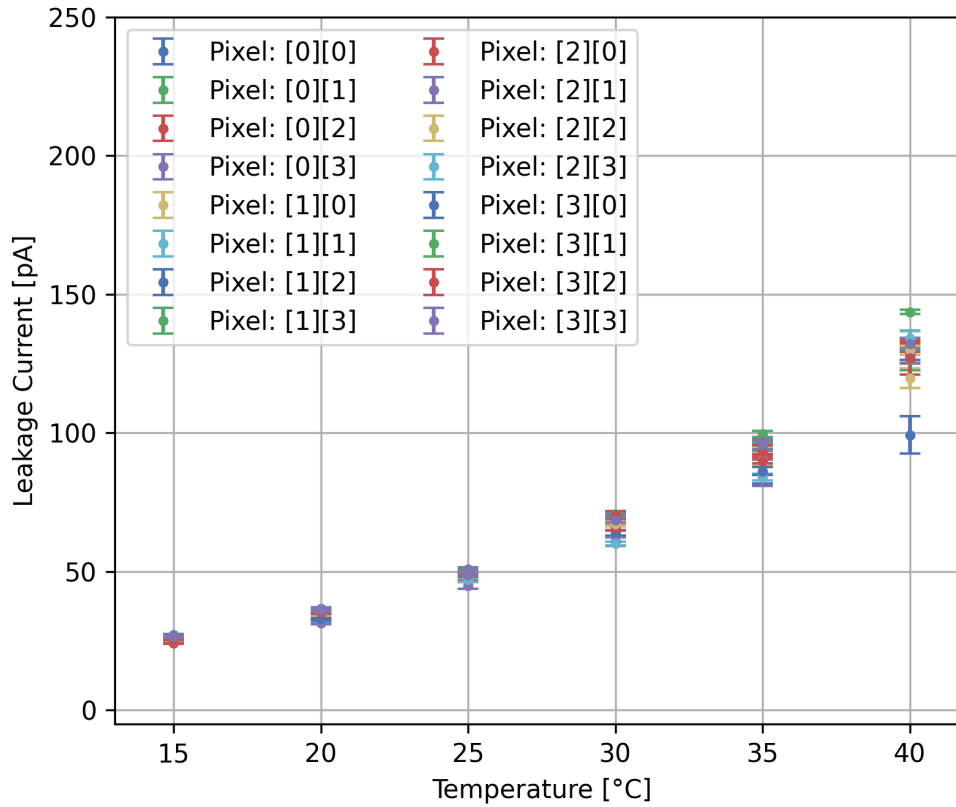


Figure 6.8: Temperature dependence of the leakage current for different pixels at  $V_{BB} = -2.4$  for an irradiated sensor ( $10^{15} \text{ 1 MeV n}_{\text{eq}}\text{cm}^{-2}$ )

35 °C, the determined leakage currents for all pixels are in good agreement with the systematic error. At  $T = 40$  °C, two pixels are deviating significantly from the average value of the remaining pixels. This can be attributed to a reduced operational range. As the leakage current increases, the number of data points available to fit for the determination of leakage current decreases (see figure 5.7 in section 5.4). This limited data can result in reduced fit quality and increase the uncertainty for the leakage current determination. Generally, the measurement of the leakage current is observed to be reliable, as it is not largely affected by the variations in the effective reset from one pixel to pixel or the temperature. However, an increase in both temperature and leakage current can lead to a wider spread in measurements across different pixels.

### 6.3.2 Leakage current dependence on reverse bias

Another parameter study covers the influence of  $V_{BB}$  on the leakage current. As discussed in chapter 4, the reverse bias has an influence on the circuitry by changing the biasing conditions of  $V_T$ , due to the body-effect, included in the complex transistor model BSIM for the subthreshold [19, 15, 18]. This leads to a higher effective reset current, as shown in section 4.4. But also in terms of leakage current. Moreover, an effect of  $V_{BB}$  on the leakage current is expected, as  $V_{BB}$  influences the charge collection in the substrate and hence also can increase the "collection of leakage current".

This is shown for the  $10^{15}$  1 MeV  $n_{eq}cm^{-2}$  irradiated sensor at various reverse bias settings in figure 6.9.

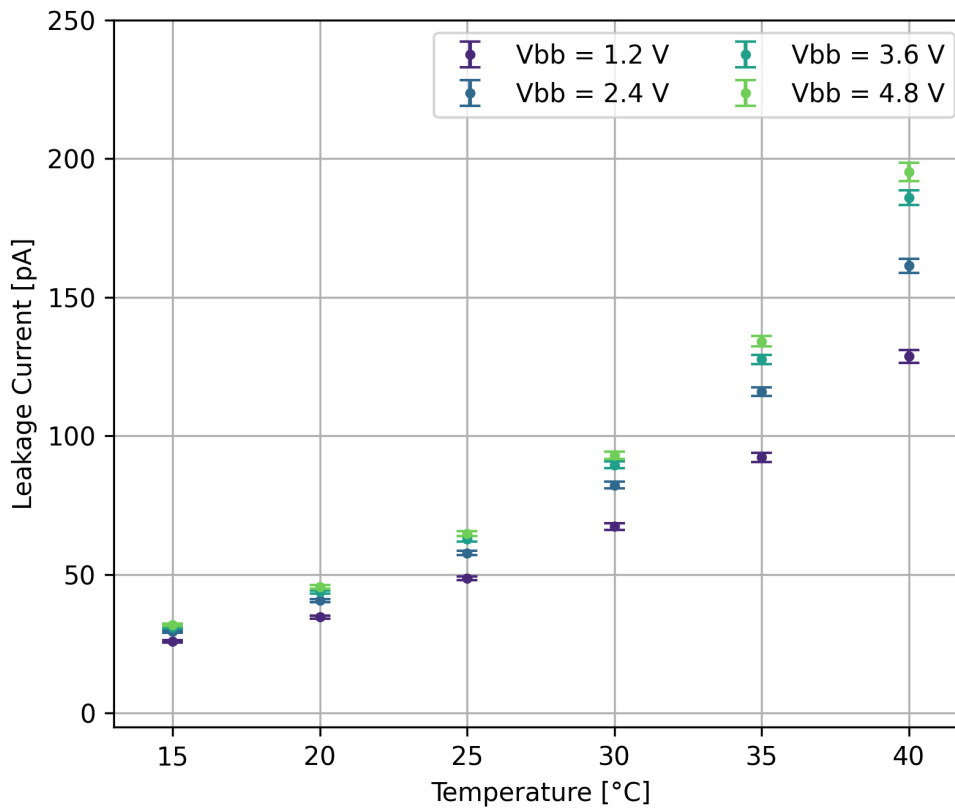


Figure 6.9: Temperature dependence of the leakage current for different  $V_{BB}$ . The leakage current represents the arithmetic mean from all pixels of the corresponding sensor ( $10^{15}$  1 MeV  $n_{eq}cm^{-2}$ ).

It shows that with increasing  $V_{BB}$  the leakage current is increasing as well. The total error of the leakage current is increasing due to the increasing systematic uncertainty in the leakage current.

A reverse bias voltage of  $V_{BB} = -4.8\text{ V}$  is chosen for the summary of the leakage currents at different irradiation levels. This high bias setting not only increases the leakage current but also the effective reset current. Figure 6.10 illustrates the  $I_{effective}-I_{reset,set}$  dependence for the leakage current determination for a reverse bias setting of  $V_{BB} = -4.8\text{ V}$  and  $V_{BB} = -2.4\text{ V}$ . It can be observed that the effective current  $I_{effective}$  is increasing with increasing reverse bias at the same temperature and  $I_{reset,set}$  setting. Additionally, a failed leakage current determination at temperatures of  $T = 20\text{ }^\circ\text{C}$  and  $T = 25\text{ }^\circ\text{C}$  is observed at bias settings of  $V_{BB} = -2.4\text{ V}$  and  $V_{BB} = -4.8\text{ V}$ , respectively. Furthermore, an increased leakage current is apparent. In the case of  $V_{BB} = -4.8\text{ V}$  the leakage fit succeeds for two temperatures, while for  $V_{BB} = -2.4\text{ V}$  this is only the case for  $T = 15\text{ }^\circ\text{C}$ . This can be attributed to the increased  $I_{effective}$  with increased reverse bias, which increased the operable range in  $I_{reset,set}$  and hence in improved fit performance.

The failed leakage current determination at  $T = 20\text{ }^\circ\text{C}$  ( $V_{BB} = -2.4\text{ V}$ ) and  $T = 25\text{ }^\circ\text{C}$  ( $V_{BB} = -4.8\text{ V}$ ) can be explained by the small operating range in  $I_{reset,set}$  in those cases. Due to the fit criteria of a minimum  $I_{effective} = 30\text{ pA}$  the leakage current determination was not performed. This criterion proves to be the correct choice in this case, as the linear relation of  $I_{effective}$  and  $I_{reset,set}$  is not given anymore under these conditions.

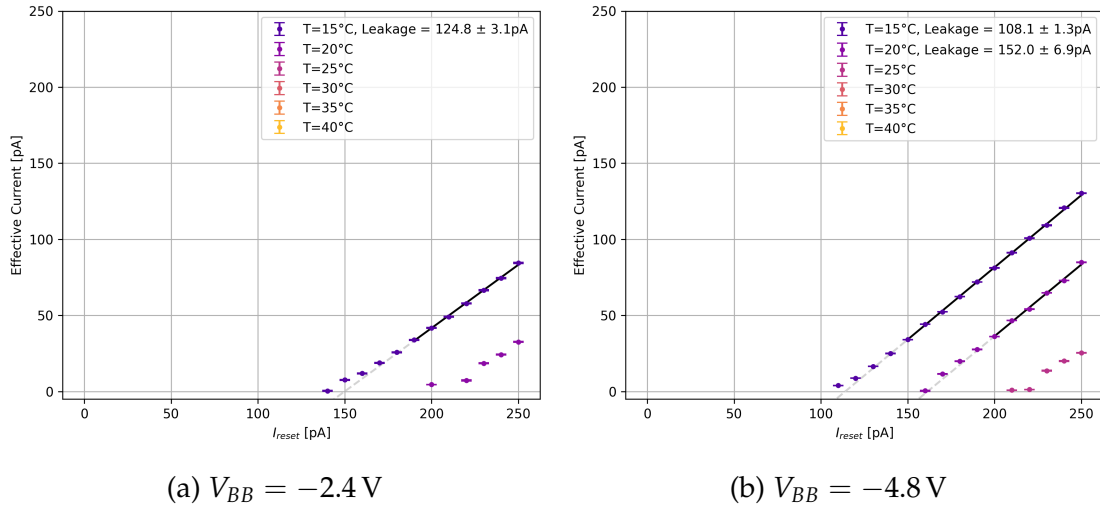


Figure 6.10: Leakage current for  $5 \cdot 10^{15}\text{ } 1\text{ MeV n}_{eq}\text{cm}^{-2}$  level at  $V_{BB} = -2.4\text{ V}$  and  $V_{BB} = -4.8\text{ V}$  back-bias voltage.

### 6.3.3 Temperature effect on the leakage current for different irradiation levels

It is left to compare the leakage current levels for different radiation doses. This analysis uses the average values derived from pixels within the device that are

### 6.3. LEAKAGE CURRENT DETERMINATION

maintained sufficiently operable to determine the leakage current. It should be noted, as highlighted in figure 6.6, that due to fabrication variations, the effective reset current ( $I_{effective}$ ) could differ significantly from pixel to pixel. As a consequence, under high temperatures and irradiation levels, certain pixels might fail to operate, or the applied fitting procedure could fail.

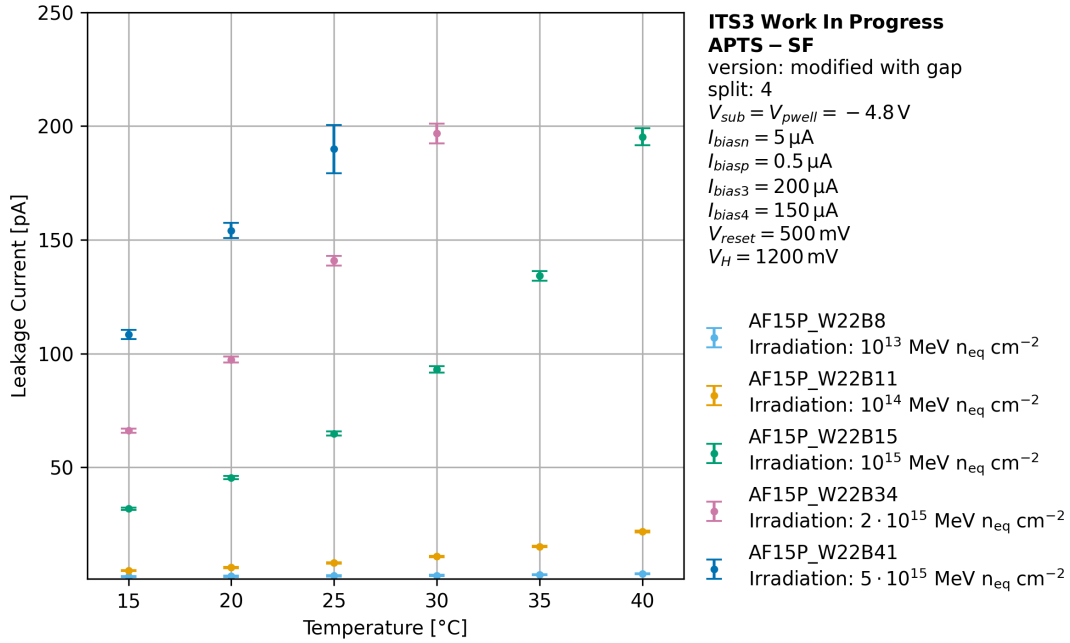


Figure 6.11: Temperature dependence of the leakage current for different irradiation levels. The leakage current represents the arithmetic mean from all well-behaving pixels of the corresponding sensor

Figure 6.11 shows the pixel-averaged leakage current against the temperature for radiation doses from  $10^{13}$   $1 \text{ MeV n}_{eq}\text{cm}^{-2}$  to  $5 \cdot 10^{15}$   $1 \text{ MeV n}_{eq}\text{cm}^{-2}$ . First of all, apart from  $10^{13}$   $1 \text{ MeV}$  (due to the small leakage current), for all irradiation levels, an exponential dependence of the leakage current to the temperature is observed, which is the expected temperature dependence (see section 2.4.1). Furthermore, the leakage current is increasing significantly with increasing radiation doses. At this parameter settings, the sensors up to a received dose of  $10^{15}$   $1 \text{ MeV n}_{eq}\text{cm}^{-2}$  are operable over the full temperature range. It is also apparent that the maximum measured leakage current for all sensors has a limit of around 200 pA. This limit can be explained by the maximum available  $I_{reset,set} = 250 \text{ pA}$ . As the leakage current exceeds 200 pA, a very small operating range in terms of  $I_{reset,set}$  is left, hence making it increasingly challenging to fulfill the fit criteria, as already discussed in the previous section 6.3.2.

It can be noted that at a radiation dose of  $10^{13}$   $1 \text{ MeV n}_{\text{eq}}\text{cm}^{-2}$ , the determination of the leakage failed for the majority of the available range of biasing and environmental parameters.

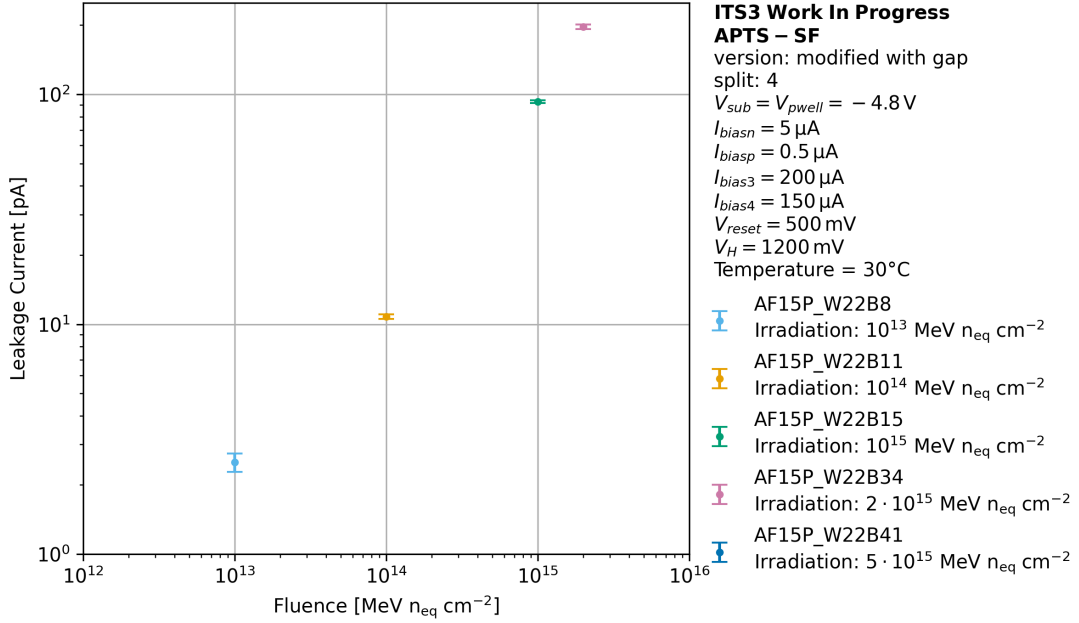


Figure 6.12: Leakage current over irradiation level for  $V_{BB} = -4.8 \text{ V}$  and  $T = 30^\circ\text{C}$

Looking at the dependence of the leakage current on the irradiation level in equation 2.18, a linear increase of the leakage current is expected with increasing radiation dose. In figure 6.12, the leakage current is plotted versus the function of the irradiation level over a double-logarithmic scale at a temperature of  $T = 30^\circ\text{C}$ . The linear relation of the leakage current to the radiation dose can be seen, especially for irradiation levels higher than  $10^{13}$   $1 \text{ MeV n}_{\text{eq}}\text{cm}^{-2}$ .

# Chapter 7

## Conclusion

This thesis aims at investigating and qualifying the 65 nm CMOS technology for the use in sensors to be implemented in future particle and nuclear physics experiments. Here, this is especially done in the framework of the ITS3 upgrade and potential ALICE3 experiment with a focus on efficiency, minimal material budget, and radiation hardness. In doing so, the Analog Pixel Test Structure (APTS) was extensively investigated. This is a prototype representative of the proposed 65nm technology, which serves as the basis for these studies. The performance dependence on radiation damage, various parameter settings, and environmental conditions are assessed for this sensor prototype. Particularly, one main objective of this thesis was to develop a method for determining the leakage current, emphasizing the temperature dependence of this current and the performance of sensors at different irradiation levels.

The analysis of the analog signal shape information from the APTS revealed that the effective reset current, which results from the externally set reset current and the counteracting leakage current, can be determined from the signal shape using a relatively simple model of the resetting behavior of the sensor (see section 5.1). This approach allows for circumventing the issues encountered with traditional I-V measurements, where other currents dominate compared to the leakage current, which is in the order of tens of pA.

In general, the determined reset current and leakage current are used to quantify the performance of irradiated and non-irradiated sensors. Furthermore, some relations of the reverse bias voltage to the sensor performance are found. The reverse bias voltage has a profound impact on the signal shape, with increasing reverse bias enhancing the amplitude due to the decreased input capacitance. It also increases the effective resetting current due to effects on the biasing conditions of the resetting transistor.

Investigating irradiated sensors, the performance of sensors exposed to radiation doses of up to  $10^{14}$   $1 \text{ MeV n}_{\text{eq}}\text{cm}^{-2}$  (NIEL) remains essentially unchanged across

the measured temperature range (15 to 40 °C). This is true when observing both the signal shape (figure 6.3) and the determined leakage current (figure 6.11), which remained in the range of 2 pA to 25 pA, even at the highest measured temperatures. In contrast to that, sensors that have been subject to a radiation dose of  $10^{15}$  1 MeV  $n_{\text{eq}}\text{cm}^{-2}$  (NIEL) irradiation dose, exhibited significant alterations in the signal shape and increased leakage current at higher temperatures but maintained a comparable signal shape to non-irradiated sensors at lower temperatures. At high temperatures, good results could be achieved under more extreme parameter settings, as high  $I_{\text{reset,set}}$  values. This biasing parameter counteracts the increasing leakage current. However, at high temperatures and low  $I_{\text{reset,set}}$  values, the sensor failed to operate stably. Even higher radiation doses lead to a further increased leakage current and significantly changed signal shape. This is observed primarily at higher temperatures and is caused by increased leakage current, which at some point compromises the capability of the sensor to reset the signal to the reference baseline voltage. Consequently, the set working point is not stable anymore and hence the sensor cannot be operated as intended. However, at extreme parameter choices for the reset current and reverse bias, as well as low temperatures, even  $10^{16}$  1 MeV  $n_{\text{eq}}\text{cm}^{-2}$  becomes operable. However, the performance is heavily compromised due to the high amount of leakage current.

From these findings, the most significant outcome is the successful development of a method to determine the leakage current from the analog sensor response. This method is established as a valuable tool for quantifying sensor performance and will surely be utilized in future studies in this field of research. Furthermore, the sensor has been neutron-irradiated to a level of  $10^{15}$  1 MeV  $n_{\text{eq}}\text{cm}^{-2}$ , the irradiated sensor remains operable over a broad range of parameters and even at high temperatures. This result is crucial for both ITS3 and the more challenging ALICE3. With the reduced distance to the interaction point in these future experiments, the sensors will encounter higher particle fluences. Given the moderate ITS3 requirement in terms of radiation hardness of  $10^{13}$  1 MeV  $n_{\text{eq}}\text{cm}^{-2}$  and an expected yearly dose of  $1.5 \cdot 10^{15}$  1 MeV  $n_{\text{eq}}\text{cm}^{-2}$  in ALICE3, the radiation hardness of the current APTS is a major leap forward compared to the studied radiation hardness of the currently installed ALPIDE sensor, which accounts to  $10^{13}$  1 MeV  $n_{\text{eq}}\text{cm}^{-2}$ . These findings especially contribute to proving the 65 nm CMOS technology to be suitable for sensors operating in future experiments and detector upgrades of existing systems.

Despite the considerable progress, this study has limitations. For instance, no detailed investigation of the altered signal shape at high irradiation levels and low biasing settings of  $I_{\text{reset,set}}$  was performed (see section 4.6). In addition, the considered sensors were only subject to neutron irradiation. It would be worth

---

studying sensors having been irradiated with charged particles to study the effects of TID irradiation damage on the sensor response, as this type of radiation is also present in the experimental use case. Future research should also explore different pixel pitches, process variants (such as the modified process), and varying doping concentrations of the low-dose n-type implant. Expanding the temperature range, possibly to negative temperatures, could yield additional insights considering the operational limits of this sensor technology with active cooling. This would require a climate chamber to overcome humidity and dew point issues. Another limitation is the precision of the simplified model used for the reset current determination (see section 5.3). For extending the studies towards more extreme operating conditions, it is worth pushing to introduce a more complex model, matching the behavior of the reset current more closely, especially in extreme conditions to account for arising non-linearities, which at the moment limit the model precision.

In conclusion, the presented results in this thesis revealed that the 65 nm CMOS technology node, here represented by the APTS, vastly exceeds the ITS3 requirements in terms of radiation hardness (NIEL) and gets very close to meeting the criteria for a possible future ALICE3 tracking detector or other planned experiments. This demonstrates that the sensors irradiated to levels of up to  $10^{15}$  1 MeV  $n_{eq}cm^{-2}$  operate effectively within a wide range of conditions and can be tuned to exhibit similar performance as a non-irradiated sensor at moderate temperatures. Moreover, it confirms, along with the newly developed method for determining leakage current, the substantial value and contribution of the research to the ITS3 R&D group and the broader field of research focusing on silicon pixel sensors for particle tracking applications in general.

# Appendices

# Appendix A

## Derivation of the fit function used for the determination of the effective reset current

To solve the separable differential equation:

$$\frac{dV_{in}(t)}{dt} = \frac{I_{effective}(1 - e^{\frac{V_{in}(t)}{V_{th}}})}{C} \quad (\text{A.1})$$

First, the equation needs to be rearranged:

$$\frac{dV_{in}(t)}{dt} = -\frac{I_{effective}(e^{\frac{V_{in}(t)}{V_{th}}} - 1)}{C}. \quad (\text{A.2})$$

Next, both sides of the differential equation are divided by  $-\left(e^{\frac{V_{in}(t)}{V_{th}}} - 1\right) / C$ :

$$-\frac{C}{e^{\frac{V_{in}(t)}{V_{th}}} - 1} \frac{dV_{in}(t)}{dt} = I_{effective}. \quad (\text{A.3})$$

Then, the differential equation is solved using the method of separation of variables and integrating both sides:

$$\int -\frac{C}{e^{\frac{V_{in}(t)}{V_{th}}} - 1} \frac{dV_{in}(t)}{dt} dt = \int I_{effective} dt. \quad (\text{A.4})$$

APPENDIX A. DERIVATION OF THE FIT FUNCTION USED FOR THE  
DETERMINATION OF THE EFFECTIVE RESET CURRENT

---

Next, the integral on the left-hand side is solved. Therefore,  $u = \frac{V_{in}}{V_{th}}$ ,  $du = \frac{1}{V_{th}} dV_{in}$ ,  $s = e^u$  and  $ds = e^u du$ :

$$\begin{aligned}
 -CV_{th} \int \frac{1}{e^u - 1} du &= -CV_{th} \int \frac{1}{(s-1)s} ds \\
 &= -CV_{th} \left( \int \frac{1}{s-1} ds - \int \frac{1}{s} ds \right) \\
 &= CV_{th} (\ln |s| - \ln |s-1|) + \text{constant} \\
 &= CV_{th} \left( \ln \left| e^{\frac{V_{in}}{V_{th}}} \right| - \ln \left| e^{\frac{V_{in}}{V_{th}}} - 1 \right| \right) + \text{constant}. \quad (\text{A.5})
 \end{aligned}$$

Combining A.4 and A.5 leads to:

$$-C \left( V_{th} \ln \left| -e^{\frac{V_{in}(t)}{V_{th}}} + 1 \right| - V_{in}(t) \right) = I_{effective} t + t_0. \quad (\text{A.6})$$

Here,  $t_0$  is the integration constant representing the time constant.

Subsequently,  $V_{in}(t)$  needs to be calculated. Therefore, equation A.6 is subjected to several mathematical transformations. Finally, the solution for  $V_{in}(t)$  is:

$$V_{in}(t) = -V_{th} \ln \left| e^{-\frac{I_{effective} t + t_0}{CV_{th}}} + 1 \right|. \quad (\text{A.7})$$

# Bibliography

- [1] M. Thomson. *Modern Particle Physics*. Cambridge University Press (cited on page 1).
- [2] *CERN homepage-The LHC*. 2012. URL: <https://home.cern/science/accelerators/large-hadron-collider> (cited on page 1).
- [3] Kenji Fukushima et al. "Quark–gluon Plasma and Heavy Ion Collisions: a Review". In: *Progress of Theoretical and Experimental Physics* 2020.8 (2020), p. 082D01. DOI: 10.1093/ptep/ptaa104. URL: <https://doi.org/10.1093/ptep/ptaa104> (cited on page 2).
- [4] B Abelev et al. "The ALICE experiment at the CERN LHC. A Large Ion Collider Experiment". In: *JINST* (2008). Also published by CERN Geneva in 2010. DOI: 10.1088/1748-0221/3/08/S08002. URL: <http://cds.cern.ch/record/1129812> (cited on page 2).
- [5] ALICE Collaboration. *ALICE upgrades during the LHC Long Shutdown 2* (2023). 2023. DOI: 10.48550/arxiv.2302.01238 (cited on pages 3, 4, 25).
- [6] F. Reidt. "Upgrade of the ALICE ITS detector". In: *Nuclear Instruments and Methods in Physics Research Section A: Accelerators, Spectrometers, Detectors and Associated Equipment* 1032 (2022), p. 166632. ISSN: 0168-9002. DOI: <https://doi.org/10.1016/j.nima.2022.166632>. URL: <https://www.sciencedirect.com/science/article/pii/S0168900222002042> (cited on page 4).
- [7] ALICE Collaboration, CERN. *Letter of Intent for an ALICE ITS Upgrade in LS3*. Technical Report CERN-LHCC-2019-018 / LHCC-I-034. CERN, Dec. 2019 (cited on pages 4, 7–9, 37).
- [8] James Philip Iddon. "Commissioning of the new ALICE Inner Tracking System". In: *JINST* arXiv:2005.01443. 08 (May 2020). DOI: 10.1088/1748-0221/15/08/C08009. URL: <https://cds.cern.ch/record/2717344> (cited on page 5).
- [9] *Tower Partners Semiconductor Co*. URL: <http://www.towersemi.com/> (visited on 05/21/2023) (cited on pages 5, 6, 8, 9, 25, 26).

- [10] M. Suljic. "Study of Monolithic Active Pixel Sensors for the Upgrade of the ALICE Inner Tracking System". In: (). URL: <http://cds.cern.ch/record/2303618> (cited on pages 5, 23).
- [11] M. Mager. "ALPIDE, the Monolithic Active Pixel Sensor for the ALICE ITS upgrade". In: (). URL: <https://doi.org/10.1016/j.nima.2015.09.057> (cited on page 5).
- [12] *APTS Datasheet version 1.7*. June 2022 (cited on pages 6, 27–31).
- [13] ALICE Collaboration. *Letter of Intent for ALICE 3 (CERN-LHCC-2022-009)*. URL: <https://arxiv.org/pdf/2211.02491.pdf> (visited on 11/01/2022) (cited on pages 9, 27).
- [14] W. R. Leo. *Techniques for Nuclear and Particle Physics Experiments*. Springer-Verlag Berlin Heidelberg GmbH (cited on pages 11, 12).
- [15] Donald A. Neamen. *Semiconductor Physics and Devices*. 3rd. New York, NY: McGraw-Hill, 2006. ISBN: 0072321075 (cited on pages 12, 15–18, 41, 70).
- [16] Wikimedia Commons. *pn-junction equilibrium graph*. [Online; accessed Nov. 21, 2020]. URL: <https://commons.wikimedia.org/wiki/File:Pn-junction-equilibrium-graph.svg> (cited on page 13).
- [17] S. M. Sze and M. K. Lee. *Semiconductor Devices: Physics and Technology*. 3rd ed. Wiley, 2007 (cited on pages 15, 18).
- [18] A. Bellaouar and M.I. Elmasry. *Low-power digital VLSI design: circuits and systems*. Kluwer Academic Publishers, 1996 (cited on pages 17, 19, 40, 41, 46, 54, 70).
- [19] M. Chan et al. "BSIM: Berkeley Short-Channel IGFET Model for MOS Transistors". In: *IEEE Journal of Solid-State Circuits* 22.4 (Aug. 1987), pp. 558–566. DOI: 10.1109/JSSC.1987.1052775 (cited on pages 17, 18, 70).
- [20] BSIM Research Group. *BSIM Models*. Department of Electrical Engineering and Computer Sciences, University of California, Berkeley. Available: <http://www-device.eecs.berkeley.edu/bsim/>. 2023 (cited on pages 17, 18).
- [21] Sherif M. Sharroush. "Analysis of the subthreshold CMOS logic inverter". In: *Ain Shams Engineering Journal* 9.4 (2018), pp. 1001–1017. ISSN: 2090-4479. DOI: <https://doi.org/10.1016/j.asej.2016.05.005>. URL: <https://www.sciencedirect.com/science/article/pii/S2090447916300685> (cited on page 18).
- [22] Harry J. M. Veendrick. *Deep-Submicron CMOS ICs - From Basics to ASICs*. 2nd ed. Springer, 2006, Chapter 7 –Subthreshold MOSFETs. DOI: 10.1007/3-540-29249-4 (cited on page 19).

- [23] *Muon stopping power and range tables, 10 MeV-100 TeV (PDG)*. 2020. URL: <https://pdg.lbl.gov/2020/AtomicNuclearProperties/adndt.pdf> (cited on page 19).
- [24] Particle Data Group et al. "Review of Particle Physics". In: *Physical Review D* 98.3 (2020), p. 030001 (cited on page 20).
- [25] Hans Bichsel. "Straggling in thin silicon detectors". In: *Reviews of Modern Physics* 60.3 (1988), p. 663 (cited on page 20).
- [26] Michael Moll. "Radiation damage in silicon particle detectors - microscopic defects and macroscopic properties". PhD thesis. University of Hamburg (cited on pages 20–22).
- [27] Hermann Kolanoski and Norbert Wermes. *Particle Detectors: Fundamentals and Applications* (cited on pages 20–22).
- [28] A Chilingarov. "Temperature dependence of the current generated in Si bulk". In: *JINST* 8 (2013), P10003 (cited on page 21).
- [29] K Aamodt et al. *Technical Design Report for the Upgrade of the ALICE Inner Tracking System*. Tech. rep. CERN-LHCC-2013-024. ALICE-TDR-017. Nov. 2013. DOI: 10.1088/0954-3899/41/8/087002. URL: <http://cds.cern.ch/record/1625842> (cited on page 23).
- [30] M. Keil and F. Reidt. *ALPIDE Software - User manual*. June 2018 (cited on page 24).
- [31] CERN – Experimental Physics Department R&D. URL: <https://ep-dep.web.cern.ch/rd-experimental-technologies> (cited on page 25).
- [32] W. Snoeys et al. "Optimization of a 65 nm CMOS imaging process for monolithic CMOS sensors for high energy physics". In: *PoS Pixel2022*. 2023, p. 083. DOI: 10.22323/1.420.0083 (cited on pages 25–28, 43).
- [33] W. Snoeys et al. "A process modification for CMOS monolithic active pixel sensors for enhanced depletion, timing performance, and radiation tolerance". In: *NIM A* 871 (2017), pp. 90–96. ISSN: 0168-9002. DOI: 10.1016/j.nima.2017.07.046. URL: <https://www.sciencedirect.com/science/article/pii/S016890021730791X> (cited on page 26).
- [34] H. Pernegger et al. "Radiation hard monolithic CMOS sensors with small electrodes for High Luminosity LHC". In: *NIM-A* 986 (2021), p. 164381. DOI: 10.1016/j.nima.2020.164381 (cited on pages 26, 27).

- [35] Gianluca Aglieri Rinella et al. “Digital Pixel Test Structures implemented in a 65 nm CMOS process”. In: (). arXiv:2212.08621v3 [physics.ins-det] 26 May 2023. DOI: 10.22323/1.420.0083. arXiv: 2212.08621v3 [physics.ins-det] (cited on pages 27, 28).
- [36] S. Bugiel et al. “Charge sensing properties of monolithic CMOS pixel sensors fabricated in a 65 nm technology”. In: *NIM A* 1040 (2022), p. 167213. DOI: 10.1016/j.nima.2022.167213 (cited on pages 27, 28).
- [37] W. Deng et al. “Design of an analog monolithic pixel sensor prototype in TPSCo 65 nm CMOS imaging technology”. In: *JINST* 18.C01065 (2023) (cited on pages 28, 30, 40, 44).
- [38] Isabella Sanna. *Characterization of first prototypes fabricated in 65 nm CMOS technology for the ALICE Inner Tracking System upgrade*. Presentation. Presented on behalf of the ITS3-WP3 at the WP1 meeting. Dec. 7, 2022 (cited on pages 34, 44).
- [39] Huber. *Minichiller 300 OLE - Huber*. accessed 2023. URL: <https://www.huber-online.com/produkte/umwaelzkuehler/umwaelzkuehler-bis-25-kw/minichiller/minichiller-300-ole#wco-productdata-technicaldata> (cited on pages 33, 46).
- [40] *HAMEG HMP manual*. accessed 2023. URL: [https://cdn.rohde-schwarz.com/hameg-archive/HAMEG\\_MAN\\_DE\\_EN\\_HMPSeries.pdf](https://cdn.rohde-schwarz.com/hameg-archive/HAMEG_MAN_DE_EN_HMPSeries.pdf) (cited on page 46).

# Acknowledgment

First, I want to express my sincerest thanks and gratitude to Silvia Masciocchi for her valuable guidance throughout my master studies and the opportunity to not only join the ALICE group in Heidelberg and at GSI but also join the ALICE ITS3 team at CERN for the research in my thesis. I consider the last year to be my greatest life experience. I am very thankful for her passionate spirit, which was really inspiring.

Furthermore, I express my gratitude to Yvonne Pachmayer for kindly agreeing to be the second referee for my thesis.

Special thanks are due to Pascal Becht and Bogdan Blidaru, for their incredible support, especially towards the end of this thesis.

Additionally, I want to thank Francesca, Isabella, Lukas, Magnus, Miko, Gabriela, Nicolas, Marius, and the whole team at CERN for the unforgettable experiences I was able to experience.

Moreover, I am grateful to Alex for supporting me with his engaged proofreading of many chapters.

I am profoundly grateful to Justyna for her incredible support and profound proofreading.

In addition, I would like to express my appreciation to everyone not mentioned by name but have played a significant role in my academic journey, contributing in various ways to my success.

В заключение, я хотел бы выразить глубокую признательность своей семье. Их неизменная любовь, поддержка и помощь были моим оплотом на этом непростом пути. Без них я бы не смог достичь того, кем являюсь сегодня.

## Declaration

I declare that this thesis has been composed solely by myself and that it has not been submitted, in whole or in part, in any previous application for a degree. Except where stated otherwise by reference or acknowledgment, the work presented is entirely my own.

Heidelberg, July 14, 2023

  
David Schledewitz